Leibniz Universität Hannover
Institut für Elektrische Energiesysteme
Fachgebiet Elektrische Energieversorgung
Prof. Dr.-Ing. habil. L. Hofmann

1. Helgoland Power and Energy Conference

24. Dresdener Kreis 2023

Foto: Carsten Graeve

Institut für Elektrische Energiesysteme
Fachgebiet Elektrische Energieversorgung
Prof. Dr.-Ing. habil. L. Hofmann

Leibniz Universität Hannover

Leibniz Universität Hannover

Fakultät für Elektrotechnik und Informatik

Fachgebiet Elektrische Energieversorgung

Dresdener Kreis

2023

Elektroenergieversorgung

24. Dresdener Kreis Elektroenergieversorgung

14. bis 15. Juni 2023

Helgoland

Herausgeber
Prof. Dr.-Ing. habil. Lutz Hofmann
Leibniz Universität Hannover
Institut für Elektrische Energiesysteme
Fachgebiet Elektrische Energieversorgung
Appelstraße 9a
30167 Hannover
Tel. +49 511 762 - 2801
Fax. +49 511 762 - 2369

DOI: http://dx.doi.org/10.15488/15895

www.iee.uni-hannover.de

Vorwort

Am 14. und 15. Juni 2023 lud das Fachgebiet Elektrische Energieversorgung am Institut für Elektrische Energiesysteme der Gottfried Wilhelm Leibniz Universität Hannover zum 24. Treffen des Dresdener Kreises ein. Neben den Fachgebietsmitgliedern aus Hannover nahmen Mitarbeitende der Universitäten aus Magdeburg, Duisburg und Dresden an der Veranstaltung teil.

Das Treffen fand in diesem Jahr auf Deutschlands einziger Hochseeinsel Helgoland statt. Somit begann das Treffen am 14. Juni für alle Teilnehmenden an den Hamburger Landungsbrücken mit der gemeinsamen Überfahrt nach Helgoland mit der Fähre. Nach der Ankunft im Konferenzsaal „Nordseehalle“ und einem gemeinsamen Mittagsimbiss folgten traditionsgemäß die Fachvorträge aus den Forschungsgebieten der teilnehmenden Institute. Der Tag endete mit einem gemeinsamen Abendessen im Restaurant „Düne Süd“, bei dem die Teilnehmenden enger zusammenrückten und sich über Fachliches sowie Privates austauschten.

Die traditionelle Exkursion am zweiten Tag der Veranstaltung setzte sich in diesem Jahr aus zwei Teilen zusammen. Zunächst besichtigten alle Teilnehmenden die Leitwarte der RWE Renewables Trident Offshore GmbH, wo sie einen Einblick in das operative Geschäft der Offshore Windparks vor Helgolands Küste bekamen. Der zweite Teil der Exkursion stellte die Ausfahrt in den Offshore-Windpark Kaskasi dar. Mit der gemeinsamen Rückreise von Helgoland nach Hamburg wurde das 24. Treffen des Dresdener Kreises beendet.

Gruppenfoto der Teilnehmenden vor der Nordseehalle

Danksagung

Für zwei sehr interessante wie auch faszinierende Tage auf Helgoland, an denen wir, der Dresdener Kreis, die Möglichkeit hatten, die 1. Helgoland Power and Energy Conference durchzuführen und mit über 40 Personen an einer Exkursion zum Offshore-Windpark Kaskasi teilzunehmen, möchte ich auch im Namen meiner Kollegen Prof. Schegner, Technische Universität Dresden, Prof. Wolter, Otto-von-Guericke-Universität Magdeburg, und Prof. Vennegeerts, Universität Duisburg-Essen, der RWE Renewables GmbH unseren herzlichen Dank aussprechen.

Die beteiligten Mitarbeiterinnen und Mitarbeiter der RWE Renewables haben sich sehr viel Mühe gegeben, die Aufgaben der RWE Renewables zu erläutern und unsere Fragen ausführlich, detailliert und verständlich zu beantworten. Uns wurde eindrucksvoll vor Augen geführt, wie groß und vielfältig die Herausforderungen sind, die RWE Renewables als Beitrag zur Energiewende zu bewältigen hat. Dies wurde auch durch die Exkursion zum Windpark Kaskasi eindrucksvoll demonstriert. Alle Teilnehmer waren begeistert und haben diese einmalige Gelegenheit, den Offshore-Windpark hautnah zu erleben, sehr genossen und hoch geschätzt.

Wir möchten uns bei allen Mitarbeiterinnen und Mitarbeitern der RWE Renewables ganz herzlich für die hervorragende Organisation unseres gesamten Aufenthaltes auf Helgoland, die großzügige Gastfreundschaft an beiden Tagen, die freundliche Aufnahme und das Interesse an unseren wissenschaftlichen Vorträgen und deren Diskussion bedanken.

Lutz Hofmann
Fachgebiet Elektrische Energieversorgung
Institut für Elektrische Energiesysteme
Leibniz Universität Hannover

Inhaltsverzeichnis

1. Helgoland Power and Energy Conference (HPEC 2023)

Agenda 14. & 15. Juni 2023

Mittwoch, 14. Juni 2023

Zeit	
08:45 Uhr	**Anreise Helgoland** *Fähre Hamburg–Helgoland* *St. Pauli Landungsbrücken 3/4* *Abfahrt 09:00 Uhr*
12:45 Uhr	**Ankunft auf Helgoland** *Binnenhafen/Südhafen (je nach Wetterlage)* *Ca. 1,2 km Fußweg vom Binnenhafen zur Nordseehalle (Konferenzsaal)* *Kurpromenade 8*
13:30 Uhr	**Mittagsimbiss**
14:00 Uhr	**Begrüßung der Teilnehmer** *Prof. Dr.-Ing. habil. Lutz Hofmann, Uni Hannover* *Dr.-Ing. Jörn Runge, RWE Offshore Wind GmbH*
14:30 Uhr	**Fachvorträge Block 1** *Leitung: Prof. Dr.-Ing. Hendrik Vennegeerts, Uni Duisburg-Essen*
	„Approaches and methods for automation of low-voltage distribution networks“ *Dipl.-Ing. Laura Fiedler, Uni Dresden*
	„Comprehensive Study of the Full Grid Forming Direct Voltage Converter Control“ *M. Sc. Marc Wöstefeld, Uni Duisburg-Essen*
	„Methodology for Projection of the Diffusion of Electric Vehicles in Residential Consumers“ *M. Sc. Mauro dos Santos Ortiz, Uni Magdeburg*
	„TSO-DSO Cooperation Under Multiple Vertical Interconnections“ *M. Sc. Lars Stark, Uni Hannover*
16:30 Uhr	**Kaffeepause/Fototermin**
17:00 Uhr	**Fachvorträge Block 2** *Leitung: Prof. Dr.-Ing. habil. Martin Wolter, Uni Magdeburg*
	„Harmonic stability assessment of commercially available single-phase photovoltaic inverters in public low voltage networks“ *Dipl.-Ing. Elias Kaufhold, Uni Dresden*
	„InRush-Currents of Series Combination of Transformer with in-phase Regulation and PST“ *Dr.-Ing. Fekadu Shewarega, Uni Duisburg-Essen*
	„Dynamic Security Enhancement in Power Networks with High Share of Wind and Solar-PV Power Generations“ *Dr.-Ing. Tahaguas Woldu, Uni Magdeburg*
	„Simulation Studies of an Model Predictive Control-Based Operation of Island Power Systems“ *M. Sc. Lucas Reus, Uni Hannover*
19:00 Uhr	**Ende der Vortragsreihen**

19:15 Uhr **Check-In Hotel**
Helgoländer Botschaft
Lung Wai 39

20:00 Uhr **Abendveranstaltung**
Restaurant Düne Süd
Lung Wai 41

Donnerstag, 15. Juni 2023

Zeit

09:15 Uhr **Besichtigung Leitwarte**
RWE Renewables Trident Offshore GmbH
Rickmer-Bock-Wai 1215

11:00 Uhr **Zeit zur freien Verfügung**
Gemeinsamer Mittagsimbiss in Planung ggf. Selbstversorgung
Erkundung der Insel etc.

13:15 Uhr **Ausfahrt Offshore-Windpark Kaskasi**
Helgoland Südhafen
Abfahrt 13:30 Uhr
Rückkehr nach Helgoland ca. 15:30 Uhr

16:45 Uhr **Abreise von Helgoland**
Fähre Helgoland-Hamburg
Helgoland Binnenhafen/Südhafen (je nach Wetterlage)
Abfahrt 17:00 Uhr

20:30 Uhr **Ankunft St. Pauli Landungsbrücken und individuelle Abreise aus Hamburg**


Nordseehalle
Helgoländer Botschaft
Restaurant Düne Süd
Binnenhafen
Leitwarte
Südhafen
Wichtige Orte:
An-/Abreise:
Helgoland Binnenhafen/ Südhafen (je nach Wetterlage)
Konferenzsaal/Vorträge:
Nordseehalle
Kurpromenade 8
Check-In Hotel:
Helgoländer Botschaft
Lung Wai 39
Abendveranstaltung:
Restaurant Düne Süd
Lung Wai 41
Leitwarte:
RWE Renewables Trident Offshore GmbH
Rickmer-Bock-Wai 1215

Categorization of approaches and methods for automation of low-voltage distribution networks

Laura Fiedler and Peter Schegner
Institute of Electrical Power Systems and High Voltage Engineering
TUD Dresden University of Technology
Dresden, Germany
laura.fiedler@tu-dresden.de, peter.schegner@tu-dresden.de

***Abstract*—The defossilization of the power system has a particular impact on low-voltage distribution networks. During this process, a large number of photovoltaic systems, charging infrastructure for electric vehicles and heat pumps are installed in these networks. In order to ensure the continuous integration of power-intensive producers as well as consumers, and to guarantee reliable network operation, the digitisation and automation of low-voltage networks is essential. Therefore, Grid Energy Management is the appropriate tool. Hence, this paper provides a systematization of the functions to be automated in the Grid Energy Management. Additionally, this paper analyses possible problem formulations and calculation approaches with special regard to the automation of congestion management and grid operation optimization. In conclusion, this paper represents an entry point for further investigations in the area of active distribution networks and the computation methods required.**

Keywords—active distribution network, smart grid, congestion management, optimal power flow, optimization techniques

I. Introduction

The continuous integration of power-intensive producers like photovoltaic systems and consumers such as heat pumps and electric vehicles drastically changes the load situation of low-voltage distribution grids. This results in a massive need for grid expansion. Due to the significant financial investment required and the substantial personnel and administrative effort needed, the necessary expansion measures are not achievable within a short timeframe. The solution lies in automating the operation and the planning of low-voltage distribution networks.

Two network features are essential for this automation: observability and controllability. The former requires continuous metering at secondary substations and in particular at smart meters. These measurement data are used within a State Estimation algorithm to determine the network state. Besides measured data also forecast data or schedules can contribute to the network observability. By additionally installing actuators within the network, e.g. on-load tap changing transformers (OLTC) or load control units, its controllability can be archived. An observable and controllable network offers many opportunities for the network operator. Accurate data prevents unnecessary over-dimensioning through more precise expansion planning. The possibility to control the network power flow through actuators results in a more predictable and temporal deferrable expansion need. Furthermore, the executed expansion is more economically efficient due to avoidance of bottlenecks in material, personnel and civil engineering.

The tool for implementing the automation of network operation as well as planning and for the coordination of various automated functionalities is Grid Energy Management. Fig. 1 shows the classification of Grid Energy Management in the context of the different automation systems, which also aim to influence energy consumption and feed-in in low-voltage distribution systems. Three main Energy Management (EM) categories have been identified: Domestic EM, Commercial EM and Grid EM. As there are no consistent definitions for any of these three categories in the literature, this paper will first explain each one and the differences between them. *Domestic EM* can be additionally divided in Home EM, Building EM and Community EM. Domestic EM executes actions with regard to the interests of the inhabitants, who live in the managed house, building or community. In contrast to this, *Commercial EM* focusses more on the economic optimization of processes and the use of energy. ***Grid EM* comprises all measures taken or incentivised by the grid operator to improve and maintain the network's efficiency or reliability**.

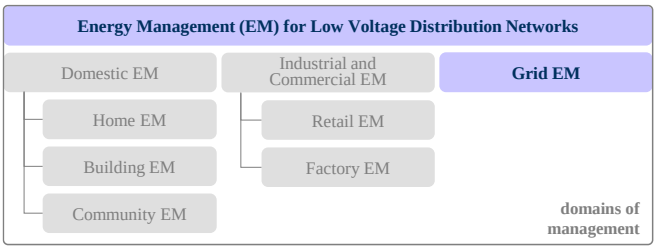

Fig.1. Domains of energy management in low-voltage distribution systems, based on [1]

These categorised types of EM differ, inter alia, in real-time requirements, possible control actions and management objectives. However, as it is evident from the descriptions, the primary distinction between the three is which stakeholders' interests are represented by the management. The challenge with automation tasks performed by the Grid EM is that its sphere of influence is much larger compared to Home, Building or Factory EM. In addition, its architecture and data handling must be scalable to multiple networks or perhaps even multiple voltage levels.

Due to these significant challenges posed by Grid EM, this paper will start in Chapter II with explaining the concept of Grid EM in more detail and providing a systematic overview of the functions of Grid EM. Based on this, Chapter III then addresses specific functions of automated Grid Operation with their corresponding problem formulations as well as calculation approaches.

II. Grid Energy Management as Tool for Grid Automation

To provide an extensive explanation of Grid EM and demonstrate how it operates as an automation tool, the automated functions and its distinguishing features are analysed. Grid EM can be characterised by different **properties**. One attribute is the *sphere of influence*. Thereby, a distinction is made in particular with regard to the variety of control options, e.g. the number and size of controllable grids/ grid voltage levels,

This work was supported by the German Federal Ministry for Economics and Climate Action with the grant number 03EI6075A.

as well as the possible controllable consumers, generators and assets. Another distinctive feature is the *external influences* taken into account in the management. Since the Grid EM does not exclusively determine the energy flows in low-voltage distribution networks, it is important to consider other stakeholders. This primarily involves aggregators, energy retailers, prosumers and other grid operators, so that, for example, the influences of sector coupling or demand response can be included in the Grid EM. The present *system architecture* for the interaction with other Grid EMs is also a classifying attribute. This can be, for instance, centralised, decentralised or hierarchical. Another characteristic is the *point in time* affected by the control action and the points in time at which the calculation of the same is carried out. The control measures implemented may have short-, medium- or long-term objectives and effects. They can be based on forecasts and thus be preventive, or curative due to their measurement-based calculation. Finally, the *functions automated* by Grid EM are a very important feature.

Fig. 2 displays the three groups of **automated functions** identified, including important example functions that have been widely discussed in the literature. Thereby *Grid Monitoring* refers to activities that aim to measure important parameters related to network resources [2]. In addition, the Grid Monitoring functions provide the data basis for the other two groups, Grid Operation and Grid Planning. For example, fault detection, which includes determining the type and location of the fault, is necessary to calculate self-healing control actions [3]. Furthermore, the data generated by the grid state calculation is required for congestion management, grid operation optimization and network expansion planning. The functions summarised under the term *Grid Operation* refer to activities to maintain and optimise the stability, economic efficiency, reliability and quality of network operation on an operational time scale. This excludes any constructional changes to network resources. In contrast to that, *Grid Planning* is the umbrella term, as stated by the IEV, for all activities involved "in the development of a technically and economically sound system of electricity supply" [4]. The potential changes taken into account in this planning process include, in particular, constructional changes to the network assets as well as changes to the connected facilities. For these activities, a medium- to long-term time horizon is considered. Some additional function not addressed in Fig. 2 can be found in [5].

Depending on the control actions automated by functions of the Grid EM, the degree of system automation can be determined. This is a metric for the extent to which network planning and operation are automated, i.e. carried out without human intervention. The underlying basis for automating tasks is an observable and controllable network. For these basic functionalities, a Grid EM would only provide Grid Monitoring functions with the corresponding data processing and human remote control [6]. With a higher degree of automation the human decision making processes are supported by steady calculations. Therefore, functions of the groups Grid Monitoring and Grid Planning are implemented within the Grid EM but they are not able to execute decisions without human reviewing. When further automating the entire system, even the execution of decisions is handled automatically. The full system is automated, when no human intervention besides setting the requirements for the processes is needed. It is debatable whether complete automation of the system is desirable, as the cost of automation and management must balance its benefits.

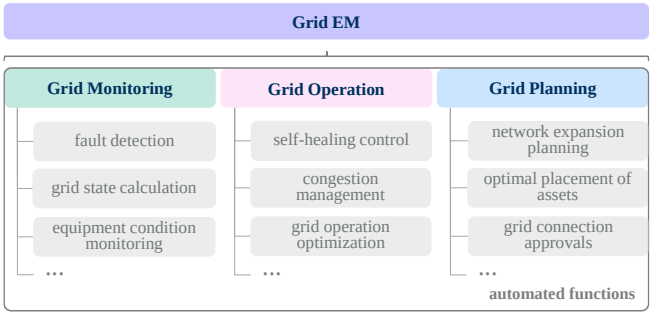

Fig. 2. Categorisation of the functions automated by a Grid EM

Due to recent changes in the German regulatory framework, such as the revision of §14a EnWG, there is now a heightened interest in the automation of congestion management and grid operation optimization. Thus, these are the subject of the following chapter.

III. Grid Operation Automation

A. Characterization of the Grid Operation Functions

First, the functions belonging to Grid Operations need to be properly defined. In addition to the properties of a Grid EM already described, further characteristic features can be used to distinguish the automated functions. Fig. 3 presents an overview on these features. All functions aim to improve the **grid operation mode** on an operational time scale. However, each of the three functions serves a distinct grid operation mode. This allows a clear division of functions. Self-healing control remedies the faulty operation. In this case, electricity supply is no longer available in certain areas of the network. Whereas congestion management is used to resolve the vulnerable grid operation, where no energy supply failure but violations to the same occur. Furthermore, grid operation optimization aims to improve the normal operation additionally. However, this distinction is not established in the literature.

The **control system design** is another characteristic feature of the functions. The available *control measures* can be used to characterise the control system design. These measures may be direct, where the system operator directly controls an asset of its own property or a contracted controllable distributed energy resource (DER), load or storage. They might also be indirect, where the system operator incentivises network users to support the operator in achieving a particular objective. Market-based measures belong to this category of indirect measures. Both types of measures may also be used in combi-

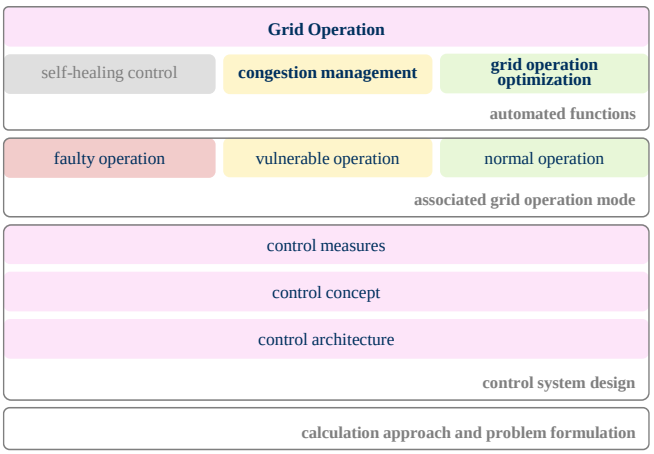

Fig. 3. Characterization of Grid Operation functions

nation. The measures used in the two functions with the greatest research demand, congestion management and grid operation optimization, are briefly discussed in the following. Common direct measures used for congestion management in low-voltage distribution networks are e.g. network reconfiguration, on-load tap changer control, photovoltaic or load curtailment, reactive power control or phase-shifting transformers. On the other hand, indirect measures derive from congestion management which is organised through flexibility markets [7], dynamic tariffs or network charges [8]. It is also possible to adapt the redispatch concept to the low-voltage distribution network [9]. Grid operation optimization primarily utilises the grid operator's own assets for direct measures. On the other hand, measures that control or influence the equipment of network users are subject to strong cost-benefit considerations.

In addition, the underlying *control concept* is an essential element of the control system design for automated Grid Operation functions. The control concept describes the relationship between calculating and executing the control signal. Accordingly, the execution of direct control signals can be of various types. Thereby, signals can be executed directly after the calculation, which implies an ad hoc control. It is also possible to calculate the control signals with a time offset then communicate a schedule to the executing asset and, if necessary, adapt it again before execution. This is called schedule-based control. The signal may alternatively be executed according to a predetermined characteristic or set of rules. For indirect control measures, the relationship between calculation and execution of the control signal is much more complex, since the signals are usually generated by other EM systems. The grid operator only incentivises actions. The implementation of indirect control is very individual and diverse in the literature, depending on the framework assumed. The control concept for indirect measures can therefore be categorised primarily based on the EM finally executing the control command.

The *control architecture* is also important in describing the control system design. Hereby, it is distinguished between network-wide control mechanisms and local controllers. These may be combined. In this case, the chosen hierarchy between the entities as well as the decision making process in case of control signal conflicts is of particular importance.

The **calculation approach** is also an important feature of an automated function. It represents the programmatically implementation for solving the underlying problem of the task, which is to be automated. The problem varies depending on the control measures available, the control concept and the control architecture chosen. Ultimately, the calculation approach must be chosen according to the problem. Chapter III.B will deal with this more detailed.

B. Calculation Approaches and Formulation as Optimal Power Flow (OPF) Problem

In order to discuss the different solutions methods that can be utilised to automate congestion management and grid operation optimisation, their three main categories of calculation approaches are first explained. Fig. 4 illustrates the subdivision into rule-based, optimisation-based and hybrid methods. *Rule-based calculation* approaches offer high simplicity and real-time feasibility, but suffer from a lack of optimality in their decision making [10, 11]. Another disadvantage is the limited scalability and high calibration effort [12] required to adapt to different networks and scenarios, which can be a significant practical challenge for broad implementation. Whereas, in recent years, *optimisation-based computation* methods have been mainly used by researchers [11], which demonstrates their effectiveness in tackling complex grid optimisation problems. However, optimisation-based solution methods generally require a higher computational effort [13] due to the intricacy of the underlying problems and the extensive search for optimal solutions. *Hybrid* approaches combine both strategies.

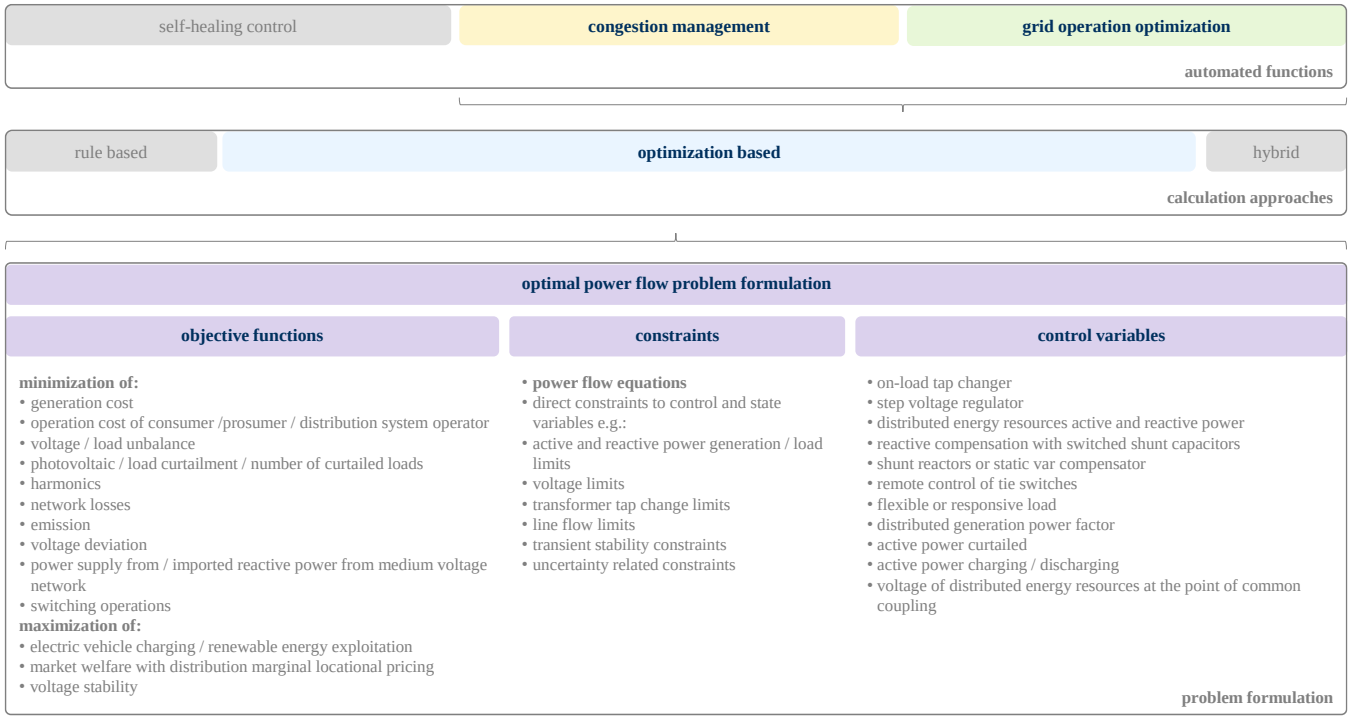

Fig. 4 Overview of different optimal power flow formulations itemised according to the objective functions, the constrains and the control variables, compilation based [10, 14–19]

1) OPF Problem Formulation

Due to the advantages of the optimisation-based calculation methods, the following explanations will deal with these methods in particular. In addition, optimisation-based approaches are able to solve **Optimal Power Flow (OPF) problems**. Hereby, OPF problems are very common in the electrical power system and are a mainstay of grid operation and management. Thus, the tasks of congestion management and grid operation optimisation can also be formulated as OPF problems. The classical OPF formulation was described by Carpentier in 1962 and is aimed to minimise the total cost of power generation while ensuring the safe and reliable operation of the power system [20]. Beyond that, OPF problems cover a wide range of applications today [21], such as operation and market-related subjects [22] or network expansion calculations. Furthermore, the utilization of OPF is extended to distribution networks, where challenges like the controlling a large number of DER and the uncertainty of load and DER profiles must be addressed [23].

Before discussing optimisation-based approaches in detail, the problem to be solved and its structure are examined. An OPF problem formulation consists of an **objective function**, **equality and inequality constraints**, which contain the power flow equations, as well as the **control variable(s)**. Fig. 4 provides a summary of possible formulations. The objective function naturally determines the target to be achieved, while the constraints serve to maintain the operating limits of the grid, the assets and the network user's equipment. Uncertainty-related constraints can also be included. The control variables logically depend directly on the available control measures. Based on the problem formulation a large number of subcategories within the OPF problem has been defined in literature [10].

2) Optimization-based calculation approaches

In the following, an overview of the optimization-based approaches that are used in the literature for the solution of OPF problems is provided. It should be noted that there is no consistent classification of these solution methods, e.g. metaheuristics can be categorized as computational intelligence methods in a wider meaning [24]. Therefore, a combination of different resources is presented here. Fig. 5 illustrates the compilation of methods described in this section.

The optimisation-based methods include deterministic, non-deterministic and hybrid approaches. **Deterministic methods** are sometimes referred to as classical methods [25] or methods based on mathematical programming [26]. The subcategories, such as linear and non-linear programming, are umbrella terms for various algorithms. For example, the interior point and the simplex algorithms are linear programming methods [27]. In [19] a comprehensive review of deterministic methods is presented, including a comparison of the advantages and disadvantages of the various algorithms. In general, deterministic methods are well researched and have been applied widely. Still, the deterministic methods inherently suffer from multiple drawbacks, including their high sensitivity to the starting point [23], issues with highly constrained problems [28] and integer or binary variables [19]. Although these methods have been applied at high computational expense for day-ahead applications for large systems and near-real-time applications for medium-sized systems [28]. Nevertheless, there is the risk of converging to local optima [19, 29]. To overcome this problem, many researchers utilise relaxation and convexification approaches in combination with the deterministic methods. In [30] a review of convexification methods used for the non-linear non-convex AC OPF problem is provided. The review focuses on the exactness of the simplifications made, as

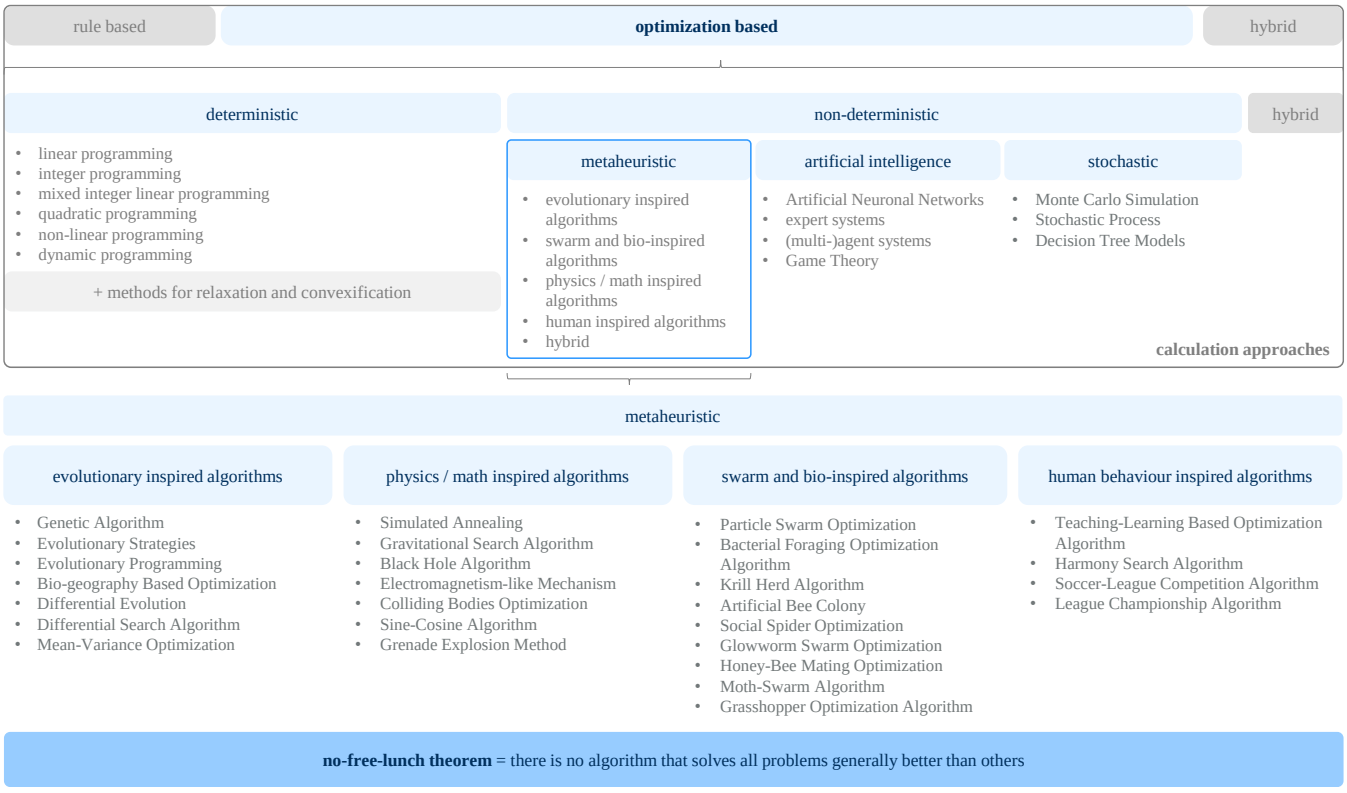

Fig. 5. Overview of calculation approaches with special regard to optimization-based methods, compilation of optimization-based methods from [18, 24, 31–35]; categorization of metaheuristic algorithms based on [36]

this is a metric for applicability. Moreover, [37] discussed in a systematic survey the problem formulations and relaxations utilised for AC OPF.

The **non-deterministic methods** can be distinguished in metaheuristic, artificial intelligence and stochastic methods. *Metaheuristic algorithms* are characterised by their problem-independent solution strategy [38]. They are analysed more closely in the following, due to the particularly high level of attention they received in the literature. Fig. 5 categorises the metaheuristic approaches by the emulated natural pattern [36]. Other resources distinguish the metaheuristic approaches in trajectory-based and population-based [39]. However, as the number of algorithms listed in Fig. 5 emphasises, there is no algorithm that solves all problems generally better than others. This has been stated in the no free lunch theorem [40]. According to that, each of the algorithms has individual strengths and weaknesses. In general, metaheuristics tend to find sub-optimal but high-quality solutions in a reasonable amount of time [38]. However, the ability to avoid local minima and the rate of convergence varies significantly between algorithms [41]. A fundamental challenge with metaheuristics is to define a suitable termination criterion [42]. Additionally, there is a lack in well-established benchmarks for statistically valid and reliable comparisons, especially for optimization dealing with power system issues [43]. A large number of overview studies deals with metaheuristic approaches such as [44], which focusses on the evolutionary inspired computation methods. In [45] the background of metaheuristic optimization is discussed in detail. Additionally, [46] reviews the applications of metaheuristics for OPF calculation. A critical review on the application of metaheuristics in power system optimization is provided in [43]. Non-deterministic approaches also include methods based on *artificial intelligence* such as Artificial Neural Networks [34], expert systems [24], (multi-)agent systems [24, 33] and Game Theory [33, 35]. This subcategory summarizes specialised tools and intelligent methods for solving various types of problems [24]. *Stochastic methods*, such as the Monte Carlo Simulation, which is often used as a reference solution but involves a long computation times, are also included within the subcategory of the non-deterministic methods [29].

Hybrid approaches combine either multiple deterministic methods, multiple non-deterministic methods or both types [47]. As a result, the disadvantages of one algorithm may be compensated through the advantages of another. For example, it is possible to combine a metaheuristic algorithm, which performs a global search and the exploration of the feasible region, with a deterministic approach that executes a local search [43]. The differential evolutionary particle swarm optimization presented in [48], which combines differential evolution, evolutionary programming and particle swarm optimization, can also be cited as an example.

Additionally, calculation approaches can be distinguished according to the utilized **uncertainty handling method**. Although this negligence of uncertainties may be sufficiently accurate for some issues, review papers repeatedly emphasize the importance for their consideration in calculations concerning low-voltage distribution networks. Fig. 6 gives an overview of these uncertainty handling approaches. The appropriate method for modelling uncertainty in a problem depends primarily on the information available about the uncertainty and the requirements regarding accuracy and computation time.

Numerous reviews [49–55] offer detailed insights into the modelling of uncertainties.

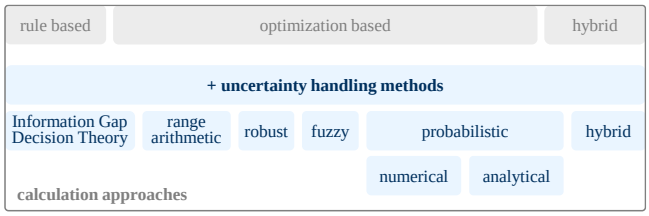

Fig. 6. Overview of uncertainty handling methods according to [26, 55]

IV. Conculsion

The paper presents a clear introduction to the topic of automating low-voltage distribution networks, outlining the crucial role of grid energy management as a fundamental tool for achieving the automation of the monitoring, operation and planning of these networks.

The functions to be automated within low-voltage distribution networks are identified. This paper focuses particularly on the automation of grid operation for congestion management and grid operation optimization. The large variety of problem formulations related to these two control functions, including the objective functions, control variables as well as constraints are examined. It is outlined that both of these control tasks can be expressed as optimal power flow problems.

Additionally the paper gives a classification of calculation methods for the automated functions. The optimisation-based calculation approaches are discussed in more detail. In particular, this paper analyses the advantages and disadvantages of deterministic and metaheuristic methods. Overall, no generally applicable solution method can be identified and the optimal and most effective calculation approach depends on the defined problem.

References

[1] S. S. Ali and B. J. Choi, "State-of-the-Art Artificial Intelligence Techniques for Distributed Smart Grids: A Review," *Electronics*, vol. 9, no. 6, p. 1030, 2020, doi: 10.3390/electronics9061030.

[2] S. Andreozzi, E. Fattibene, G. Misurelli, G. L. Rubini, C. Aiftimiei S. Fantinel, G.Cuscela, G. Donvito, N. De Bortoli, G. Tortone, "GridICE: Requirements, Architecture and Experience of a Monitoring Tool for Grid Systems," *CHEP Mumbai (India)*, 2006.

[3] S. A. Arefifar, M. S. Alam, and A. Hamadi, "A Review on Self-healing in Modern Power Distribution Systems," *Journal of Modern Power Systems and Clean Energy*, 2023, doi: 10.35833/MPCE.2022.000032.

[4] *International Electrotechnical Comission - power system planning*, IEV ref 603-01-01.

[5] Vladimír Mařík, Jose L. Martinez Lastra, and Petr Skobelev (eds.), "Review of Trends and Challenges in Smart Grids: An Automation Point of View," *6th International Conference, HoloMAS 2013, Prague, Czech Republic, August 26-28, 2013, Proceedings*, vol. 8062, 2013.

[6] M. Braun *et al.*, *Systematisierung der Autonomiestufen in der Netzbetriebsführung*: VDE Impuls, VDE Verband der Elektrotechnik Elektronik Informationstechnik e.V., 2020.

[7] Ioannis Bouloumpasis, David Steen, and Le Anh Tuan, "Congestion Management using Local Flexibility Markets: Recent Development and Challenges," 2019.

[8] A. Tomar, "Congestion management techniques in PV Rich LV distribution grids - a structured review," *Energy Syst*, vol. 113, no. 2, p. 411, 2023, doi: 10.1007/s12667-023-00571-6.

[9] Carsten Krüger, Marcel Otte, Stefanie Holly, Saskia Rathjen, Arlena Wellßow, Sebastian Lehnhoff, "Redispatch 3.0 – Congestion Management for German Power Grids – Considering Controllable Resources in Low-Voltage Grids," *ETG Kongress 2023*, 2023.

[10] H. Abdi, S. D. Beigvand, and M. La Scala, "A review of optimal power flow studies applied to smart grids and microgrids," *Renewable and Sustainable Energy Reviews*, vol. 71, pp. 742–766, 2017, doi: 10.1016/j.rser.2016.12.102.

[11] M. Hosseinzadeh and F. R. Salmasi, "Robust Optimal Power Management System for a Hybrid AC/DC Micro-Grid," *IEEE Trans. Sustain. Energy*, vol. 6, no. 3, pp. 675–687, 2015, doi: 10.1109/TSTE.2015.2405935.

[12] Y. Zhang, B. Vand, and S. Baldi, “A Review of Mathematical Models of Building Physics and Energy Technologies for Environmentally Friendly Integrated Energy Management Systems,” *Buildings*, vol. 12, no. 2, p. 238, 2022, doi: 10.3390/buildings12020238.

[13] A. R. Sahu, B. Bose, S. Kumar, and V. K. Tayal, “A Review of Various Power Management Schemesin HEV,” *2020 8th International Conference on Reliability, Infocom Technologies and Optimization (Trends and Future Directions) (ICRITO)*, pp. 1296–1300, 2020, doi: 10.1109/ICRITO48877.2020.9197881.

[14] J. Kallrath, Ed., *Optimization in the energy industry: Optimization Methods Application to Optimal Power Flow in Electric Power Systems*. Berlin: Springer, 2009.

[15] E. Naderi, H. Narimani, M. Pourakbari-Kasmaei, F. V. Cerna, M. Marzband, and M. Lehtonen, “State-of-the-Art of Optimal Active and Reactive Power Flow: A Comprehensive Review from Various Standpoints,” *Processes*, vol. 9, no. 8, p. 1319, 2021, doi: 10.3390/pr9081319.

[16] I. A. Ibrahim and M. J. Hossain, “Low Voltage Distribution Networks Modeling and Unbalanced (Optimal) Power Flow: A Comprehensive Review,” *IEEE Access*, vol. 9, pp. 143026–143084, 2021, doi: 10.1109/ACCESS.2021.3120803.

[17] S. Claeys, M. Vanin, F. Geth, and G. Deconinck, “Applications of optimization models for electricity distribution networks,” *WIREs Energy Environ.*, vol. 10, no. 5, p. 1, 2021, doi: 10.1002/wene.401.

[18] V. A. Evangelopoulos, P. S. Georgilakis, and N. D. Hatziargyriou, “Optimal operation of smart distribution networks: A review of models, methods and future research,” *Electric Power Systems Research*, vol. 140, no. 3, pp. 95–106, 2016, doi: 10.1016/j.epsr.2016.06.035.

[19] S. Frank, I. Steponavice, and S. Rebennack, “Optimal power flow: A bibliographic survey I,” *Energy Syst*, vol. 3, no. 3, pp. 221–258, 2012, doi: 10.1007/s12667-012-0056-y.

[20] S. Frank and S. Rebennack, “An introduction to optimal power flow: Theory, formulation, and examples,” *IIE Transactions*, vol. 48, no. 12, pp. 1172–1197, 2016, doi: 10.1080/0740817X.2016.1189626.

[21] J. K. Skolfield and A. R. Escobedo, “Operations research in optimal power flow: A guide to recent and emerging methodologies and applications,” *European Journal of Operational Research*, vol. 300, no. 2, pp. 387–404, 2022, doi: 10.1016/j.ejor.2021.10.003.

[22] Zhifeng Qiu, Geert Deconinck, and Ronnie Belmans, *A Literature Survey of Optimal Power Flow Problems in the Electricity Market Context*. New Jersey.

[23] D. Stanelyte and V. Radziukynas, “Review of Voltage and Reactive Power Control Algorithms in Electrical Distribution Networks,” *Energies*, vol. 13, no. 1, p. 58, 2020, doi: 10.3390/en13010058.

[24] M. Vukobratović, P. Marić, G. Horvat, Z. Balkić, and S. Sučić, “A Survey on Computational Intelligence Applications in Distribution Network Optimization,” *Electronics*, vol. 10, no. 11, p. 1247, 2021, doi: 10.3390/electronics10111247.

[25] J. Momoh, *Smart Gird: Fundamentals of Design and Analysis*: Wiley-IEEE Press, 2012.

[26] S. K. Rathor and D. Saxena, “Energy management system for smart grid: An overview and key issues,” *Int J Energy Res*, vol. 44, no. 6, pp. 4067–4109, 2020, doi: 10.1002/er.4883.

[27] R. C. Bansal, “Optimization Methods for Electric Power Systems: An Overview,” *International Journal of Emerging Electric Power Systems*, 2005.

[28] F. Capitanescu, “Critical review of recent advances and further developments needed in AC optimal power flow,” *Electric Power Systems Research*, vol. 136, no. 3, pp. 57–68, 2016, doi: 10.1016/j.epsr.2016.02.008.

[29] B.-G. Risi, F. Riganti-Fulginei, and A. Laudani, “Modern Techniques for the Optimal Power Flow Problem: State of the Art,” *Energies*, vol. 15, no. 17, p. 6387, 2022, doi: 10.3390/en15176387.

[30] Shaojun Huang, Konstantin Filonenko, and Christian T. Veje, “A Review of The Convexification Methods for AC Optimal Power Flow,” *2019 IEEE Electrical Power and Energy Conference (EPEC)*, 2019.

[31] A. Gautam, Ibraheem, G. Sharma, M. F. Ahmer, and N. Krishnan, “Methods and Methodologies for Congestion Alleviation in the DPS: A Comprehensive Review,” *Energies*, vol. 16, no. 4, p. 1765, 2023, doi: 10.3390/en16041765.

[32] M. M. Farag, R. A. Alhamad, and A. B. Nassif, “Metaheuristic Algorithms in Optimal Power Flow Analysis: A Qualitative Systematic Review,” *Int. J. Artif. Intell. Tools*, 2023, doi: 10.1142/S021821302350032X.

[33] M. F. Zia, E. Elbouchikhi, and M. Benbouzid, “Microgrids energy management systems: A critical review on methods, solutions, and prospects,” *Applied Energy*, vol. 222, pp. 1033–1055, 2018, doi: 10.1016/j.apenergy.2018.04.103.

[34] A. F. Zobaa, S. A. Aleem, and A. Y. Abdelaziz, *Classical and Recent Aspects of Power System Optimization*: Elsevier Science, 2018.

[35] A. R. Battula, S. Vuddanti, and S. R. Salkuti, “Review of Energy Management System Approaches in Microgrids,” *Energies*, vol. 14, no. 17, p. 5459, 2021, doi: 10.3390/en14175459.

[36] Udit Mittal, Uma Nangia, and Narender Kumar Jain, “Computational Intelligence-Based Optimal Power Flow Methods-A Review,” *2022 IEEE Delhi Section Conference (DELCON)*, 2022, doi: 10.1109/DELCON54057.2022.9753276.

[37] D. Bienstock, M. Escobar, C. Gentile, and L. Liberti, “Mathematical programming formulations for the alternating current optimal power flow problem,” *Ann Oper Res*, vol. 314, no. 1, pp. 277–315, 2022, doi: 10.1007/s10479-021-04497-z.

[38] Sergio Nesmachnow, “An overview of metaheuristics: accurate and efficient methods for optimisation,” *International Journal on Metaheuristics*, no. 4, 2014.

[39] A. M. Nassef, M. A. Abdelkareem, H. M. Maghrabie, and A. Baroutaji, “Review of Metaheuristic Optimization Algorithms for Power Systems Problems,” *Sustainability*, vol. 15, no. 12, p. 9434, 2023, doi: 10.3390/su15129434.

[40] D. H. Wolpert and W. G. Macready, “No Free Lunch Theorems For Optimization,” *IEEE Transactions on Evolutionary Computation*, no. 1, pp. 67–82, 1997, doi: 10.1109/4235.585893.

[41] A. K. Khamees, N. M. Badra, and A. Y. Abdelaziz, “Optimal Power Flow Methods: A Comprehensive Survey,” *International Electrical Engineering Journal (IEEJ)*, no. 7, 2016.

[42] A. Corominas, “On deciding when to stop metaheuristics: Properties, rules and termination conditions,” *Operations Research Perspectives*, vol. 10, p. 100283, 2023, doi: 10.1016/j.orp.2023.100283.

[43] G. Chicco and A. Mazza, “Metaheuristic Optimization of Power and Energy Systems: Underlying Principles and Main Issues of the ‘Rush to Heuristics’,” *Energies*, vol. 13, no. 19, p. 5097, 2020, doi: 10.3390/en13195097.

[44] M. A. A. Rahman, B. Ismail, K. Naidu, and M. K. Rahmat, “Review on population-based metaheuristic search techniques for optimal power flow,” *IJEECS*, vol. 15, no. 1, p. 373, 2019, doi: 10.11591/ijeecs.v15.i1.pp373-381.

[45] Nidhal Kamel Taha El-Omari, “Sea Lion Optimization Algorithm for Solving the Maximum Flow Problem,” *IJCSNS International Journal of Computer Science and Network Security*, 2020, doi: 10.22937/IJCSNS.2020.20.08.5.

[46] Zia Ullah *et al.*, “A Mini-review: Conventional and Metaheuristic Optimization Methods for the Solution of Optimal Power Flow (OPF) Problem,” *AINA 2020*, 2020.

[47] S. Frank, I. Steponavice, and S. Rebennack, “Optimal power flow: A bibliographic survey II,” *Energy Syst*, vol. 3, no. 3, pp. 259–289, 2012, doi: 10.1007/s12667-012-0057-x.

[48] Leonel M. Carvalho *et al.*, “Statistical tuning of DEEPSO soft constraints in the Security Constrained Optimal Power Flow problem,”

[49] A. Ramadan, M. Ebeed, S. Kamel, and L. Nasrat, *Uncertainties in Modern Power Systems.: Optimal power flow for distribution systems with uncertainty*: Elsevier Inc., 2021.

[50] K. N. Hasan, R. Preece, and J. V. Milanović, “Existing approaches and trends in uncertainty modelling and probabilistic stability analysis of power systems with renewable generation,” *Renewable and Sustainable Energy Reviews*, vol. 101, no. 2100, pp. 168–180, 2019, doi: 10.1016/j.rser.2018.10.027.

[51] Mohamed Ebeed and Shady H. E. Abdel Aleem, *Uncertainties in Modern Power Systems.: Overview of uncertainties in modern power systems: uncertainty models and methods*: Elsevier Inc., 2021.

[52] E. Acar, G. Bayrak, Y. Jung, I. Lee, P. Ramu, and S. S. Ravichandran, “Modeling, analysis, and optimization under uncertainties: A review,” *Struct Multidisc Optim*, vol. 64, no. 5, pp. 2909–2945, 2021, doi: 10.1007/s00158-021-03026-7.

[53] M. Aien, M. Rashidinejad, and M. F. Firuz-Abad, “Probabilistic optimal power flow in correlated hybrid wind-PV power systems: A review and a new approach,” *Renewable and Sustainable Energy Reviews*, vol. 41, no. 3, pp. 1437–1446, 2015, doi: 10.1016/j.rser.2014.09.012.

[54] L. A. Roald, D. Pozo, A. Papavasiliou, D. K. Molzahn, J. Kazempour, and A. Conejo, “Power systems optimization under uncertainty: A review of methods and applications,” *Electric Power Systems Research*, vol. 214, no. 6, p. 108725, 2023, doi: 10.1016/j.epsr.2022.108725.

[55] R.H.A. Zubo, G. Mokryani, H.-S. Rajamani, J. Aghaei, T. Niknam, and P. Pillai, “Operation and planning of distribution networks with integration of renewable distributed generators considering uncertainties: A review,” *Renewable and Sustainable Energy Reviews*, vol. 72, no. 3, pp. 1177–1198, 2017, doi: 10.1016/j.rser.2016.10.036.

A Comprehensive Study of the Full Grid Forming Direct Voltage Converter Control

Mahshid Maherani
Institute of Electrical Energy Systems
University of Duisburg-Essen
Duisburg, Germany
mahshid.maherani@uni-due.de

Jens Denecke
Institute of Electrical Energy Systems
University of Duisburg-Essen
Duisburg, Germany
jens.denecke@uni-due.de

Hendrik Vennegeerts
Institute of Electrical Energy Systems
University of Duisburg-Essen
Duisburg, Germany
hendrik.vennegeerts@uni-due.de

***Abstract*—The development of a grid-forming converter control is associated with variety of potential challenges, for which different solutions have been reported such that each solution usually studies a specific stand-alone challenge and/or experimental setup. This makes it difficult to get an overview of the capabilities of a grid-forming control method, especially since it is often not possible to generalize a used parameterization and test environment, and hence the obtained insights, in one study for others. This work performs a comprehensive investigation of the full-grid-forming direct voltage control (DVC) via EMT simulations in a representative 16-machine test system. Applied test scenarios reflect the challenges for grid forming converter control, especially current limitation even during transient changes of voltage magnitude or angle at the connection point to the grid. Moreover, the tests address the expected benefit for the system stability like contribution to momentary reserve, transient voltage support during short circuits in the grid, islanding operation as well as system restoration to ensure that the control structure, controller parameters, and test system remain unchanged to show the stability and robustness of the full-grid-forming DVC and thereby indicate practicability in the mass application.**

Keywords—Power converter, grid forming, grid-forming, GFC, direct voltage control, DVC, virtual inertia, inertia, converter

I. INTRODUCTION

The transition to converter-based renewable energy resources presents new challenges for power system stability and operation. Converter based resources have very little internal energy storage, which means they cannot provide the physical inertia or synchronization torque, nor can they deliver short-circuit currents appreciably greater than their rated current [1,2]. Currently, synchronous generators (SGs) are dominating the electrical grid, establishing a stable voltage and frequency that allow for voltage source converters (VSCs) to be synchronized at the point of common coupling (PCC) through a phase-locked loop (PLL) and injecting the power into the grid. These converters are characterized as “grid-following” VSCs and behave similar to current sources. However, since the installation of these generating units is rapidly increasing, some synchronous areas might occasionally operate without synchronous machines (SM)s. In such conditions, and since the converter-based grid-following concept is not able to form an instantaneous AC voltage [3], the system may lose synchronism which can lead to unstable operation. As a result, electrical power can no longer be provided to loads. Therefore, the present operation mode is dramatically changed, while the grid stability still has to be ensured with the same level of reliability as today, or better. To operate autonomously, the control law should be changed. Power converters need to change from following the grid to leading the grid behavior [4]. This capability is known as the "grid-forming" concept, where power converters are able to generate an AC voltage with a given amplitude and frequency at the PCC. Different from grid-following converters (GFL)s, grid-forming units behave as voltage sources, which possess a number of superior features, such as the black-start (BS) capability, the enhanced synchronization performance in weak grids, and the rate of change of frequency (RoCoF) support [5,6].

A. State-of-the-art and drawbacks

To implement a grid-forming control, an intuitive solution is to operate VSCs in a similar way as SGs. Various control schemes have thus been proposed during the last years. The first explicit proposal for a "Virtual Synchronous Machine," labeled VISMA, incorporated a full-order model of a SM as part of the control system. The voltage measurements at the PCC were used as input to an internal model, providing the currents that would have been produced by a real SM. Grid-forming converter (GFC) control emulation was then achieved by imposing these currents as reference values for hysteresis current controllers. The same approach can also be adapted to reduced order SM models [7-14]. The simplest GFC control implementations emulate only the inertia and damping of a SM, represented by the traditional mechanical swing equation [15,16]. The position of the virtual rotor inertia from the swing equation is then combined with a reactive power controller to directly provide output voltage references for pulse width modulation (PWM) signal generation [14,16]. This open loop approach ensures a simple control system structure, but complicates the implementation of current limiters and protection features in case of grid faults and other severe transients. Unlike GFLs that behave as current sources, GFCs are very sensitive to external disturbances. Indeed, due to the voltage source behavior of a GFC, the over-current protection deserves a specific attention [17-19]. Compared to SGs that can support up to higher multiple times over their rated current, power converters can only cope with a few percent of over-current. Trying to mimic SM would require a very large over-sizing of semiconductor components and induce large additional costs. Therefore, power converters have to be protected against extreme events as short circuits and also against other events which may induce small over-current such as phase shift, connection of large loads, and tripping of a line [20]. To avoid the drawbacks of GFC control implementations based on open loop voltage control, the voltage references determined by the inertia emulation and the reactive power control can be input to an inner control structure with

cascaded voltage and current controllers to regulate output AC voltage and converter output current [14]. This approach is similar to the common micro-grid control architectures where active and reactive power droops provide the references for inner cascaded voltage and current controllers [14,21,22]. Current and voltage limitations can be explicitly implemented to protect the converter from over-currents and to avoid unintended over-modulation. Despite the advantages offered by inner cascaded voltage and current controllers, the resulting control schemes can be difficult to tune due to the relatively high number of controller parameters and the potential interaction between the loops. Detailed analysis of the controller tuning is therefore needed for ensuring overall system stability [22].

In contrast to the reviewed state of the art, this paper presents GFC 'direct voltage control' (DVC) including modeling and new developments and application in power systems. Additionally, this article examines a range of potential challenges and solutions as part of a comprehensive control package. DVC control scheme has already achieved good results in various applications ([23]-[25]), including its efficacy in stabilizing grid voltage for an offshore wind farm in the event of sudden blocking of the HVDC offshore converter [19]. In terms of structure and operation, the DVC resembles classical converter controls (GFL) in rotating d/q-coordinates, but avoids the use of proportional, Integral (PI) current controllers, which gives the DVC a voltage source behavior instead of a previously current source behavior. This similarity to classical converter control offers the advantage that many well-known principles from classical converter control can be applied to DVC, so DVC is not a completely new technology with its associated uncertainties. Furthermore, implementing d/q-coordinates within control presents numerous advantages over stator coordinate systems, which are used in some other grid-forming control schemes. These advantages include decoupled control of active and reactive power. Additionally, the DVC converter output voltage can be formed directly from the internal current while also utilizing the measured grid voltage via Kirchhoff equations. Overall, the DVC has limited tuning parameters that have to be set empirically for specific applications, even for a wide range of applications and under changing conditions at the PCC without the need for additional tuning.

B. Contributions

The main contributions of this paper are summarized with comprehensive problem definition as well as proper solutions as follows:

1) *Separated DVC synchronization and Inertia provision control loops*

Recently, GFC controls are classified by the way the frequency of their output voltage is formed (synchronization with grid). The majority of GFC controls such as droop control, virtual synchronous machine (VSM), and oscillator-based techniques shape the converter frequency based on AC variables such as current, voltage, and output power [26, 27]. Another class of GFC controllers sets the converter frequency proportional to a linear/ nonlinear DC feedback. More recently, the trend has been toward multi-variable control, where DC and AC information is combined in setting the GFC control frequency [27]. These control methods have already shown good results in various publications which are different in their complexity, tuning and robustness.

This paper provides details on the implementation of grid forming DVC. Different ways of synchronization with the grid can be applied for DVC. Focusing here on grid forming DVC that utilizes AC voltage and power measurement feedback to define the converter frequency. The actual estimated grid frequency ω_{grid} from voltage-based synchronization is used to compensate a virtual slow mechanical speed of the power-based synchronization. Additionally, the task of synchronizing the converter to the grid and providing virtual inertia through two separate control functions allowing specific tuning of each function, avoiding the necessity to find any kind of trade-off between the quality/speed of synchronization and inertia provision.

2) *DVC's current limitation*

During weak and faulty grid conditions, the synchronization instability will be inevitable by violating the maximum static power transfer between the converter terminal bus and the grid. This limitation is present for any control structure (GFL and GFC) and is a condition for the existence of equilibrium points in the system. Therefore, this limitation is a necessary stability condition, ensuring that the converter operation represents a stable operation point [17, 28, 29]. GFC control, functioning as a controlled voltage source cannot directly control or limit the current by adding a saturation block at the current reference like GFL controller. This creates a conflict with strict current limits in case of changing terminal voltages. Moreover, a straightforward limitation of the output current without impact on the internal control may cause instabilities in the control itself, e.g. similar to transient angle instability of SG. Different studies have considered similar current limitation concepts including, derivatives of reference quantities [31], virtual impedances [32, 33], switching to phased locked loop (PLL)-based controllers [34], switching to current controllers [35, 36], switching to hysteresis controllers [37] or hardware current limiting (current clipping) [38]. However, many of these current limitations showing drawbacks, as discussed e.g. in [38]. Virtual impedances can promote unwanted interactions between neighboring GFCs, switching takes away robustness and observability from the system and current clipping causes strong harmonics, so it should only be used for short periods of time to catch current peaks [38, 39]. DVC incorporates current limitation based on fast voltage control or the angle of the grid impedance φ_z seen by the converter. Both fault ride-through (FRT) control strategies have been proposed which are easy to implement and avoid the previously mentioned drawbacks.

3) *DVC measurements filtering and harmonic rejection*

In this work, the basic concept of the fundamental DVC control method is derived from a two-stage sliding Fourier transform (SFTSFT) filter, which consists of a fixed window-width SFT in the first stage is used to drive the variable window-width SFT in the second stage. The three-phase voltage and current signals measured at the PCC are converted into control values using SFT-SFT as an input filter. The salient advantage for SFT-SFT method is its

excellent harmonic rejection. This is due to the front-end stage which adjusts the frequency of the second stage and thus forces it to operate in nominal frequency mode. The proposed SFT-SFT has a fixed sampling rate, hence it complies with the requirements of common digital controller [40].

The remaining work is organized as follows: Section 2 presents the converter model description, while Section 3 outlines the structure of SFT-SFT as an input filter for signal measurement to use in DVC. The control loops, proposed decoupled virtual inertia (rate of change frequency RoCoF) and synchronization are presented in Section 4. Section 5 presents the main control (outer and inner) loops of DVC. The issues of GFC control during faults as well as proposed current limitations for grid forming DVC are described in Section 6. Section 7 presents several case studies to show the functionality of proposed GFC-DVC loops.

II. Modelling description

A. Simplified model of power converter

In this work, the machine side converter (MSC) and wind turbine generator, battery or PV parts are neglected. In terms of grid dynamics, there will be the focus on the grid side converter (GSC). However, the chopper and DC circuit has been included in the model, so that the dynamics of the DC circuit can be observed and are well represented. The simplified model of the converter is shown in Fig. 1 assuming constant active power injection of the MSC into

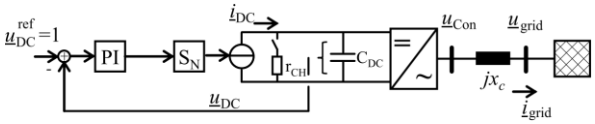

Fig. 1. Simplified electrical model design

the DC circuit. The model utilizes an average model of a two-level three phase converter for GSC with a common LC output filter which is summarized to jx_c. The DC-link voltage (u_{DC}) control in this model is handled by a PI-controlled current source. The parameters of the proportional-integral (PI) controller correspond to typical values in order to approximate realistic DC link dynamics. The power balance between the MSC and GSC in this model is governed by (1).

$$\begin{aligned}\frac{du_{DC}}{dt} &= \frac{1}{c_{DC}} \cdot i_{DC} \\ &= \frac{1}{c_{DC}} \cdot \left(i_{GSC,DC} - i_{MSC,DC} - i_{CH}\right) \\ &= \frac{1}{c_{DC} \cdot u_{DC}} \cdot (-p_{GSC} - p_{MSC} - i_{CH}) \end{aligned} \quad (1)$$

The chopper will dissipate the excessive energy if the DC circuit voltage rises above threshold value. The time constant of the DC link is calculated by using (2). This time constant represents the duration that the DC capacitor is able to provide power before being depleted during a disturbance.

$$\tau = \frac{1}{2} \cdot \frac{c_{DC} \cdot u_{DC}^2}{s_N} \quad (2)$$

The power depleted by the chopper/crowbar is given by the logic in (3).

$$p_{CH} = \begin{cases} 0 & \text{if chopper is off} \\ \frac{u_{DC}^2}{r_{CH}} & \text{if chopper is on} \end{cases} \quad (3)$$

Where u_{DC} and r_{CH} describe the rated DC voltage and chopper resistance in p.u. of the converter.

B. Grid-forming DVC Concept

Grid forming DVC could be implemented on both, MSC and GSC. Given the model in A, the output voltage u_{Con} of the GSC in combination with the actual grid voltage u_{grid} will be given by Kirchhoff equations (4).

$$\begin{aligned} u_{Con} &= u_{grid} + jx_c \cdot i_{grid} \\ \Delta u_{Con} &= jx_c \cdot i_{grid} \end{aligned} \quad (4)$$

DVC utilizes the d/q-coordinate-system with the appropriate angle θ_{sync} (based on its synchronization), which is described in detail as follows. Eq (4) can be rewritten then to (5, 6):

$$\begin{aligned} u_{Con,d} &= |u|_{grid} + \Delta u_{Con,d} \\ &= |u|_{grid} - x_c \cdot i_{grid,q} \end{aligned} \quad (5)$$

$$\begin{aligned} u_{Con,q} &= \Delta u_{Con,q} \\ &= x_c \cdot i_{grid,d} \end{aligned} \quad (6)$$

Primary control objective of the DVC is the control of active (p) and the reactive power (q) of converter at the PCC while maintaining a voltage source behavior. Hence direct control of the voltage drop across the choke (x_c), which allows for control of both active and reactive power flow, as well as indirect control of active and reactive current. DVC is considered as partial and full GFC control (based on synchronization) scheme. The total control concept will be discussed in detail in next sections. DVC, like any other GFC, offers two degrees of freedom: the angle θ_{sync} and the magnitude of the modulation signal. The angle for the modulation signal, θ_{sync}, is determined through power balance and voltage synchronization. The modulation signal magnitude is obtained through DVC outer and inner control loops as well as current limitation. In combination these signals are used to form the converter output voltage u_{Con}.

III. Two-Stages Sliding Fourier Transform (SFT–SFT) Filter Structure

The measurement concept of the fundamental DVC method is derived from SFT–SFT filtering which is shown in fig. 2. This method involves the use of two stages sliding Fourier transform (SFT). The voltage and current signals $u_{grid,abc}$, $i_{grid,abc}$, measured at PCC from fig. 1 are calculated using SFT–SFT input filter from fig. 3. The two-stage SFT gives excellent performance at nominal frequency operation. However, at off-nominal frequency, it generates errors in both magnitude and phase angle due to spectral leakage. Two-stage SFT is applied during off-nominal frequency operations at a fixed sampling rate to correct any associated drawbacks during this operation point. A fixed window-width SFT in the first stage is used to drive the variable window-width SFT in the second stage. The SFT–SFT assigns a filter characteristic on the voltage and current signals that serve to calculate the symmetrical components for converter control. According to fig. 2, the first SFT stage with a predefined filter frequency ($f_n = 50Hz$) can be used to effectively determine the unknown grid frequency (f_{grid}). Once the grid frequency was determined, a second stage SFT can use this frequency as its

own filter frequency (f_n). In this case, the second stage will run at the nominal frequency mode except for the short transitional periods and thus enjoys all the strengths of SFT specially the near-zero spectral leakage. Near zero because the adjustment of the filter frequency subjects to finite increment/ decrement step which is decided by the sampling frequency. Also, the estimated period is translated into integer discrete number of samples and the fractions are truncated. Recalling that the above analysis considers some presumptions (constant frequencies, pure sinusoidal input, and three phase balanced voltages), it is expected that violating these assumptions would render the results invalid. However, the results are still valid due to the following reasons:

1. Fourier transform has excellent harmonic rejection at nominal operation, therefore, having a distorted grid voltage may have no effect on the second stage. The effect on the first stage will show itself in the form of high frequency ripples imposed on the estimated frequency from the first stage, these ripples can be greatly attenuated by simple moving average filter. This may slightly reduce the dynamic response of the whole system.

2. The filter phase angle and the summing process are so designed to extract only the positive sequence component of the three-phase grid voltage. Therefore, the designed structure is highly immune against grid voltage unbalance.

3. Slow variation in the grid frequency doesn't entirely invalidate the assumption of constant frequency particularly in the short term. However, it triggers transient behavior that quickly decays to zero.

The first SFT stage in Fig. 2 is responsible for providing an estimate ($\hat{f}_{grid,i}$) of the actual frequency of the grid voltage. The estimated frequency ($\hat{f}_{grid,if}$) is filtered using a moving average filter (MAF) to attenuate the high frequency ripples due to spectral leakage (resulting from possible harmonic distortion). For the tap size of the MAF, it is a compromise between the filtering quality and the dynamic responsiveness of the overall measurement. The larger the tap size, the better the filtering quality of the estimated frequency ripples, but the slower the dynamic tracking response. The MAF's output ($\hat{f}_{grid,if}$) is then fed to the second stage where it controls the delay duration.

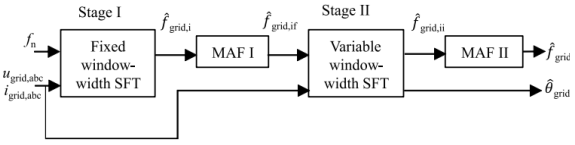

Fig. 2. Concept of two-stage SFT filtering

The second stage in Fig. 2 is similar to the first stage in every aspect except for the following features. In order to be frequency adaptive, it is equipped with variable-delay blocks instead of the fixed-delay ones. The filtered frequency ($\hat{f}_{grid,if}$) is used to adjust the delay period of these delay blocks. Since the algorithm is designed for implementation on digital signal processors that runs at fixed sampling rate F_s. The delay process is simply made by using adjusted length buffers. For an estimated grid frequency of ($\hat{f}_{grid,if}$), the number of samples included in the buffer at any time will be equal to the rounded result of $\frac{1}{F_s \cdot \hat{f}_{grid,if}}$. Therefore, the number of samples included in the buffer (which represents the variable window size) is continually adjusted by the estimated grid frequency which is in turn updated on every execution step. The filtered frequency ($\hat{f}_{grid,if}$) is integrated to generate the filter phase angle that is driving the sine/cosine filters of the second stage SFT. The differential phase angle resulting from the second stage is added to the filter phase angle to get ($\hat{\theta}$) which is the closest estimate to the grid positive sequence phase angle. As shown in Fig. 2, the output frequency of the second stage ($\hat{f}_{grid,ii}$) may also MAF filtered to obtain a smoother estimate of the frequency of the grid ($\hat{f}_{grid}$) [40].

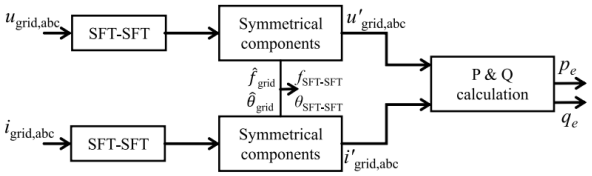

Fig. 3. Filtered measurements with two-stage SFT

IV. CONCEPT OF SYNCHRONIZATION AND INERTIA

A. *Synchronization*

One of the most critical issues is the synchronization of the GSC to the grid. The detection of the fundamental positive sequence frequency component of the grid under unbalanced and distorted conditions is a crucial aspect for establishing and maintaining synchronization. The synchronization of the GSC to the grid can be defined as the process of minimizing the difference in the phase, the frequency and the magnitude between the GSC output voltage and the grid voltage under consideration of the desired apparent power output. An ideal synchronization technique should promptly respond to any grid changes, well-track the phase angle of the grid, adeptly detect any variation in the grid frequency and effectively isolate the harmonic components and disturbance from the fundamental waveform. There are various techniques found in the literature used for tracking the phase angle of the grid voltage and based on grid voltage, e.g. the zero-crossing detection method (ZCD), space vector filter (SV) method, Kalman filter method, recursive weighted least-square method, instantaneous symmetrical component method, phase locked loop methods (PLL), discrete Fourier transform (DFT), Sliding discrete Fourier transform (SDFT) and Two-Stages Sliding Fourier Transform (SFT–SFT). These methods vary in the degree of complexity, the speed of response and the quality of tracking to the utility voltage changes [40].

Thus, the estimated phase angle and frequency ω_{grid} of grid connected converters from mentioned methods (voltage-based) are not a product of power control. This implies that they cannot be stabilized or controlled externally by intervening in the power balance of the grid, like SGs. Furthermore, there is no internal stabilization of the frequency of the voltage-based synchronization.

Basically, GFL controls use voltage-based synchronization to measure the angle and frequency of the line voltage. In principle, high percentage of converter-based generation,

requires grid-forming elements in the grid. These converters ensuring that the grid-following controlled converters can align themselves. In practice, however, several other aspects such as reliability and stabilization of the grid-forming component, redundancy, expansion of the grids, provision of inertia, system-split scenarios and the need for fast controllable reactive power, have to be considered.

GFC controls artificially establish a relationship between power and frequency, which does not exist in voltage source converters for technological reasons. Using the swing equation, the difference between a virtual mechanical power p_m which is considered as a constant amount in this study, and the actual electrical output power p_e of the inverter determines the change in frequency and therefore angle of the inverter output voltage. This is changed until both input signals are identical. In this way, the power control of conventional power plants is reproduced and, in principle, the same conditions regarding power and frequency control or stabilization apply as for SGs [14].

However, the importance of virtual inertia in this process is not only determined by its presence, but also by its duration. It should be noted that the duration of virtual inertia is in direct contradiction to the desirable high damping in synchronization. Therefore, to develop effective GFCs, a compromise between inertia and damping is necessary. This will prevent the optimal design of one of the two functions, leading to suboptimal performance for inertia provision or synchronization.

Moreover, the stored energy E_{kin} in the virtual as well as in the real mechanics depends on the velocity ($E \sim \omega^2$). In either case, inertia provision by grid forming control has to be independent parameterizable from the power-based synchronization control loops in order to be adjustable to the characteristics of the primary energy source linked to the DC-side via MSC. Unlike the physical rotating mass in an SG, excess energy (the difference between provided (virtual) mechanical and realized electrical power) does not need to be stored in virtual inertia due to the designed control structure rather than actual physical behavior. Additionally, real inertia absorbs and provides energy as needed, but in a weakened grid, injecting energy back into the grid may not be desirable. A designed digital control system eliminates this need. [1, 2, 41, 42].

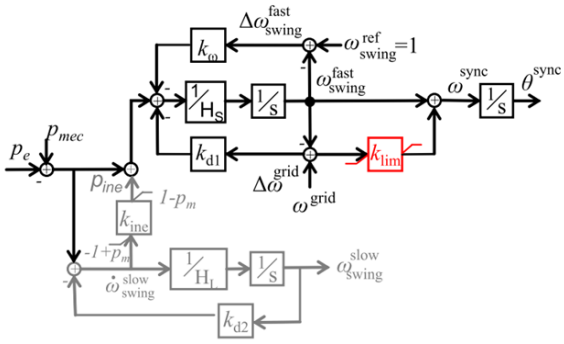

Fig. 4. Seperated synchronization and RoCoF control loop for GFC DVC

In this work, a synchronization according to fig. 4 is proposed, which consists of two swing equations. The first one - called fast swing equations (fig. 4, $H_S, k_{d1}, k_\omega, k_{\lim}$) - serves mainly the purpose of a strongly damped power-based synchronization and provides only very limited virtual inertia. A virtual inertia is provided by the second swing equation, also known as the slow-swing equation (shown in Figure 4, H_L, k_{d2}), which is less damped and requires a longer transient process to deliver synchronizing energy. This division has the advantage that these control functions, separated in this way, can each be optimized specifically for their purpose and thus no tradeoff between the individual functions (inertia and frequency control vs. synchronization) has to be made in the overall behavior of the synchronization [42, 44].

B. Fast damped DVC synchronization loop

The synchronization of the converters should ideally be as fast as possible by maintaining robust results, ensuring fast clearance of transient dynamic deviations in angle and magnitude to not additionally endanger converter or grid stability.

In this study, for DVC GFC (as well as other types of GFC), voltage-based synchronization will be combined with power balance-based synchronization to address each of their deficiencies. The quick, instantaneous and robust estimated phase angle and frequency of voltage-based synchronization under unbalanced and distorted grid conditions, come up with slow inertial nature of power-based synchronization which is implemented by swing equation that stabilize and control the grid externally and internally. Mainly, the synchronization control loop of DVC is intended to serve the purpose of fast power-based synchronization. The synchronization is based on the swing equation, representing the inertia and damping of a SG. The swing equation used for the implementation is linearized with respect to the speed so that the acceleration of the inertia is determined by the power balance according to (7).

$$H_s \cdot \frac{d\omega_{swing}^{fast}}{\mathrm{dt}} = p_m - p_e - p_\omega - p_d \qquad (7)$$

In this equation, p_m is the virtual mechanical input power, p_e is the measured electrical power fed from the converter into the grid, p_d is the damping power with high damping factor which works with respect to the grid frequency ω_{grid} , which is derived from accurate voltage-based synchronization and p_ω is a damping and stabilization term that works with respect to a fixed speed reference, ω_{ref}^{swing}. The mechanical time constant is defined as $2 \cdot H_S = T_{a,fast}$ and is small enough to fulfil fast synchronization. The per unit mechanical speed ω_{swing}^{fast} of the virtual inertia corresponding to small time constant $T_{a,fast}$ is then given by the integral of the power balance while the corresponding synchronized phase angle θ_{sync} is given by the integral of the swing speed ω_{fast}^{swing} and contributed voltage-based synchronization term which is expressed as a feed-forward gain of speed deviation $\Delta\omega_{grid}$ as in (8).

$$\frac{\mathrm{d}\theta^{\mathrm{sync}}}{\mathrm{dt}} = \omega^{sync} = \omega_{swing}^{fast} + k_{lim} \cdot \left(\omega_{grid} - \omega_{swing}^{fast}\right) \qquad (8)$$

According to (8), the fast swing-equation frequency ω_{swing}^{fast} under steady state operation will be equal to the grid

frequency ω_{grid} which is derived by SFT–SFT method. Therefore, the frequency deviation will become $\Delta\omega_{grid} = 0$ and $\omega_{sync} = \omega_{fast}^{swing}$. In case of severe events like short circuit, when phase angle of the grid voltage jumps corresponding to the fault conditions, virtual-low inertial mechanical speed ω_{fast}^{swing} based on power synchronization ($\omega_{slow}^{swing} < \omega_{fast}^{swing} < \omega_{grid}$) may not correct its speed fast enough to avoid over-current (similarity of transient stability of SG). The estimated measured grid frequency ω_{grid} from voltage-based synchronization (faster than fast swing equation) is combined to compensate virtual mechanical speed ω_{fast}^{swing} of the virtual inertia (although $2 \cdot H_S = T_{a,fast}$ is considered small) in comparison to feed forward factor, k_{lim} which will be discussed in detail.

1) *Damping Factors k_{d1} & k_ω*

Damping is a major component of power system stability since it reduces the oscillations after a disturbance. Therefore, it is necessary to tune damping as accurately as possible in order to ensure the applicability of power system stability studies to the actual system behavior. The damping power p_d, representing the damping effect of a SG, is defined by the damping constant k_{d1} and the difference between the virtual synchronization speed, ω_{fast}^{swing} and the actual measured grid frequency ω_{grid}. Thus, an estimate of the actual grid frequency ω_{grid} is needed for power-based synchronization of DVC. As indicated in fig. 4, the frequency estimation (ω_{grid}) is provided by a two-stages sliding Fourier transform (SFT-SFT). Furthermore, the effect of fast and robust synchronization for power-based synchronization in correspond to voltage-based synchronization is achieved by choosing high damping factors k_{d1}.

The damping stabilizing term p_ω works with respect to a fixed speed reference ω_{ref}^{swing}. In many papers only this term is used as damping factor. However, to ensure fast and stable synchronization, this proportional factor must be quite high, leading to strong primary-control-behavior in stationary conditions [2]. Therefore, damping and stabilization may be improved by adding a measurement of the grid frequency ω_{grid} via p_d, avoiding primary control behavior. Indeed, this is still possible by tuning the factor k_ω to a reasonable value much smaller than k_{d1}. By this a frequency droop, equivalent to the steady-state characteristics of the speed governor for a traditional SM as indicated in eq. (9), is included in the power control of the power-based synchronization of DVC control loop as shown in the top part of fig. 4. This power-frequency droop is characterized by the droop constant k_ω working on the delta between a frequency reference ω_{ref}^{swing} and the actual swing speed ω_{fast}^{swing}.

$$\frac{\Delta p}{\Delta\omega_{swing}^{fast}} = k_\omega \tag{9}$$

To avoid undesirably strong primary control behavior of the synchronization as well as stabilizing the state variable ω_{fast}^{swing} of the fast swing-equation, feedback control can be achieved through the factor k_{d1} with $k_\omega << k_{d1}$. Thus, grid-forming behavior of DVC as regards to instantaneous reaction has been introduced on changes of the grid voltage is maintained.

2) *Limit Factor k_{lim}*

By using swing equations for synchronization, transient stability remains an issue in electrical grids, even though it can be improved by high damping components as described in last section. However, operating a GFC near its rated power (1 p.u.) results in minimal remaining current margin for acceleration or deceleration of the virtual inertia. Beyond this threshold, current limitation takes effect. SGs do not experience this issue that strong, allowing them to reduce accelerations more quickly or to decelerate more strongly above their rated power. Therefore, after large 3-phase faults have been cleared, operating states can occur in which virtual swing equations are not able to decelerate strongly enough to catch up with SGs that are also decelerating. The resulting increases in the relative angles of the GFCs to the SGs in the grid leading the converters into current limitation. With active current limitation only a maximum possible relative angle with respect to the grid can be kept constant, which, however, contradicts the dynamics of the swing equation.

In the synchronization concept presented in this paper, the synchronization swing equation is given another possibility to reduce speed before too large relative angles are reached by integrating a voltage-based synchronization, which can significantly improve the dynamic performance of the overall system. For this purpose, the delta ω_{swing}^{fast} between the measured frequency of voltage-based synchronization, $\omega_{grid} = \omega_{SFT-SFT}$ and the frequency of the fast swing-equation is formed and applied to the speed ω_{fast}^{swing} at the output via the feedforward term with k_{lim} (fig. 4). A factor of $k_{lim} = 1$ correspond to a GFL control via voltage-based synchronization and a factor of $k_{lim} = 0$ often applied for a GFC control, synchronized via swing equation. In between, the factor k_{lim} can be empirically adapted to the deployment site of the plant, or to the deployment grid, and still achieve GFC behavior, fast and robust synchronization, and provide inertia. Other advantages of implementing a voltage-based synchronization are, especially in weak grids, voltage-based synchronizations are inherently faster and less problematic than power-based ones, and there is no need for an actual infeed of active power for a voltage-based synchronization.

C. Synthetic RoCoF control loop

The provision of inertia is supposed to stabilize the local grid frequency and limit the local rate of change of frequency (RoCoF). Therefore, active power can be injected/reduces as a kind of RoCoF control proportional to the measured RoCoF. However, gradients are difficult to measure in general and thus only few possibilities are available in the controller design, this work generate an artificial RoCoF by adding a second slow swing-equation (fig. 4, H_L, k_{d2}, k_{ine}), which is less damped contrary to the fast swing-equation. Moreover, this gives the possibility to tune it e.g. empirically, by pole placement or by utilization of an optimal or robust optimization criterion. This less damped behavior is only available by synchronization with the fast swing equation, allowing inertia to be provided over longer periods of time and thus supporting the power

system frequency more effectively. This second slow swing-equation is coupled to the first one (fig. 4) by feeding this synthetic RoCoF signal as an additional input to the first one via proportional gain k_{ine}. Since both swing equations are decoupled, the parameters can be freely adjusted in wide parameter ranges, but stability must be taken into account. Eqs. (10)-(12) give the state-space model of synchronization from fig. 4 suitable for open-loop stability analysis.

$$\dot{\omega} = Ax + Bu \tag{10a}$$

$$y = Cx + Du \tag{10b}$$

$$\begin{bmatrix} \dot{\omega}_{swing}^{fast} \\ \dot{\omega}_{swing}^{slow} \end{bmatrix} = \begin{bmatrix} -\frac{k_{d1}\cdot k_{d2}}{H_S} & -\frac{k_{ine}\cdot k_{d2}}{H_S} \\ 0 & -\frac{k_{d2}}{H_S} \end{bmatrix} \cdot \begin{bmatrix} \omega_{swing}^{fast} \\ \omega_{swing}^{slow} \end{bmatrix} + \begin{bmatrix} \frac{1+k_{ine}}{H_S} & \frac{k_{d1}}{H_S} & \frac{k_{d2}}{H_S} \\ \frac{1}{H_L} & 0 & 0 \end{bmatrix} \cdot \begin{bmatrix} \Delta p \\ \omega_{grid} \\ \omega_{swing}^{ref} \end{bmatrix} \tag{11}$$

$$y = [1 \quad -k_{lim}] \cdot \begin{bmatrix} \omega_{swing}^{fast} \\ \omega_{swing}^{slow} \end{bmatrix} + [0 \quad k_{lim} \quad 0] \cdot \begin{bmatrix} \Delta p \\ \omega_{grid} \\ \omega_{swing}^{ref} \end{bmatrix} \tag{12}$$

V. DVC Outer/ Inner control loops

A. *Park's transform for DVC implementation in dq-frame*

The Park's transformation is the basis for the reference frame representation of three-phase AC systems. It originates from, but is not limited to, SG theory and it consists of the following time-dependent transformation from the actual phase quantities to the dq0 reference frame currents/voltages (13).

$$i_{dq0} = K \cdot i_{abc} \qquad u_{dq0} = K \cdot u_{abc} \tag{13}$$

where the 3x3 transformation matrix is defined as (14) and $\theta = \omega t$

$$K = \begin{bmatrix} \sin(\theta) & \sin\left(\theta - \frac{2\pi}{3}\right) & \sin\left(\theta + \frac{2pi}{3}\right) \\ \cos(\theta) & \cos\left(\theta - \frac{2\pi}{3}\right) & \cos\left(\theta + \frac{2\pi}{3}\right) \\ \frac{1}{2} & \frac{1}{2} & \frac{1}{2} \end{bmatrix} \tag{14}$$

Choosing ω to be the system base electrical frequency in radians per second ($\omega_b = 2\pi f$) the dq frame is rotating at this constant speed and the d- and q-axis projections form the real and imaginary parts of a phasor in the base system frequency. The zero-axis component (i.e., the homopolar one) corresponds to the zero sequence of the classical positive, negative and zero sequence circuit representation. If the three-phase system is balanced and in sinusoidal steady state, the phasor will be constant in the dq frame if the frequency is equal to ω_b. Otherwise, the phasor in the dq frame will rotate with the slip frequency $\omega_b - \omega$. In presence of negative sequence components, the phasor will consist of a constant part and a component rotating at $2 \cdot w_b$. With DC components or second harmonics present in the system, a component rotating at synchronous speed will appear in the dq-frame and so on [43].

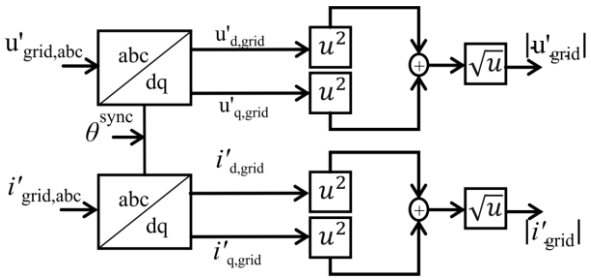

Fig. 5. Park transformation with θ^{sync}

In this study the transformation angle will be calculated by $\theta = \theta^{sync} = \int \omega^{sync}\, dt$ according to fig. 4. This angle will be applied to the transformation according (13-14) for the SFT-SFT filtered measurements, $u'_{grid,abc}, i'_{grid,abc}$ based on fig. 3 resulting in voltages and currents in dq-components as well as their magnitudes according to fig. 5.

B. *DVC Outer loop control*

The internal current references $i_{d,ref}, i_{d,ref}$ are derived from outer loop controllers in d and q channels which is shown in fig. 6.

1) *d-axis control*

The d-axis control is responsible for the slow and fast voltage control according to the assumption of a low R/X ratio of the systems coupling impedances. In this hierarchical approach of fig. 6, the upper-level (secondary) slow-acting controller is responsible for set-point changes for steady-state operation. Here different approaches like Q/U droop control, reactive power control, or power factor control can be implemented. For fig. 6 Q/U droop control is used. $u_{Grid,ref}$ represents not an actual voltage value but can be seen as a reference for the desired reactive power q_{ref} at a desired voltage level u_{grid}^{ref}. The slope k_{qu} of the linear relationship between voltage u and reactive power q can be adjusted based on system requirements for nominal power factors at rated active power and can be determined as (15)

$$k_{qu} = \frac{\Delta q}{\Delta u} \tag{15}$$

The PI controller with dominant slow integrator adjusts the desired reactive power reference q_{ref}. The time constant is chosen in such a way the reactive power provided by the converter does not influence the fast voltage control downstream of the control hierarchy. Under dynamic events (e.g. grid faults, switching actions, etc.) the voltage reference u_{grid}^{ref} is usually in a steady state due to a reasonable time constant of the integrator in the range of 5–30 seconds.

The downstream (primary /local) fast voltage control compares the actual measured magnitude of the grid voltage u'_{grid} with the steady-state voltage reference u_{grid}^{ref}. The gain k_u should have a static proportional gain. The simplest implementation is represented by a proportional controller and receives the output of the secondary controller as an input signal. This block is primarily responsible for grid voltage support during large sudden voltage drops due to grid faults. The response of the primary controller must be fast (less than 30 ms rise time)

and should have significant effect on the proper operation of the digital protection relays. Voltage boosting response by the controller must be based on locally sensed inputs. The proportional gain of the local voltage controller can be determined with (16).

$$k_u = \frac{\Delta i_{grid,q}}{\Delta u_{grid}} \quad (16)$$

The values k_u may range from 2-10 p.u. A value of 2.0, for example, implies that a 50 % voltage deviation results in 1 p.u. reactive current injection ($i_{q,grid}$). Studies have shown that the natural physical response of SMs corresponds with the gain of approx. 4 p.u. [49].

2) *q-axis control:*

The q-axis control in general is responsible for the active power/frequency control, again according to a low R/X ratio of the coupling impedances. In case of partial grid forming DVC (based on only voltage synchronization) the DC voltage PI controller is responsible for balancing the active power flow between DC and AC side of the converter by controlling the DC voltage to its reference $u_{DC,ref}$. The output of the PI controller is added to a feed-forward active power term p_{mec}. Therefore, the PI controller is meant to compensate the difference between the actual active power setpoint and modelling differences. The actual active power reference (sum of both components, fig. 6) will be divided by the actual voltage magnitude to form the active current setpoint $i_{d,ref}$.

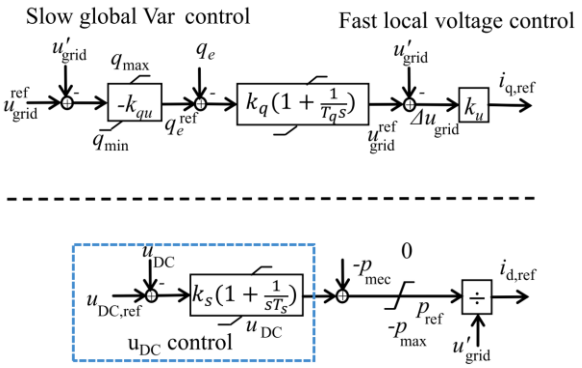

Fig. 6. GFC DVC outer loop control structure with exemplary DC voltage control and Q/U-Droop

C. DVC Inner loop control

The analysis of blocking phenomena on offshore wind parks revealed that voltage rise occurred due to the customarily used control structure for the WT based on current injection. Its integral characteristic of PI current controller causes the converter voltage to reach its maximum value in a short time interval following a mismatch between the reference and the actual values [23, 24]. Fig. 7 demonstrates the fundamental conceptual shift of the DVC structure compared to state-of-the-art current controls. While the integral component of the PI current regulator has been discarded, a proportional component is merely shifted towards the output terminal, which entails only graphical change without implications in terms of performance. In order to limit the effect of this part on the dynamic behavior (similar to the case in the conventional PI controller), this component uses a high-pass washout filter in the new approach. This expansion also opens up the possibility for frequency-selective damping if these terms at the output of the current regulator are augmented by appropriately designed band-pass filters [23, 24]. Details of modified inner current loop of DVC are described in the next sections.

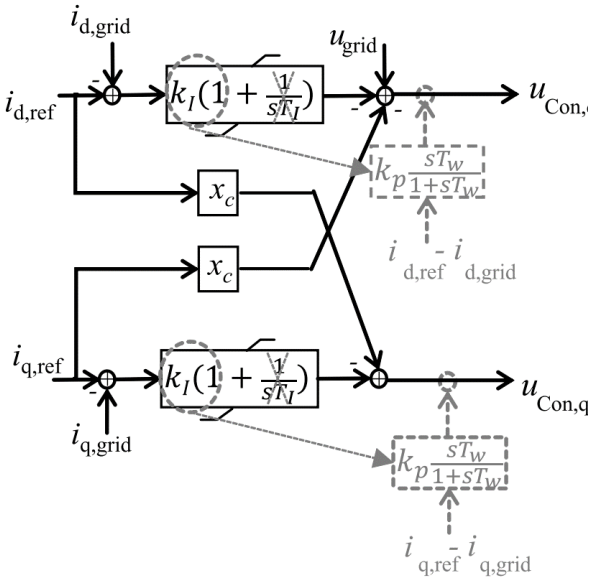

Fig. 7. GFC DVC by modification of the classical GFL current controller

1) *Decoupled control term*

The multiplication of $i_{q,ref}$ and $i_{d,ref}$, as output of active power and voltage control respectively, with the choke inductance x_c result in additional d-axis and q-axis voltage component $\Delta u_{Con,d}$ and $\Delta u_{Con,q}$. They are responsible for the active and reactive power flow of the converter which is shown in fig. 8 in black color.

2) *Feed-forward term*

For completing the voltage mesh of fig. 1 correspond to eq (4) the magnitude of the SFT-SFT filtered magnitude voltage u'_{grid} is added to the control loop in d-axis in black color.

3) *Damping term*

To improve damping in transient periods, virtual resistances r_{vir} (shifted the proportional component k_p from state-of-the-art current controller towards the output terminal, which is shown in fig. 7) are implemented. The damping effect will only be taken into account in transient periods as a result of the high-pass (HP) filters. In static operation it will not be visible (indicated with gray color) [44-48].

Furthermore, 2 different types of current limitations are used in this study are shown with different colors (fig. 8).

- Differential voltages $k_1 \cdot x_c \cdot \Delta i_d$ and $k_1 \cdot x_c \cdot \Delta i_q$ are added as current limitation based on 'fast voltage control' which is shown in red color.
- The green color terms are current limitation, through grid impedance angle φ_Z and dynamic limitation of the additional voltage component derived from the decoupled term which is shown as $\Delta u_{Con,d}^{max,min}$, $\Delta u_{Con,q}^{max,min}$ depending on the $i'_{grid,d}, i'_{grid,q}$.

These two types of current limitations will be discussed in more detail in the next section. According to the damping term and current limitation based on fast voltage control, eq (7)- (8) can be rewritten as eqs. (17-18)

$$u_{Con,d} = u'_{grid} - x_c \cdot i_{q,ref} - k_1 \cdot x_c \cdot \Delta i_q - r_{vir} \cdot HP(s) \cdot \left(i_{d,ref} - i'_{d,grid}\right) - k_u \cdot \left(u_{grid} - u_{ref}\right) \quad (17)$$

$$u_{Con,q} = x_c \cdot i_{d,ref} + k_1 \cdot x_c \cdot \Delta i_d - r_{vir} \cdot HP(s) \cdot \left(i_{q,ref} - i'_{q,grid}\right) \quad (18)$$

In case of current limitation through grid impedance angle φ_Z, differential voltages $k_1 \cdot x_c \cdot \Delta i_d$ and $k_1 \cdot x_c \cdot \Delta i_q$ terms would be omitted from eqs (17-18).

VI. CURRENT LIMITATION

During a fault event, the current drawn from the GFC can increase significantly. In conventional GFL control systems, the current is directly controlled and can be limited to a maximum value, assuming that the voltage-based synchronization e.g. PLL continues to function correctly. However, as GFC is a voltage-controlled model, it cannot limit the output current directly. The current can, however, be limited by indirectly controlling the voltage. In DVC approach the current limitation based on fast voltage control and through the angle of the grid impedance φ_Z seen by the converter as two FRT control strategies have been proposed.

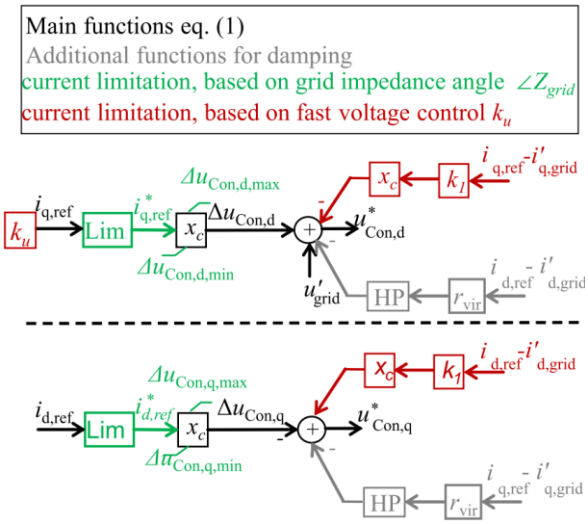

Fig. 8. GFC DVC inner loop control diagram with two possibilities for current limitation (fast voltage control, angle of the grid impedance φ_Z seen by inverter

A. Current limitation based on fast voltage control

When riding through grid short-circuit faults, the remaining grid voltage is often too low to feed-in the desired power. The GFC DVC will not inject reference currents (which are often above the limits) into the grid during the fault. Instead, the FRT operation of the GFC DVC involves increasing the d-component of the inverter output voltage is increased via fast voltage control following fig. 6, to establish a fault current above the inverter's apparent current limit (1.1 p.u.) as a function of the grid impedance x_c. In principle, an increase in the inverter output voltage would be sufficient to produce a fault current of exactly 1.1 pu magnitude, but the fault impedance is initially unknown and thus this voltage magnification cannot be determined beforehand. For this reason, the factor k_u (fig. 6) is selected so large that a fault current greater than 1.1 pu is to be expected, and this is then subsequently limited. For the limitation, difference currents Δi_d and Δi_q are derived from a magnitude limitation, which leaves the angle of the fault current unaffected, turned into difference voltages, and then implemented to eq. (17-18). This results in voltage-based current limitation, since it is interfered with the formation of the inverter output voltage. However, this intervention is only applied to the current components that are above the apparent current limit 1.1 pu, thus keeping the inverter output voltage at the limit and not interfering with the control functions of the GFC DVC itself. Also, no additional controllers or control functions have to be switched on or off. By parameterization of k_1, the intensity of the current limitation intervention can be influenced to improve the dynamic behavior. By selecting $k_1 > 1$ e.g. 1.5, the control action of the current limitation is predominant in comparison with maximum amount of fast voltage control output during fault. The control structure, however, is applicable for other priorities for current limitation as well. The current limiting procedure is as follows:

1) *Magnitude calculation of the actual current eq. (19)* If the magnitude of the actual current exceeds the current limit (e.g. 1.1 pu) then:

2) *Division of the individual current components with the magnitude eq. (20-21)*

3) *Calculating the difference between unlimited and limited component eq. (22-23)*

4) *Entering the current differences in eq. (17-18).*

$$\left|i_{dq}\right| = \sqrt{\left(i'_{d,grid}\right)^2 + \left(i'_{q,grid}\right)^2} \quad (19)$$

$$i_{d,lim} = \frac{i'_{d,grid}}{\left|i_{dq}\right|} \quad (20)$$

$$i_{q,lim} = \frac{i'_{q,grid}}{\left|i_{dq}\right|} \quad (21)$$

$$\Delta i_d = i'_{d,grid} - i_{d,lim} \quad (22)$$

$$\Delta i_q = i'_{q,grid} - i_{q,lim} \quad (23)$$

This current limitation method used for DVC is shown by red color in fig. 8.

B. Current limitation through the angle of the grid impedance φ_Z

This current limitation method used for DVC is demonstrated in fig. 9 and is applied by green color to fig. 8. It consists of two parts. The first part represents a 'current limiting control' which reduces the available maximum current threshold $i'_{grid} = \left|i'_d + j \cdot i'_q - i_{ref}^{max}\right|$ proportional to k_{red} if the current exceeding the maximum current value [48].

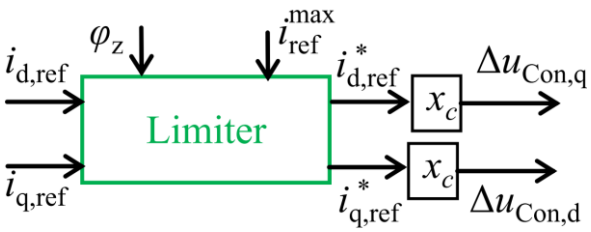

Fig. 9. Current limitation utilizing angle of the grid impedance φ_Z seen by inverter for better voltage support

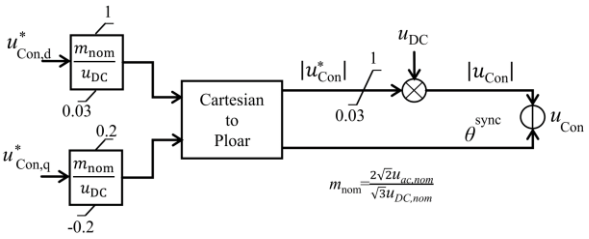

Fig. 10. Example of modulation index limitation

The second part represents the dynamic limitation by 'limitation of the current feed-forward terms'. The new calculated maximum current value i_{ref}^{max} from the first part is used in the limiter block along with the angle of the grid impedance φ_z seen by the power electronic converter to form new current references (fig. 8). The power electronic converter adjusts the reference currents based on the impedance seen by it, thus provides the best possible voltage support. The current limiting procedure, given in (24), follows this procedure:

$$\text{if } \left(\left|i_{d,ref} + j i_{q,ref}\right| - i_{ref}^{max0}\right) > 0 \text{ then:}$$

$$i_{ref}^{max} = i_{ref}^{max0} - k_{red} \cdot \left(\left|i_{d,ref} + j i_{q,ref}\right| - i_{ref}^{max0}\right)$$

$$else\ i_{ref}^{max} = i_{ref}^{max0} \quad (24)$$

$$\varphi_Z = \varphi_{u,grid} - \varphi_{i,grid} \quad (25)$$

$$i_{d,lim} = i_{d,ref}^* = i_{ref}^{max} \cdot \cos(-\varphi_Z) \quad (26)$$

$$i_{q,lim} = i_{q,ref}^* = i_{ref}^{max} \cdot \sin(-\varphi_Z) \quad (27)$$

$$\Delta u_{Con,d} = x_c \cdot i_{q,ref}^* \quad (28)$$

$$\Delta u_{Con,q} = x_c \cdot i_{d,ref}^* \quad (29)$$

1) *Reducing the available maximum current threshold* $i'_{grid} = \left|i'_{d,grid} + i'_{q,grid}\right|$ *proportional to* k_{red} *to the current exceeding maximum current value (24). By this in principle, also short-term overload capabilities can be utilized.*

2) *calculation of the angle of the grid impedance φz (25)*

3) *limiting of the current feed-forward terms (26-27).*

4) *voltage support by means of current limitation (28-29).*

C. Reference voltage limitation

Fig. 10 shows the limitation of the reference voltages $u^*_{Con,d}$, $u^*_{Con,q}$ and the adaptation to the varying DC link voltage. This part is quite manufacturer specific. Therefore, fig.10 represents just one alternative. In this study and the following simulation examples, a two-level three-phase inverter was considered. The modulation index is limited to 1.0 p.u. to avoid additional nonlinear effects. However, the nominal DC voltage is chosen in such a way that the maximum injected converter voltage can reach always 1.155 p.u. at nominal DC voltage. This value is the maximum voltage by using modulation with common mode signal (zero sequence third harmonics) [23].

VII. Simulation Verification of DVC Performance

For the simulative verification of the operation and functional scope, the inverter was operated with the GFC-DVC according to fig. 1. As test-system the PST 16 system was chosen. The PST 16-machine test system consists of three strongly meshed areas, 66 buses, 16 generators, 28 transformers and 51 transmission lines with generation and consumption details which is shown in Tab. 1. This grid has the characteristics of a European grid [50] and it is used to evaluate the comprehensive functionality, stability and robustness of DVC grid forming controller. Matlab/ Simulink is used for the simulations.

A. Black start (BS) & Restoration

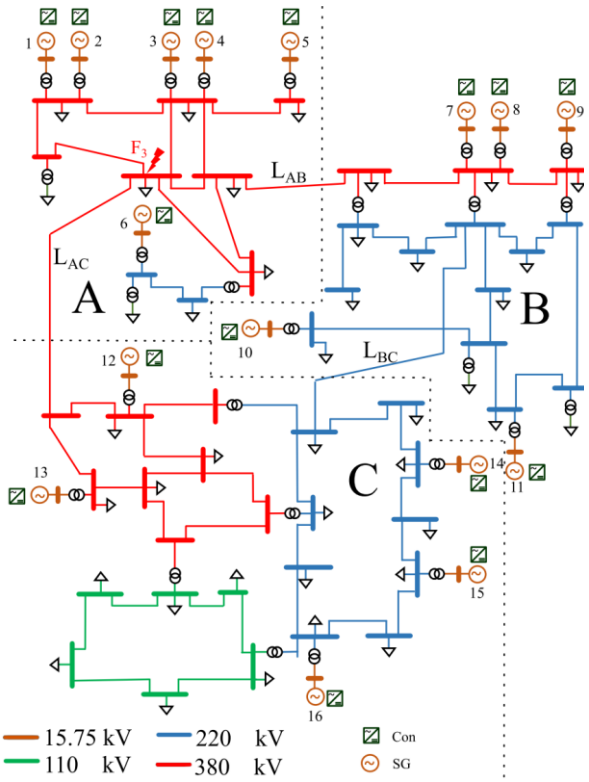

Fig. 11. PST16 test system [50]

Power blackouts are extraordinary events which occurrence has to be avoided as much as possible due to the extremely high economic and social impacts. Large-scale integration of renewable energy sources with power-electronic converters interface with very limited overload capacities results in decreased transient stability. There is a need for converter-based units to be able to start the grid restoration process (black start) and pick up the loads so that the grid can be started to operate again. Load pick-up was originally a task assigned to thermal power plants with assumed sufficient primary energy storage. Black start (BS) and energization of first parts of network is a task of either pump storage hydro power stations or gas turbines. In a fully renewable generation system, the gas turbines as long

Tab. 1. PST16 load and generation

Grid area	Load [MW]	Generation [MW]
A	2000	4840
B	6100	5640
C	7465	5450
Total	15565	15930

as not fired with bio-gas may be supposed to be substituted as well. The BS capability of GFC may be a huge contribution to a variety of additional options for the system control/start in case of blackouts. BS is the procedure to recover from a total or partial shutdown of the transmission system, which has caused an extensive loss of supplies. Large scale renewable energy resources with full-scale converters which are connected at the transmission level have the potential to cope with the huge reactive power needs of grid energization (mainly long cables & lines), withstand transformer inrush transients and provide the possibility to be controlled dynamically for BS needs [25, 51]. This section evaluates the DVC GFC control restoration's functionality and stability when full blackout event occurs for PST 16 grid. The operational stages of the DVC, namely startup and island operation, picking up load, synchronization of more DVCs and load sharing between present DVC units are studied for a part of grid in fig. 12 in one simulation run.

1) *Startup mode (island operation)*

Battery energy storage systems (BESS) have a major role to BS capability. The BESS/ kick starter as a BS resource can start without support from the grid or additionally primary ressources. In this scenario, the BESS with 5 MVA power rating is activated at t = 0 s, which is equipped with the GFC DVC. During the synchronization in startup mode the battery operates at no load conditions and is initialized with synchronization control loop fig. 4 which is characterized by power-frequency droop control and the droop constant k_ω acting on the difference between ω_{swing}^{ref} and ω_{swing}^{fast} . The purpose is to show the startup capability of DVC GFC control. Considering k_ω of 5% in all scenarios (similar to primary controller of SG). In the short period of startup, due to the expected higher frequency deviation, k_ω is considered 15 times less (as an exceptional case).

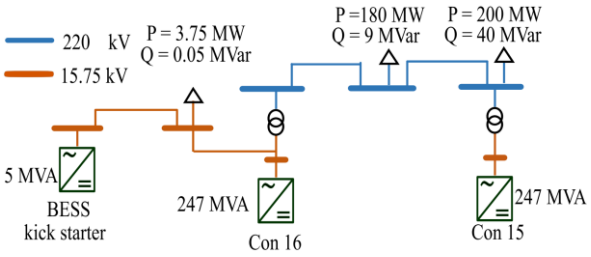

Fig. 12. Test grid section for BS & restoration scenario

2) *Pick up load (island operation)*

A certain level of load on the generator unit is a necessary condition for its successful synchronization with the next generator unit and to reduce the possibility of tripping after synchronization. During the process of loading process, it is interesting to find out the proper load to be connected at any given moment so that the resulting voltage and frequency drops are not too high as well as over current and angle jump. It is also necessary to know how fast the transient processes following a load switching settle to a new steady state value. In this time period, the control of converter is the same as under startup mode. In this simulation a 3.75 MW active and 0.05 MVAR reactive load as house-load was connected at t = 5 s to the station linked to the middle voltage level of 15.75 kV line. The reactive load is almost fully compensated by the line capacitance.

3) *Synchronization of two units equipped with DVC (grid operation)*

At t = 5 s, the synchronization of the BESS (5 MVA) equipped with DVC with the Con 16, (247 MVA) takes place. At t = 20 s the BESS is disconnected from the grid since the main responsibility (BS) has been fulfilled. The output power of the Con 16 unit rises to 3-4% of its nominal power to cover the small load. In next step, after energizing the transformer and transmission line, the first main load will be picked up at a power factor corresponding to 9 MVAR reactive load at t = 26 s. At t = 38 s, converter 15 is connected to the energized grid and try to synchronize with converter 16 (Con 16).

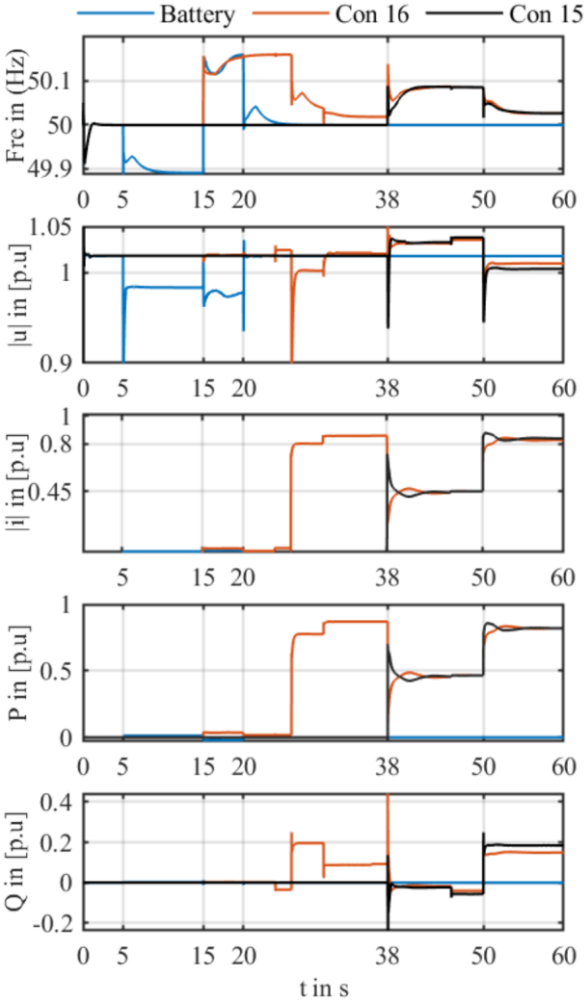

Fig. 13. PCC results for Battery, Con 15 and 16: BS, load pick up, synchronization and load sharing scenarios

4) *Load sharing between present DVC units*

In last section, after synchronization of Con16 and Con15, the presented loads are shared between them equally (because of the similar droop factor). After the connection of the second load corresponding to 200 MW and 40 MVAR load at t = 50 s, again proper equal load sharing is proved. Fig. 13. is shown the converter's quantities in different Stages. Synchronization, load pick up and load sharing with proper identification and optimization can be continued to form the grid completely.

B. *System split, Islanding & Restoration*

System splitting can lead to power system collapse and show the risk, depending on the separation line, of very high active power imbalance in the resulting asynchronous areas. The crucial element for a stable remaining operation is the existence of inherently or fast acting active and reactive power sources in regions with critical voltages and frequencies. The increase of transmission capacities and renewable generation share lead to high locally power imbalance. Moreover, power electronic interfaced generators don't provide inherent contribution to frequency stabilization [20], they can even be subjected to disconnections to limited withstand capability on frequency deviations asked in older grid codes and corresponding conservative protections settings.

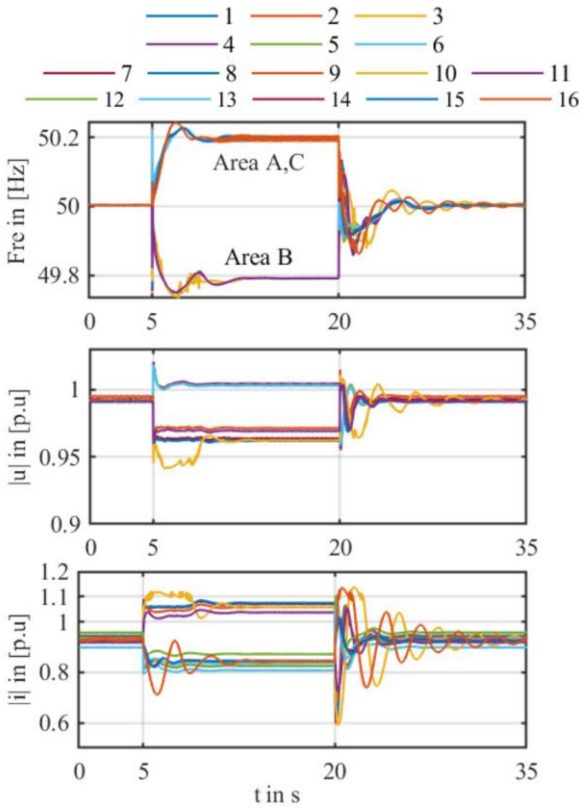

Fig. 14. Behaviour of DVC based converters during system split.
Area A: Con (1, 2, 3, 4, 5, 6) & Area B: Con (7, 8, 9, 10, 11)
Area C: Con (12, 13, 14, 15, 16)

The simulation and analysis of the system split, islanding and resynchronization scenarios with 100% percentage of renewable energy will be shown to show the capability of the GFC DVC to withstand these imbalances. Fig. 14 shows the voltages, frequencies (of their synchronization control) and currents of all 16 converters at their PCC with active RoCoF control loops for Con 10 and 16. The actual system split will take place at the long transmission lines L_{AB} and L_{BC} to isolate grid Area B from Area A and C at t = 5 s. Due to the lack of power provision (about 450 MW active and corresponding reactive power needs), the voltages in the Area B drop as shown in Fig. 14. As a result, the converters in area B partly reach their current limits. Inversely in Area A and C, increase of active power causes over-frequency. Frequency is stabilized by primary control in those areas with the help of the dynamic impact of the RoCoF control loop of converter 16 as shown in Fig. 14. At t = 20 s Area B is reconnected again to Area A and C through transmission line L_{AB} and L_{BC}. The duration of 15 seconds is considered as a new steady state for two separated islanding grids (B & A, C) while at t = 20 s grid is restored and operates in normal steady state condition like before splitting.

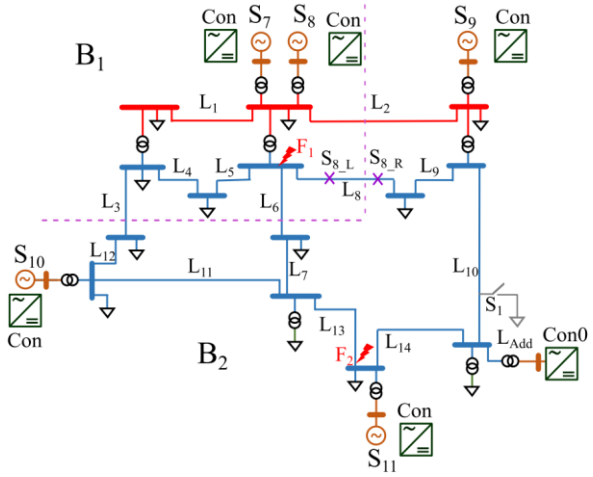

Fig. 15. Area B

C. *Angle jump*

To demonstrate the effects of a phase jump on inverters, resynchronization of a split grid is performed [44, 47, 48]. In this scenario, the combination of Con 9, 10 & 11 with SG 7 & 8 is considered. According to fig. 15, the grid has been split through relevant lines via switches with purple dashed line. It is assumed, that the grid (Area B) is divided into 2 separated zones, zone B2 with 100% converter based generator and zone B1 with 100% SG. These 2 islanded grids are connected together at t = 15.51 s through the tie lines and switches, which causes a large phase jump at the voltage of the converters and transmission lines.

Switching of all lines at the same time is not realistic, however, will cause the highest transients. Fig. 16 illustrates the simulation results obtained for converters' quantities especially their currents which is limited based on fast voltage control method. Moreover, the actual voltage u_a of phase a at line L8 at two ends (S8−L, S8−R) during islanding, resynchronization, and normal modes is shown. Obviously, the phase of u_a at resynchronization has an 180° angle shift, which is considered as the worst case. As a result, stable synchronization is accomplished without violating the current limits of the converters.

D. Primary control and interia

In this section the functionality of the synchronization and RoCoF control loops of the GFC DVC will be examined. The criteria are the RoCoF itself and the NADIR in case of a primary control response of the test systems area B (fig. 15) [44]. For this purpose, the frequency of the test system is investigated and compared to different combinations of GFC DVC and SG after the switch S1 adds 350 MW of additional load. A distinction is made between 5 scenarios in Tab. 2.

Tab. 2. Scenario definition for synchronization on primary control event and provision of inertia

Scenario	Description
1	Only synchronous Generator (SG) in the grid
2	Converter (Con) 9, 10 & 11 RoCoF controller not connected with $H_S = 2.5s$
3	Converter (Con) 9, 10 & 11 RoCoF controller not connected with $H_S = 0.0625s$
4	Converter (Con) 9, 10 & 11 RoCoF controller connected with $H_L = 1.25s$
5	Converter (Con) 9, 10 & 11 RoCoF controller connected with $H_L = 2.5s$

The SGs are equipped with a primary controller with a droop factor of 5%. In order to create the same conditions, the factor kω is set in the converters to $k_\omega = 20$, which corresponds to primary control with a droop factor of 5%. Converter Con 9, 10 and 11 (1550 MVA, 2 x 1000 MVA) are equipped with the GFC DVC in combination with the SGs 7 and 8 (2 x 1300 MVA) are considered for the scenarios 2-5 of tab 2. The results are shown in fig. 17. The frequency measurement is located on Line L_8.

The difference in the steady state frequency between the scenarios with only SGs (1) and the scenarios with converters (2-5) are due to the different load flows from the converter model because of losses w/o adaptions. In scenarios 2-5, where converters Con 9, 10, 11 are replacing SG 9, 10, 11 in the grid, the NADIR is significantly higher, which is due to the instantaneous primary control via the factor k_ω. Since Con 9, 10, 11 make up more than 60% of the generation in the test system in scenarios 2-5, they can make a major contribution to the primary control, but can otherwise also follow the grid frequency via the factor k_{d1}. A comparison between scenarios 1, 2 and 3 shows, that inclusion of inertia in the synchronization swing control loop only has a minor effect on the RoCoF. High damping factors for k_{d1}, required for synchronization at high H_S, counteract an inertia provision over a longer time period. A comparison between Scenarios 2 and 3 shows that placing inertia directly in the synchronizing swing equation results in little improvement in the RoCoF and NADIR of the test system. In the second swing equation for the generation of the RoCof signal (fig. 4), the damping k_{d2} can be selected

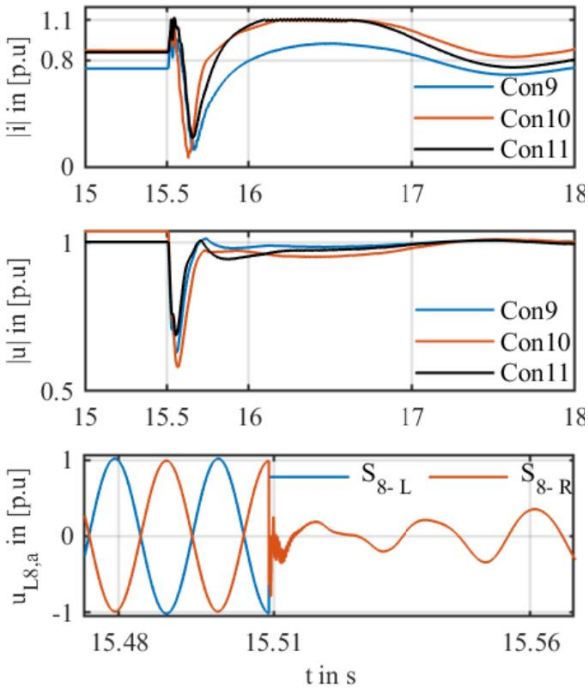

Fig. 16. PCC results of Con (9,10,11) for angle jump scenario

to be very low, so that the inertial response of this does not decay over a long period of time and thus results in more significant improvements of RoCoF and NADIR in scenario 4-5. The second swing equation can be set independently and represents a deterministic possibility of providing inertia, since no noisy frequency gradients have to be measured here.

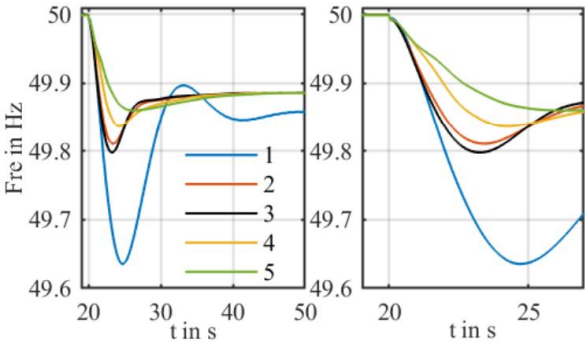

Fig. 17. Frequency response for scenarios in tab. 2 and additional load of 350 MW (primary control response)

E. FRT behavior

The test system is used to evaluate the functionality of the GFC DVC and proposed current limitation based on fast voltage control with different fault scenarios. The dynamic behavior of GFCs in case of interaction with each other and with SG at different electrical distances as well as fault location with different electrical distances to the generating units will be analyzed in 5 scenarios. They include the demonstration of the stability of the system with 100% converter-based generation for small (7.5.3) and large systems (7.5.4). While in the first 3 scenarios, converters with contribution of SGs in electrical grid are considered and in the last scenario (7.5.5) a converter with only 10- MVA rated power is considered to study weak grid

connection. In the last scenario, due to the corresponding small rating of the transformer unit, this converter is connected to the grid with a comparatively high impedance, which reflects a weak grid situation. Robustness of proposed controller will be proved in all scenarios by applying identical controller parameters in spite of different rated power of the converters [44].

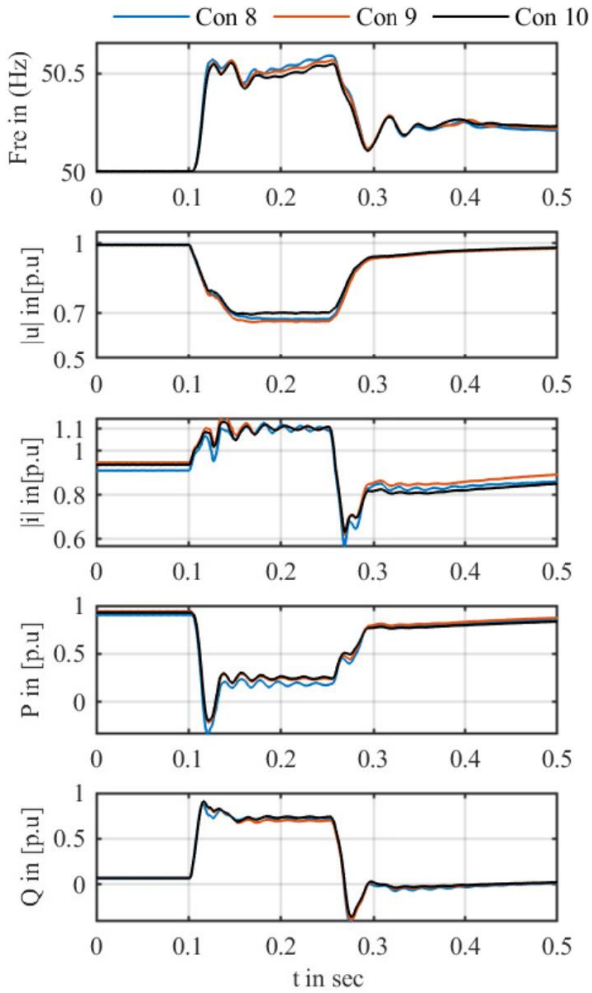

Fig. 18. Scenario 1 FRT fault f1 and output quantities of Con (8,9,10) at PCC

1) *FRT operation current limitation based on fast voltage control in Area B with 60% GFC*

In the first scenario Fig. 18, the operating behavior and current limitation with 60% converter-based generation in Area B is investigated. Three aggregated 1550, 2x1000 MVA Con 9, 10 and 11 controlled by DVC with contribution of 2x1300 MVA SG 7 and 8 in order to illustrate are tested in the event of a symmetrical fault at location F1(fig. 15) with different electrical distance to the generating units to demonstrate that unwanted interactions do not appear with SGs in the grid. The results show stable operation before and after the fault, the balancing processes at fault start and end are well damped for all converters that operate in different electrical distance to the failure location. Moreover, the current limiting intervenes effectively shortly after the fault start and shows no undesirable interactions with each other and SGs.

2) *Comparison of the dynamic behaviour of DVC grid forming with SG*

Fig. 19 presents the results of two different scenarios in order to compare converter dynamic behavior with SGs. This comparison consists of the FRT behavior of Con 9, 10 and 11 based on fast voltage control and the FRT behavior of the SG 9, 10 and 11 for a symmetrical fault at location F1. For this purpose, the test system is parameterized accordingly for these generating units. The output currents of the SG 9, 10 and 11, contains 50 Hz oscillations generated by the DC component of the short-circuit current in d/q-reference frame, which in case of grid forming DVC converters are damped by using SFT-SFT active filtering. According to fig. 19, output quantities of the converter show an overall deeper voltage during fault resulting from strict current limits. The test system is stable in both scenarios, the transient processes quickly decay after fault clearing and the converters keep the current limitation (1.1 pu) already shortly after fault occurrence.

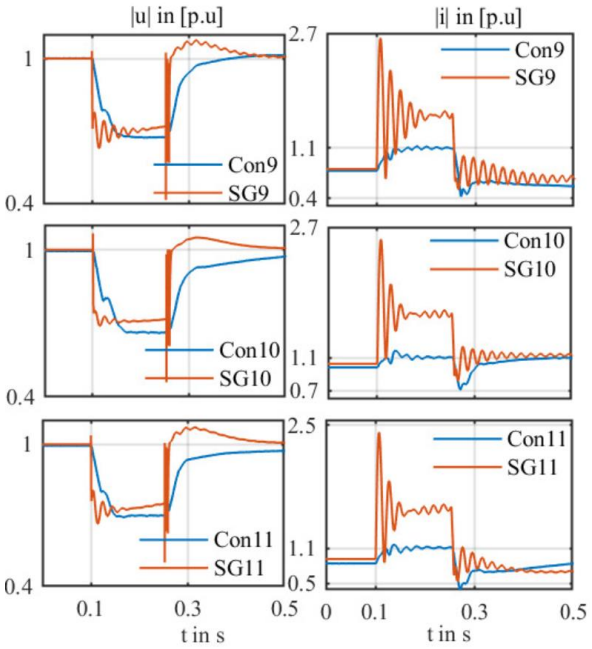

Fig. 19. PCC results for comparison of dynamic behavior between GFC DVC and SG

3) *FRT operation & current limitation based on fast voltage control and through the angle of the grid impedance φ_z with 100% DVC grid forming in a small grid*

Now, the test system is operated purely with GFC for Area B as a small grid to evaluate overall stability during and post fault for a symmetrical fault at location F1 by means of current limitation based on fast voltage control. Fig. 20 shows the functionality of current limitation during fault for all converters (7-11). Additionally, fig. 21 shows the functionality of current limitation as well as overall stability during and post fault for all of converters (7-11) through the angle of the grid impedance φ_z current limitation. The basic idea of the second current limitation is to support the voltage in such an event best possibly. It can be shown, that at least some voltages can be held at higher level by maintaining the same maximum current.

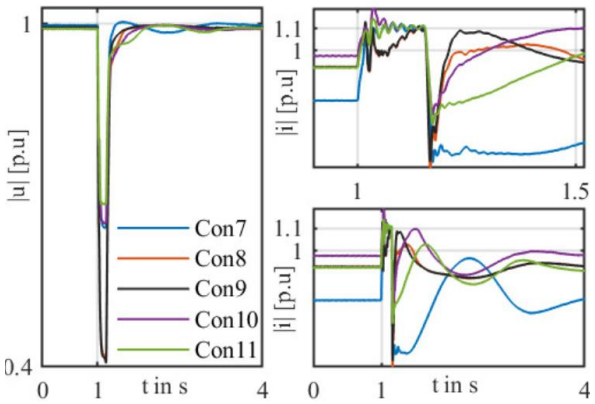

Fig. 20. PCC results for Con (7-11) regarding current limitation (fast voltage based)

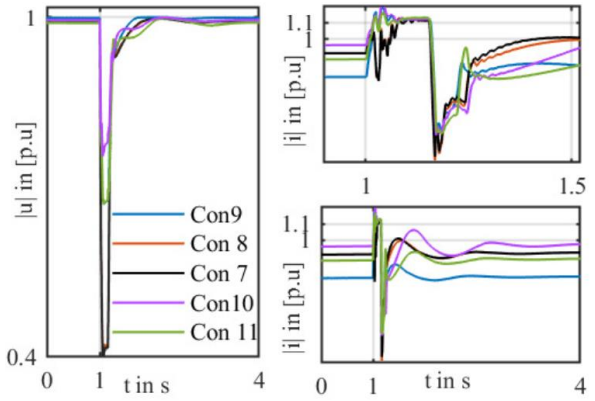

Fig. 21. PCC results for Con (7-11) regarding current limitation (based on angle of the grid impedance φ_z seen by inverter)

4) *100% DVC grid forming in a big grid :*

For the result of fig. 22, the test system is operated purely with GFC for the entire PST16 grid as a large size grid to evaluate overall stability during and post fault conditions. The fault F3 is located centrally in fig. 11, causing a voltage reduction level (more than 20%) at Con 1-7 as well as Con 12-13 terminals, so current in these converters has to be limited. The test system is stable before and after the fault, the transient processes will be damped completely shortly after the fault occurs and after the fault is cleared. Results for both small and big grid don't show any undesirable interactions between converters.

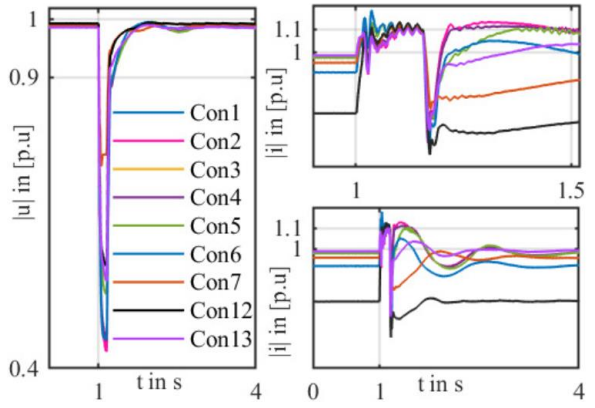

Fig. 22. PCC results for Con (1-16) regarding system stability while GFC DVC applied in entire test system

5) *DVC grid forming in a weak grid*

Finally, the GFC DVC is used for the 10 MVA converter Con 0 in fig. 15 and fault F1 and F2 with at different electrical distances in Area B will be applied. Despite identical parameterization for all converters Con 1-16, the grid-forming DVC shows stable and well-damped behavior (fig. 23). However, the reactive power lashes out more strongly at fault clearing than with the large systems. This is due to the bigger grid impedance of the connection of Con 0, which interacts with the synchronization swing equation and interfere the synchronization process.

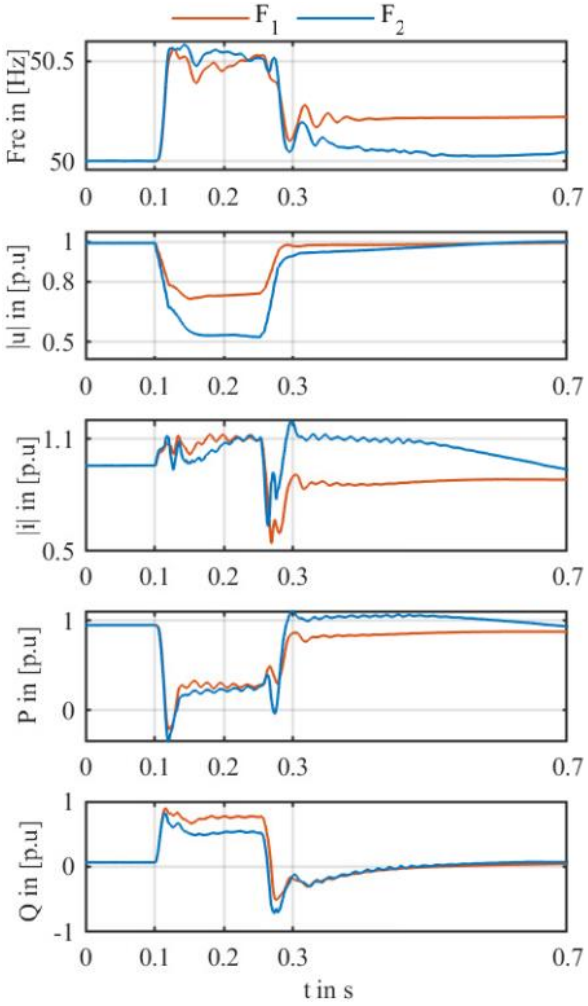

Fig. 23. PCC results of Con 0 regarding weak grid connection under faulty conditions

VIII. Conclusion

This paper presents the concept of a grid-forming DVC in rotating d/q-coordinates which is based on the classical current controlled GFL in terms of structure and operation. Thus, GFC DVC is not a completely new technology with its associated uncertainties. Accuracy and transient performance are derived from the utilization of two-stage sliding Fourier transform filter. DVC is based on the combination of voltage synchronization and power-

balanced synchronization to compensate for each other's disadvantages. The task of synchronizing the converter to the grid and providing virtual inertia is divided into two separate control functions which enable a specific tuning of both functions for their task avoiding the necessity to find any kind of trade-off between the quality of synchronization and inertia provision. Two current limitations, one based on fast voltage control, and another based on the angle of the grid impedance φ_z seen by the converter, have been proposed as FRT control strategies that are simple to implement while still maintaining GFC behavior. The converters in these studies are provided with identical parameters in order to exclude an over-fitting of the parameters for the specific application site and to indicate the robustness of the DVC. Different test scenarios indicate the comprehensive functionality of DVC to address the stability challenges, whereby the converter features frequency and voltage regulation, black start, and load-sharing capabilities. The full-grid-forming DVC concept of this work shows a stable and well-damped dynamic behavior in the main quantities of active and reactive power, output current, and DC magnitudes without significantly exceeding any limitation.

The following work on the grid-forming DVC will address the theoretical analysis for stability and robustness as well as present a grid-forming STATCOM variant of the DVC.

REFERENCES

[1] Fang, J., Li, H., Tang, Y.and Blaabjerg, F., : 'On the Inertia of Future More-Electronics Power Systems', IEEE Journal of Emerging and Selected Topics in Power Electronics., 2019, 7, pp. 2130-2146

[2] Dreidy, M., Mokhlis, H. and Mekhilef, S., : 'Inertia response and frequency control techniques for renewable energy sources: A review'. Renewable and Sustainable Energy Reviews., 2017, 69, pp. 144–155

[3] [3] Qoria, T., Li, C., Oue, K., Gruson, F., Colas, F., Guillaud, X., : 'Direct AC voltage control for grid-forming inverters'. journal of power electronics, 2020, 20, pp. 198-211.

[4] Paolone, M., Gaunt, T., Guillaud, X. and et al, : 'Fundamentals of Power Systems Modelling in the Presence of Converter-Interfaced Generation', Electric Power Systems Research., 2020, 189, pp. 180-197

[5] F. Milano, F. Dörfler, G. Hug, D. J. Hill, and G. Verbi´ c., : 'Foundations and challenges of low-inertia systems,' in Proc. Power Syst. Comput.Conf. (PSCC), Dublin, Ireland, Jun. 2018, pp. 1–25

[6] Pan, D., Wang, X., Liu, F., and Shi, R., : 'Transient Stability of Voltage-Source Converters With Grid-Forming Control:A DesignOriented Study'. IEEE journal of emerging and selected topics in power electronics, 2020,(8), 2, pp. 1019-1033

[7] Chen, M., Zhou, D., and Blaabjerg, F., : 'Modelling, Implementation, and Assessment of Virtual Synchronous Generator in Power Systems'.JOURNAL OF MODERN POWER SYSTEMS AND CLEAN ENERGY, 2020, (8), 3, pp. 39-411

[8] Hesse, R., Turschner, D., and Beck, H.-P., : 'Micro grid stabilization using the virtual synchronous machine (VISMA)," Renewable Energy and Power Quality Journal,2009 (1), 7, pp. 676-681

[9] [9] Chen, Y., Hesse, R., Turschner, D. and Beck, H.-P., : 'Dynamic properties of the virtual synchronous machine (VISMA),' Renewable Energy and Power Quality Journal, 2011, (1), 9, pp. 755-759

[10] Chen, Y., Hesse, R., Turschner, D. and Beck, H.-P., : 'Comparison of methods for implementing virtual synchronous machine on inverters' Renewable Energy and Power Quality' Journal, 2012, (1), 10, pp. 734-739

[11] Zhang, W., Remon, D. and Rodriguez, P. : 'Frequency support characteristics of grid-interactive power converters based on the synchronous power controller,' IET Renewable Power Generation,2017, (11), 4, pp. 470-479

[12] Peng, Z., Wang, J., Bi, D. and et al., : 'The application of microg rids based on droop control with coupling compensation and inertia,' IEEE Transactions on Sustainable Energy,2018, (9), 3, pp. 1157-1168

[13] [Zhang, C.-H., Zhong, Q.-C. and Meng, J.-S. and et al., 'An improved synchronverter model and its dynamic behaviour comparison with synchronous generator,' in Proceedings of 2nd IET Renewable Power Generation Conference (RPG 2013), Beijing, China, Sept. 2013, pp.1-4.

[14] D'Arco, S., Suul, J. A. and Fosso, O. B. : 'A virtual synchronous machine implementation for distributed control of power converters in smartgrids,' Electric Power Systems Research, 2015, 122, pp. 180-197

[15] Zhong, Q.-C., Weiss,G., : 'Synchronverters: Inverters That Mimic Synchronous Generators,' IEEE Transactions on Industrial Electronics, 2011, (58), 4, pp. 1259-1267 IET Research Journals, pp. 1–15 14 © The Institution of Engineering and Technology 2015

[16] Shintai, T., Miura, Y., Ise, T., : ' Reactive Power Control for Load Sharing with Virtual Synchronous Generator Control,' in Proceedings of the 2012 IEEE 7th International Power Electronics and Motion Control Conference – ECCE Asia, Harbin, China, 2-5 June 2012, pp. 846-853

[17] Denis, G., Prevost, T., Debry, M.-S., Xavier, F., Guillaud, X. and Menze, A., : 'The Migrate project: The challenges of operating a transmission grid with only inverter-based generation. A grid-forming control improvement with transient current-limiting control,' IET Renew. Power Gener., 2018, (12), 5, pp. 523–529

[18] Sadeghkhani, I., Golshan, M. E. H., Guerrero, J. M. and Mehrizi-Sani, A., : 'A current limiting strategy to improve fault ridethrough of inverter interfaced autonomous micro-grids,' IEEE Trans. Smart Grid, 2017, (8), 5, pp. 2138–2148

[19] A. D. Paquette and D. M. Divan, 'Virtual impedance current limiting for inverters in microgrids with synchronous generators,' IEEE Trans. Ind. Appl., 2015, (51), 2, pp. 1630–1638.

[20] Qoria,T., Gruson, F., Colas, F., Denis, G., Prevost, T., and Guillaud, X., : 'Critical Clearing Time Determination and Enhancement of Grid-Forming Converters Embedding Virtual Impedance as Current Limitation Algorithm,' IEEE Journal of Emerging and Selected Topics in Power Electronics, 2020, (8), 2

[21] Rocabert, J., Luna,A., Blaabjerg, F., Rodríguez, P., : 'Control of Power Converters in AC Microgrids," IEEE Transactions on Power Electronics, 2012, (27), 11, pp. 4734-4749

[22] D'Arco, S., Suul, J. A. and Fosso, O. B., : 'Control System Tuning and Stability Analysis of Virtual Synchronous Machines,'IEEE Energy Conversion Congress and Exposition, September 2013, Denver, USA

[23] Neumann, T.,Erlich, I., Paz, B. and et al. : 'Novel direct voltage control by wind turbines,' IEEE Power and Energy Society General Meeting (PESGM), 2016, pp. 1-5

[24] Erlich, I., Korai, A. and Neumann, T. : 'New Control of Wind Turbines Ensuring Stable and Secure Operation Following Islanding of Wind Farms', IEEE Transactions on Energy Conversion, 2017, (32), 3, pp. 1263-1271

[25] Korai, A., Denecke, J., Rueda Torres, J. L. and Rakhshani, E. : 'New control approach for blackstart capability of full converter wind turbines with direct voltage control', IEEE Milan PowerTech, June 2019, pp. 1-6

[26] Tayyebi, A., Dörfler, F., Kupzog, F., Miletic, Z. and Hribernik, W. : 'Grid forming converters-inevitability, control strategies and challenged in future grids application', in Proc CIRED Ljubljana Workshop on Microgrids and Local Energy Communities., 2018, pp. 1-6

[27] Tayyebi, A., Anta, A.and Dörfler, F. : 'Grid-Forming Hybrid Angle Control and Almost Global Stability of the DC-AC Power Converter',IEEE Transactions on Automatic Control, 2022, pp. 1-16

[28] Taul, M. G., Wang, X., Davari, P. and Blaabjerg, F., : 'An overview of assessment methods for synchronization stability of grid-connected converters under severe symmetrical grid faults,' IEEE Trans. Power Electron., 2019, (34), 10, pp. 9655–9670

[30] Wang, X.,Graungarrd Taul, M. and et al, : 'Grid-Synchronization Stability of Converter-Based Resources—An Overview', IEEE Open Journal of Industry Applications, 2020, (1),pp. 115-134

[31] Chen, J., Prystupczuk, F. and O'Donnell, T., : 'Use of voltage limits for current limitations in grid-forming converters,' in CSEE Journal of Power and Energy Systems, vol. 6, no. 2, pp. 259-269, June 2020,

[32] Paquette, A. D. and Divan, D. M., : 'Virtual Impedance Current Limiting for Inverters in Microgrids With Synchronous Generators,' in IEEE Transactions on Industry Applications, vol. 51, no. 2, pp. 1630-1638, March-April 2015

[33] Welck, F., Duckwitz, D. and Gloeckler, C.. : 'Influence of Virtual Impedance on Short Circuit Performance of Virtual Synchronous Machines in the 9-Bus System,' NEIS 2017; Conference on Sustainable Energy Supply and Energy Storage Systems, 2017, pp. 1-7.

[34] Zhang, L., Harnefors, L. and Nee, H., : 'Power-Synchronization Control of Grid-Connected Voltage-Source Converters,' in IEEE Transactions on Power Systems, vol. 25, no. 2, pp. 809-820, May 2010, doi: 10.1109/TPWRS.2009.2032231.

[35] Huang, L., Xin, H., Wang, Z., Zhang, L., Wu, K. and Hu, J., : 'Transient Stability Analysis and Control Design of DroopControlled Voltage Source Converters Considering Current Limitation,' in IEEE Transactions on Smart Grid, vol. 10, no. 1, pp. 578-591, Jan. 2019

[36] Shi, K., Song, W., Xu, P., Liu, R., Fang. Z. and Ji, Y., : 'LowVoltage Ride-Through Control Strategy for a Virtual Synchronous Generator Based on Smooth Switching," in IEEE Access, vol. 6, pp. 2703-2711, 2018

[37] Shuai, Z., Huang, W., Shen, C., Ge. J. and Shen, Z. J., : 'Characteristics and Restraining Method of Fast Transient Inrush Fault Currents in Synchronverters,' in IEEE Transactions on Industrial Electronics, 2017,(64), 9, pp. 7487-7497

[38] Schöll, C. and Lens, H., : 'Impact of Current Limitation of Grid-forming Voltage Source Converters on Power System Stability,' 2020 IFAC-PapersOnLine, 2020, (53), 2, pp. 13520-13524

[39] Taul, M. G., Wang, X., Davari, P. and Blaabjerg, F., : 'Current Limiting Control With Enhanced Dynamics of Grid-Forming Converters During Fault Conditions,' in IEEE Journal of Emerging and Selected Topics in Power Electronics, 2020, (8), 2, pp. 1062-1073

[40] Arafa, O. M. : 'Two Stages Sliding Fourier Transform for High Performance Phase Angle and Frequency Tracking', Journal of Electrical Engineering Technology., 2020, 15, pp. 2007-2016

[41] Milano, F., Dorfler, F., Hug, G., Hill, D. and Verbic, G., : 'Foundations and challenges of low-inertia

[42] Ortega, A.and Milano, F., : 'Converter-Interfaced Energy Storage Systems Converter-Interfaced Energy Storage Systems', In Procs. of the Power Systems Computation Conference (PSCC), 2019, pp. 240-245

[43] systems', In Procs. of the Power Systems Computation Conference (PSCC), 2018, pp. 1–22 Paolone, M., Gaunt, T., Guillaud, X., Liserre, M., Meliopoulos, S., Monti, A., Van Cutsem, T., Vittal, V., Vournas, C., : 'Fundamentals of Power Systems Modelling in the Presence of Converter-Interfaced Generation. Proc 2020 Power System Computation Conference (PSCC)

[44] Maherani, M., Denecke, J. and Vennegeerts, H., : 'Flexible parameterizable grid-forming converter control by separated fast synchronization and slow inertia response control loops of Direct Voltage Control'. IFAC-CPES 2022, 11th Symposium on Control of Power and Energy Systems, Moscow, Russia, pp. 1-6

[45] Denecke, J., Maherani, M. and Vennegeerts, H., : 'Current Limitation in fully grid-forming Direct Voltage Control'. in Proc 20th wind integration workshop, Sep. 2021, pp. 1–8

[46] Maherani, M., Denecke, J. and Vennegeerts, H., : 'Current Limitation based on fast voltage control for fully grid-forming Direct Voltage Control'. IEEE ENERGYCON-2022, May 2022, pp. 1-6

[47] Maherani, M. and Vennegeerts, H., : 'Complementary Current Limitation Control for Grid-Forming Direct Voltage Control ', Smart Energy Grid Engineering (SEGE), 2022, August, pp. 1-6

[48] Maherani, M. and Vennegeerts, H., : 'Current Limitation Control through the Angle of Grid Impedance for Grid-Forming Direct Voltage Control ', IEEE PES ISGT Europe, 2022, October, pp. 1-5

[49] Erlich, I., Shewarega, F. and Winter, W., : 'A method for incorporating VSC-HVDC into the overall grid voltage-reactive power control task',in Proc Power Systems Computation Conference (PSCC), June 2016, pp. 1-7

[50] Teeuwsen, S.P., Erlich, I.and El-Sharkawi, M.A., : 'Neural network based classification method for small-signal stability assessment', in Proc PowerTech, June 2003

[51] Jain, A., Sakamuri, J.N. and Cutululis, N.A., : 'Grid-forming control strategies for blackstart by offshore wind farms,' Wind Energ. Sci., 2020, 5, pp. 1297–1313,

[52] Ippolito, M., Musca, R. and Zizzo, G.:'Current Limitation in fully Frequency Dynamics of European System during split Integration Grid Forming Capabilities', in Proc 20th wind integration workshop, Sep. 2021, pp. 1-6

Methodology for Projection of the Diffusion of Electric Vehicles in Residential Consumers

Mauro dos Santos Ortiz
Otto-von-Guericke University
Institute of Electric Power Systems
Magdeburg, Germany
mauro.dossantosortiz@ovgu.de

Pedro Henrique Eisenkraemer
Federal University of Santa Maria
Center of Excellence in Energy and Power Systems
Santa Maria, Brazil
pedrokrameci@gmail.com

Daniel Pinheiro Bernardon
Federal University of Santa Maria
Center of Excellence in Energy and Power Systems
Santa Maria, Brazil
dpbernardon@ufsm.br

Martin Wolter
Otto-von-Guericke University
Institute of Electric Power Systems
Magdeburg, Germany
martin.wolter@ovgu.de

***Abstract*—This paper presents a methodology for forecasting the diffusion of Electric Vehicles (EVs) among residential consumers, combining the System Dynamics (SDs) technique and the Bass diffusion model. The proposed model was tested in a case study in Santa Maria, Brazil, taking into account economic, technical, socio-environmental, political and market factors. Preliminary results suggest a potential saturation of EV adoption by 2040 in an optimistic scenario, emphasizing the adaptability of the model to varying weights and scenarios. The study highlights the effectiveness of adapting the SDs and the Bass model to study dynamic system behavior. The model's versatility allows for future extensions, encouraging ongoing refinement for policymakers, power system operators, and other stakeholders interested in analyzing the challenges and opportunities of sustainable EV adoption.**

Keywords—Bass diffusion model, diffusion of innovations, electric vehicles, system dynamics

I. INTRODUCTION

The existing literature on the diffusion of new products and advances in both technological and social domains is extensive [1]–[7]. One seminal publication in the field of study is the book "Diffusion of Innovations," authored by Everett Rogers and initially released in 1962. Adopting novel products or services is a gradual occurrence that does not manifest instantaneously across all individuals within a given social system. According to Rogers [4], those who embrace innovation at an early stage exhibit distinct qualities compared to those who adopt it later.

Although widely researched, the study of innovation diffusion processes remains a complex task [2], [8]. In the context of electric vehicles (EVs), analyzing whether or not new vehicles will be adopted is even more difficult given the large number of possible variables and the uncertainties associated with potential consumers' decisions.

In this sense, this paper aims to present a methodology for estimating the projected diffusion of EVs among residential consumers. To this end, a review of the theoretical basis of the System Dynamics (SDs) technique is carried out, together with the Bass model, which is used to develop the proposed model. Five groups are considered: economic, technical, socioenvironmental, political and market, in order to determine consumer adherence to EVs over time. The model is tested through a case study and the preliminary results of which are considered satisfactory. The versatility of the methodology presented stands out, with the possibility of extending it by including new variables and aspects. This feature is crucial to understanding how the increased penetration of EVs can impact the electricity system, as well as the barriers and potential related to the development of public policies, charging infrastructure and new business models for sustainable and efficient electrification in the transportation sector.

This work was supported by CNPq MAI/DAI, CAPES/PROEX - Finance Code 001 and CAPES/PrInt. The authors gratefully acknowledge UFSM (Brazil) and OVGU (Germany) for also supporting the development of research.

II. SYSTEM DYNAMICS TECHNIQUE

The SDs technique emerged in 1961 with Jay W. Forrester, who sought to understand strategic problems in complex dynamic systems [5], [6]. It is based on theories of control and non-linearity and has been used for several decades to understand and estimate the processes of adoption and diffusion of new products [3]. These studies are essential for governments and companies that organize market development by formulating policies and investments in new technologies and infrastructure [3], [8].

SD is a method that uses inventory, flow, internal feedback loops, table functions, and time delays to understand the non-linear behavior of complex systems over time [9]. Saavedra, Fontes, and Freires [10] reviewed various works in the renewable energy supply sector that used SDs in their modeling. Similarly, Selvakkumaran and Ahlgren [11] reviewed articles from the last decade, systematically categorizing the different approaches and uses of the SD technique to examine the complex processes of local energy transitions.

Recently, Domarchi and Cherchi [2] published a review article, providing a critical review of the methods found in the literature for predicting the diffusion of innovation in the transportation sector, in which there is also a long list of works that have used SDs and the Bass model. These authors did not set out to determine which method is best for obtaining robust forecasts in all circumstances but rather to analyze the strengths and weaknesses of each modeling proposal, identifying the elements that can contribute to a more accurate representation of EV demand estimation.

In the diverse range of publications cited in the literature, the SD technique is presented as a tool to analyze the behavior of systems, defined as a set of functional elements and the relationships that include them, susceptible to variations over time [3], [8], [9], [12]. Some advantages of using SDs are [12]:

- Possibility of dealing with long- and short-term aspects in the same model;
- Complete representation of complex and non-linear relationships;
- Possibility of representing social and psychological variables;
- Ease with which the effects of political alternatives can be tested.

The models developed using SD make it possible to represent physical flows, which can be accumulated, and information flows, which are typically observed but cannot be accumulated, as feedback mechanisms between the parties. As such, changes in external variables can cause alterations in the system's state [12]. These changes can be distortions, delays, system responses, flows, accumulation of flows (stocks), and feedback, which end up resulting in a dynamic model thought of in a systemic way [6], [8], [12].

The main characteristic of the SDs technique is the feedback of information [5], [6], [12]. Feedback loops form causal loop diagrams (CLDs) and demonstrate the phenomenon where X influences Y and Y, in turn, affects X, potentially through a series of interconnected causes and effects. To make this explanation more palatable, Fig. 1 presents a modest illustration of the impact of the CLD.

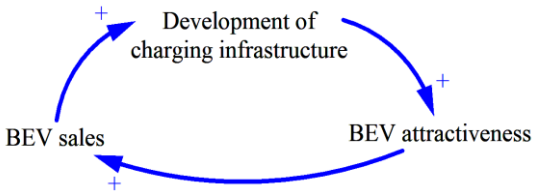

Fig. 1. CLD among BEV sales, BEV attractiveness, and the development of charging infrastructure.

Fig. 1 shows that the increase in BEV sales positively impacts the development of charging infrastructure. Technological advances, environmental concerns, and government incentives have increased BEV sales. This increase in sales, in turn, amplifies the need for a robust and affordable charging infrastructure. In addition, the proper development of charging stations is essential to mitigate range anxiety, allowing EV users to charge their vehicles conveniently and efficiently, increasing BEVs' attractiveness. In this case, it is observed that positive feedback is represented by an arrow with a "plus" sign.

On the contrary, negative feedback operates inversely within the system. For example, the purchase cost of BEVs will decrease in inverse proportion to the increase in their production volume. The decrease in cost stimulates sales, which in turn increases the production rate. This indicates that the quantity of BEVs produced remains reversely proportional to their cost. Negative feedback is denoted by an arrow with a "minus" sign in the model.

Since real systems are made up of several feedback loops and, consequently, several variables, the complexity of system analysis increases as the number of variables and the non-linear and dynamic relationships between them increase, as well as depending on the ways in which the system interacts with the environment [5], [6]. In this context, Ford [6] suggests eight steps for modeling a system using the SD technique in his book "Modeling the Environment":

- Step 1. A ("Acquainted"): familiarize yourself with the system to be modeled;
- Step 2. B ("Be specific"): be specific about the dynamic behavior of the problem;
- Step 3. C ("Construct"): build the stock and flow diagrams;
- Step 4. D ("Draw"): draw the causal loop diagram;
- Step 5. E ("Estimate"): estimate the parameter values;
- Step 6. R ("Run"): simulate the model to obtain the reference mode;
- Step 7. S ("Sensitivity"): perform sensitivity analysis;
- Step 8. T ("Test"): test the impact of the policies under analysis.

Another vital author about SDs, John D. Sterman, in his book "Business dynamics" [5], suggests five steps for modeling a problem using SD. Fig. 2 shows these proposed steps.

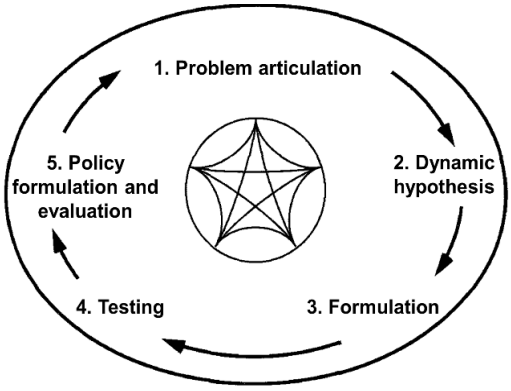

Fig. 2. Modeling steps proposed by Sterman [5].

Sterman [5] considers the articulation of the problem, which includes selecting the topic, defining the key variables, the dynamic problem, and the time horizon, to be the most important step in modeling. Next, a dynamic hypothesis must be formulated, which is the theory that allows the dynamics represented by the model to be understood. At this stage, subsystems, feedback schemes, causal loop diagrams, stock and flow diagrams are systematically schematized. The third step is to formulate the simulation model. This involves specifying the decision parameters, initial conditions, equations, and behavioral relationships. At this stage, the designer must pay attention to possible modeling contradictions not observed in the conceptual formulation in order to resolve them. In the

testing phase, the simulated behavior is compared with the real behavior of the system. In addition, the proposed modeling is thoroughly tested by means of sensitivity analyses to see if there are any shortcomings. Finally, after analyzing the behavior of the system, new environmental conditions can be studied, which, if they occur, would modify the system. Similarly, new policies and scenarios can be formulated to verify the system's behavior.

As evident from the comparison, the SD modeling approach outlined by Ford (1999) [6] and Sterman's method (2000) [5] exhibit substantial similarities. Distinctions in their procedural sequences arise primarily from variations in the level of detail incorporated into the modeling process. Consequently, in this this study, Sterman's modeling steps were adopted due to their objectivity and efficiency in implementing the stages of modeling EV diffusion as an innovation.

As previously mentioned, the process of system dynamics modeling involves the creation of CLDs, in which the system variables and their interrelationships are schematized in the form of feedback loops. In addition to this diagram, it is important to understand stock and flow diagrams (SFDs). Stocks are nothing more than accumulations that represent the state of the system and provide information on which the model's actions and decisions are based.

Finally, it is important to mention that CLDs serve as qualitative representations of the cause-and-effect connections among the system variables. In order to quantify the variables under consideration, SFDs are implemented. The distinction between CLDs and SFDs is that logical formulas and/or mathematical equations are used to relate the variables in the latter.

III. BASS DIFFUSION MODEL

After analyzing the theory of diffusion of innovations proposed by Rogers in 1962, Frank Bass modeled it mathematically in 1969 [13]. The significant contribution of the model developed by Bass is the possibility of generating a sigmoid curve for analyzing the penetration rate of a diffusion over time [4].

Sterman [5] points out that one of the problems with logistic models of the diffusion of innovations concerns initialization, because in logistics, as well as in other simple growth models, including Richards and Weibull, zero represents equilibrium. Consequently, the origin of the initial adopters of a new technology cannot be explained by these models. In this sense, the diffusion of innovations model proposed by Bass overcomes the initialization problem, based on the assumption that potential adopters become aware of the innovation through external sources of information of continuous magnitude and persuasion over time.

The Bass model envisages the market as potential consumers mixed homogeneously with each other and interacting mutually over time. In this way, the dynamics between the groups occurs in the sense that an individual who did not adopt the new technology starts to adopt it, based on two rates: the coefficient of innovation (p), formed by the "innovators", and the coefficient of imitation (q), which corresponds to the group of "imitators" [13]. Innovators are motivated by external influence, such as the media, while imitators are influenced by the internal patterns of their social system, which is qualified as "word of mouth" contact [1], [5], [13]. From a mathematical point of view, Bass's model is expressed by (1) [13].

$$P(t) = p + q \cdot \frac{Y(t)}{m} \tag{1}$$

Where: $P(t)$ represents the probability of adoption of the innovation at time t; p is the innovation coefficient; q is the imitation coefficient; $Y(t)$ expresses the cumulative total number of consumers who have already adopted the new technology at time t, and m is the potential market or final number of total adopters.

Upon analyzing (1), it can be seen that its growth is contingent upon the increase in the number of consumers who accept the market innovation, denoted as $Y(t)/m$. Furthermore, this growth is directly proportional to the coefficient q.

Since $Y(t)$ represents the accumulated total of adopters at time t, $dY(t)/dt$ will be the rate at which new consumers are added at each moment in time. Therefore, the likelihood of purchase at time t can be expressed as the proportion of individuals who adopt the product at time t, in relation to those who have not yet adopted it on the market, given by (2).

$$P(t) = \left(\frac{1}{m - Y(t)}\right) \cdot \frac{d}{dt} Y(t) \tag{2}$$

By combining (1) with (2) and assuming $U(t) = (m - Y(t))$ as the quantity of potential consumers remaining to purchase the product, the Bass model is derived in its differential form as seen in (3).

$$\frac{d}{dt} Y(t) = p \cdot U(t) + q \cdot U(t) \cdot \frac{Y(t)}{m} \tag{3}$$

The solution to (3) depicts an S-shaped curve, wherein the asymptote of the resulting graph corresponds to the maximum market capacity—represented by the parameter m, denoting the market potential.

Further, the substitution of $Y(t)/m$ for $F(t)$, yields the most widely recognized representation of the Bass model, which is a first-order differential equation (4).

$$\frac{d}{dt} F(t) = f(t) = \big(p + q \cdot F(t)\big) \cdot \big(1 - F(t)\big) \tag{4}$$

$$= p + (q - p) \cdot F(t) - q \cdot F^2(t) \tag{5}$$

In this depiction, $f(t)$ signifies the sales function density at time t, while $F(t)$ denotes the cumulative fraction of the potential reached by that time. Integrating $f(t)$ over time results in the cumulative fraction, as expressed in (5).

$$F(t) = \frac{1 - e^{-(p+q)t}}{1 + (p/q)e^{-(p+q)t}} \tag{5}$$

From the analysis of the Bass model equations, it can be seen that if essential information about the market is not accessible to the designer or if it is not found, it is extremely difficult to parameterize the model for the innovation to be analyzed. For this reason, to expand and improve this model,

other techniques can be incorporated into it, such as the discrete choice model and system dynamics [8].

As previously stated, using of the SD technique enables the simulation and comprehension of the temporal behavior of complex systems through the examination of the system's structure and its feedback mechanisms [5], [12]. By adopting this approach, it becomes feasible to examine the system by considering the interplay between its behavior and its structure, which comprises interconnected decision-making processes and temporal lags.

In this sense, SD presents itself as an interesting tool to combine the proposal of the Bass model, including the projection of the diffusion of an innovation over time and its social aspects, with the fundamentals of discrete choice models, in which it is possible to model and characterize consumer preferences according to other diverse variables and characteristics attributed to the new technology, to the market of a given region, as well as to its potential adopters. For an examination of the Bass model from a SD perspective, consult Sterman (2000) [5].

IV. PROPOSED METHODOLOGY

Fig. 3 presents an overview of the proposed methodology for estimating the adoption of EVs among residential consumers. As illustrated in this figure, the initial step involves analyzing barriers to EV diffusion, encompassing economic, technical, political, social, environmental, and market-related aspects. Mapping these barriers contributes to forming essential knowledge and understanding of the system, which is fundamental for proper modeling. The subsequent stage focuses on investigating the diffusion of EVs over time, using the system dynamics (SD) technique in conjunction with the Bass model, with a suggested division into five distinct groups: economic, technical, political, socio-environmental, and market. Table I presents the major barriers linked to the diffusion of EVs among residential consumers.

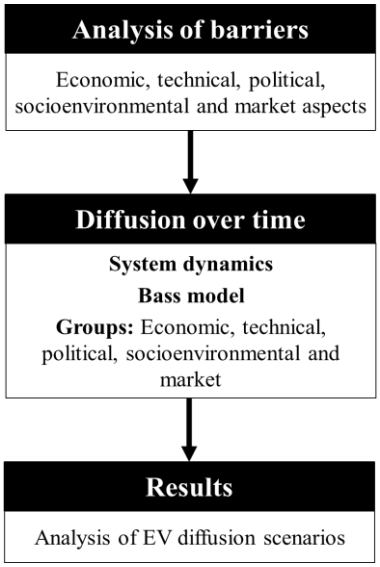

Fig. 3. Overview of the proposed methodology for estimating EV diffusion.

TABLE I. MAJOR BARRIERS TO EV ADOPTION

Economic group	Technical groups	Socioenvironmental group	Political group	Market group
EV acquisition cost	Development of batteries	Carbon credits	Political scenario	Marketing
Recharge cost	Recharge time	Ecological conscience	Economic scenario	Business incentives
Financing for the acquisition of EV	EV efficiency	Pollution reduction	Public policies	Business models
Consumer income	EV range (autonomy)	Satisfied customers	Subsidies	EV sales
Payback	Recharge infrastructure	EV knowledge advertisements	Tax incentives	Sales decay rate
V2G	Durability	HDI	Environmental issues	
EV maintenance		Education (Schooling)		

The barriers identified through a concise literature review [2], [8], [14]–[17] hold significance for parameterizing each group within the model. Within the economic domain, factors such as the initial cost of acquiring EVs, the availability of financing options, and the expenses associated with recharging consistently emerge as pivotal considerations. In this context, the implementation of differentiated tariff structures has the potential to stimulate the adoption of vehicle-to-grid (V2G) technology. This, in turn, could lead to an expansion of the EV fleet and their participation in the energy supply to the power grid. Technical barriers persistently hinge on advancements in battery technology, charging durations, and the driving range of EVs. Additionally, a primary apprehension among prospective EV consumers pertains to the accessibility of charging infrastructure within their residential regions.

In socioenvironmental context, it is noted that developed countries, characterized by high human development indices (HDI) and robust levels of education, stand out for their notable concern for environmental issues and a more pronounced ecological footprint. This environmental awareness strengthens the propagation of EVs as an effective response to reducing greenhouse gas emissions. In the market context, the dynamics involve considerations about available alternatives, dealership strategies, and innovations that drive the adoption of EVs. Factors such as sales, the development of new business models, and the introduction of products to the market become central in this context. Additionally, each region's political and socio-economic scenarios play a crucial role in the political group, directly influencing the adoption of EVs. Therefore, it is imperative to analyze specific public policies, subsidies, and incentive rates in each locality to understand the market dynamics in that region.

The proposed SD model is presented in Fig. 4. In this diagram, the model developed resembles the basic structure of

the Bass model when considering its coefficients and the potential EV market. Furthermore, using SDs, the classic Bass model is extended to consider the effect of other variables that influence the user's decision at the time of purchase.

Beyond the traditional categorization of consumers as "imitators" or "innovators" and the potential market (m), derived from the Bass model (1969), this study proposes the inclusion of five additional groups to deepen the analysis of EV diffusion. These groups include the economic, technical, socio-environmental, political, and market dimensions. Mathematically, these groups manifest as weights in the model, allowing for the assessment of the relative influences of these factors on the consumer's decision to acquire or not an EV. These considerations provide relevant insights and flexibility to explore various scenarios, enabling the conduct of more in-depth and comprehensive analyses.

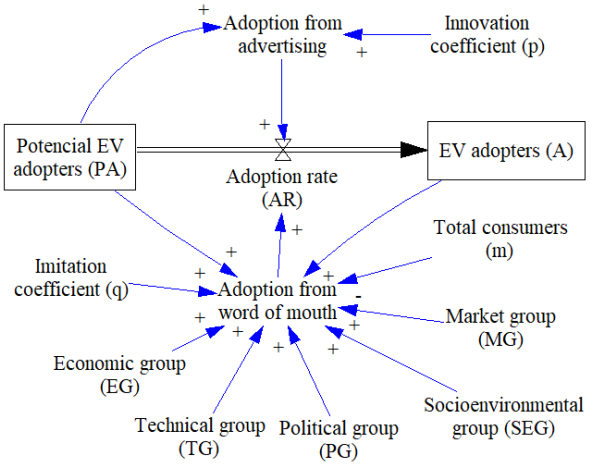

Fig. 4. Proposed model.

Analysis of the CLDs in Fig. 4 allows for establishing mathematical correlations among the stock and flow variables in the SKD. The adoption from word of mouth ($A_{WM}(t)$) and the adoption from advertising ($A_{Ad}(t)$) over time are modeled according to (6) and (7), respectively.

$$A_{WM}(t) = EG \cdot TG \cdot SEG \cdot PG \cdot MG \cdot q \cdot PA(t) \cdot \frac{A(t)}{m} \quad (6)$$

$$A_{Ad}(t) = p \cdot PA(t) \quad (7)$$

Where: EG, TG, SEG, PG, and MG correspond respectively to the economic, technical, socio-environmental, political, and market groups; q is the imitation coefficient; p is the innovation coefficient; $PA(t)$ represents the potential EV adopters; $A(t)$ are the consumers who have already purchased the EV; and m represents the total consumers (market potential). The adoption rate ($AR(t)$) is expressed by (8).

$$AR(t) = A_{Ad}(t) + A_{WM}(t) \quad (8)$$

Finally, the adopters of EVs and potential adopters are determined by (9) and (10), respectively.

$$A(t) = \int_{t_0}^{t} AR(t)dt + A(t_0) \quad (9)$$

$$PA(t) = -\int_{t_0}^{t} AR(t)dt + \left(m - A(t_0)\right) \quad (10)$$

Where: t_0 is the initial time and $A(t_0)$ denotes the part of consumers who currently already own the EV. In the context of innovation diffusion studies, it is conventionally observed that this value tends to be notably low in the beginning of the investigations.

V. Results

The present section is dedicated to testing the proposed model for EV diffusion. The analyses are conducted through a case study implemented using Vensim® Professional software version 7.0.

It is important to note that, given the focus of this study on reviewing the Bass model and SDs technique and expanding the Bass model by employing SD to analyze EV diffusion, a specific methodology for estimating the weights of each group outlined in this article has not been detailed. Consequently, for the conducted simulations, two distinct scenarios were considered: an optimistic scenario, with weights set at 0.85 for all groups, and a pessimistic scenario, with weights set at 0.20 for all groups.

The research was carried out utilizing data obtained from the municipality of Santa Maria, situated in the southern region of Brazil. The simulated data encompassed a 30-year span, specifically from 2021 to 2051.

As per the data provided by the Brazilian Institute of Geography and Statistics ("Instituto Brasileiro de Geografia e Estatística", IBGE), the population of Santa Maria is recorded as 271,735 individuals. Based on data from the aforementioned institute, the number of individuals classified as economically active in 2021 amounted to 81,184 workers. To ascertain the total number of customers (m), the adopted approach involved utilizing the figure for the economically active population, which accounts for around 30% of the whole population [18].

Furthermore, as reported by the organization "Parceria Solar", Santa Maria possessed a total of 6 EVs in the year 2021, signifying the initial value ($A(t_0)$) of the suggested model [19]. Therefore, the population of potential adopters of the model amounts to 81,178 consumers.

The p and q coefficients of the Bass model employed in this study were set at 0.0912 and 0.4692, respectively. These values were derived from [7], which conducted a comprehensive empirical analysis for the selection of the Bass model coefficients, aiming to predict the diffusion of innovative technologies and EVs in the automotive sector. The acquired results for the optimistic and pessimistic scenarios of EV diffusion in the city of Santa Maria are depicted in Fig. 5.

Upon examination of Fig. 5, it becomes evident that in the optimistic scenario, all potential adopters will have acquired an EV by 2040, after 19 years. Conversely, in the pessimistic scenario, which considered significantly low weights for the groups proposed in the model, even over a 30-year horizon, the maximum number of consumers who could acquire the vehicle is not reached.

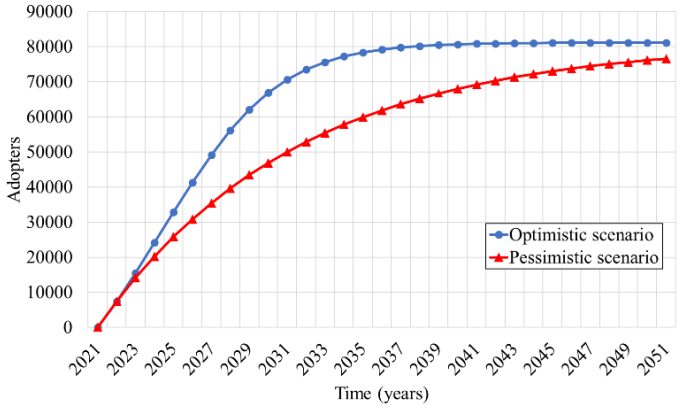

Fig. 5. Number of EV adopters for pessimistic and optimistic scenarios.

The results obtained in this study demonstrate the potential of the SDs technique when coupled with the Bass model. Simulations have allowed the observation of the dynamic behavior of the system in response to the variation of certain variable groups. For future studies, it is suggested to conduct further sensitivity analyses considering the established groups. Additionally, it is possible to extend the proposed groups by introducing more variables into the model and by extending the causal loop and stock-flow diagrams. This approach would enable a more detailed examination of parameters influencing residential consumers in their decision-making process regarding the acquisition of EVs.

Exploring the potential of SDs could involve investigating other relevant factors not addressed in this study, such as specific public policy tests, technological advancements, and the influence of additional factors on the EV adoption process. Furthermore, a more in-depth analysis of the relationships between the groups and a more dynamic approach to incorporate recent data, different EV models and technologies could further enhance the accuracy of the presented methodology and the validity of the results. These research opportunities suggest a wide range of possibilities for exploration and development in the application of SDs to the context of EV diffusion.

VI. CONCLUSION

This article presented the system dynamics technique and the Bass diffusion model, which were used to estimate the adoption of EVs by residential consumers over time. To this end, the theoretical foundation of these methods was discussed, as well as the steps for their successful implementation in a systemic context. The proposed model considered the innovation and imitation coefficients of the Bass model as well as five groups of parameters (economic, technical, political, socioenvironmental, and market), which influence consumer's decision-making. As verified during the research, both the SD technique and the Bass model have been used in various areas of knowledge with excellent results. Finally, given the versatility of the proposed model, it is possible to incorporate new dynamic variables into the EV diffusion study process, allowing to carry out numerous sensitivity tests and even more assertive and realistic analyses in different scenarios.

REFERENCES

[1] F. M. Bass, "Comments on 'A new product growth for model consumer durables,'" *Manage Sci*, vol. 50, no. 12 SUPPL., pp. 1833–1840, Dec. 2004, doi: 10.1287/MNSC.1040.0300.

[2] C. Domarchi and E. Cherchi, "Electric vehicle forecasts: a review of models and methods including diffusion and substitution effects," 2023, doi: 10.1080/01441647.2023.2195687.

[3] L. L. C. dos Santos, L. N. Canha, and D. P. Bernardon, "Projection of the diffusion of photovoltaic systems in residential low voltage consumers," *Renew Energy*, vol. 116, pp. 384–401, Feb. 2018, doi: 10.1016/j.renene.2017.09.088.

[4] E. M. Rogers, *Diffusion of Innovations*, 5th ed. New York: Free Press, 2003.

[5] J. D. Sterman, *Business dynamics: Systems thinking and modeling for a complex world*. Boston: McGraw-Hill, 2000.

[6] A. Ford, *Modeling the environment: An introduction to system dynamics models of environmental systems*, 1st ed. Washington D.C.: Island Press, 1999.

[7] J. Massiani and A. Gohs, "The choice of Bass model coefficients to forecast diffusion for innovative products: An empirical investigation for new automotive technologies," *Research in Transportation Economics*, vol. 50, pp. 17–28, Aug. 2015, doi: 10.1016/j.retrec.2015.06.003.

[8] D. Neumann, L. A. de Santa-Eulalia, R. T. Yoshino, and J. Klasen, "Um novo modelo de previsão de demanda para inovações radicais," *Production*, vol. 24, no. 3, pp. 605–617, Sep. 2013, doi: 10.1590/S0103-65132013005000077.

[9] Z. Ding, W. Gong, S. Li, and Z. Wu, "System Dynamics versus Agent-Based Modeling: A Review of Complexity Simulation in Construction Waste Management," *Sustainability 2018, Vol. 10, Page 2484*, vol. 10, no. 7, p. 2484, Jul. 2018, doi: 10.3390/SU10072484.

[10] M. R. Saavedra M., C. H. de O. Fontes, and F. G. M. Freires, "Sustainable and renewable energy supply chain: A system dynamics overview," *Renewable and Sustainable Energy Reviews*, vol. 82, pp. 247–259, Feb. 2018, doi: 10.1016/j.rser.2017.09.033.

[11] S. Selvakkumaran and E. O. Ahlgren, "Review of the use of system dynamics (SD) in scrutinizing local energy transitions," *J Environ Manage*, vol. 272, p. 111053, Oct. 2020, doi: 10.1016/J.JENVMAN.2020.111053.

[12] G. B. Schuch, "Um modelo para estudos da demanda de energia elétrica em ambiente competitivo," Tese (Doutorado em Engenharia Elétrica) - Universidade Federal de Santa Catarina, Florianópolis, 2000.

[13] F. M. Bass, "A New Product Growth for Model Consumer Durables," *Manage Sci*, vol. 15, no. 5, pp. 215–227, Jan. 1969, doi: 10.1287/mnsc.15.5.215.

[14] International Energy Agency (IEA), "Global EV Outlook 2023: Catching up with climate ambitions," 2023. Accessed: May 23, 2023. [Online]. Available: www.iea.org

[15] Plataforma Nacional de Mobilidade Elétrica (PNME), "2º Anuário Brasileiro da Mobilidade Elétrica," 2022. Accessed: Jun. 13, 2023. [Online]. Available: https://www.pnme.org.br/biblioteca/2o-anuario-brasileiro-da-mobilidade-eletrica-pnme/

[16] Y. Xiang, H. Zhou, W. Yang, J. Liu, Y. Niu, and J. Guo, "Scale Evolution of Electric Vehicles: A System Dynamics Approach," *IEEE Access*, vol. 5, pp. 8859–8868, 2017, doi: 10.1109/ACCESS.2017.2699318.

[17] A. E. Cenci, G. Bordin, R. P. Homrich, and L. T. R. Loureiro, "Estimation of Electric Vehicles in Dynamic Environment," *2019 IEEE PES Conference on Innovative Smart Grid Technologies, ISGT Latin America 2019*, Sep. 2019, doi: 10.1109/ISGT-LA.2019.8895418.

[18] Instituto Brasileiro de Geografia e Estatística (IBGE), "Cidades | Rio Grande do Sul | Santa Maria | Panorama." Accessed: Nov. 13, 2023. [Online]. Available: https://cidades.ibge.gov.br/brasil/rs/santa-maria/panorama

[19] Rádio Web Região Oeste Santa Maria RS, "Cidade ganha primeiro posto comercial de recarga para carros elétricos." Accessed: Nov. 13, 2023. [Online]. Available: http://bit.ly/3GbyTfM

TSO-DSO Cooperation under Mutiple Vertical Interconnections

Lars Stark, Lutz Hofmann
Institute of Electric Power Systems - Electric Power Engineering Section
Leibniz University Hannover
Hanover, Germany
stark@ifes.uni-hannover.de

***Abstract*— With the expansion of decentralised energy resources (DER), the distribution system operators receive active and reactive power flexibilities. These can be used by the distribution system operator (DSO) in its own grid, to optimise the voltage and minimize the loading of devices. Additional flexibilities can be offered to the transmission system operator (TSO) as ancillary services. The TSO can utilise these flexibilities in order to compensate for the shutdown of thermal power plants. One method to describe the active and reactive power potential that can be offered by the DSO to the TSO is the Feasible Operation Region (FOR). The concept of the FOR can only be applied to systems with one vertical interconnection. Therefore, approaches have been developed in the literature to further develop the concept. In this paper, an approach from the literature is analysed at a test system with two vertical interconnections. The aim of the approach is to describe the coupling of multiple interconnections by using probability distributions. The results show a need for an enhancement. Subsequently, an enhancement of the concept is introduced, which makes it possible to apply the FOR to multiple interconnections. A disadvantage is an underestimation of the flexibilities.**

Keywords—Probability Distribution, Feasible Operation Region, multiple Interconnections, Flexibility, TSO-DSO, safety Region

I. INTRODUCTION

The increasing number of decentral energy resources (DER) at the distribution grid levels and the associated shutdown of thermal power plants at the transmission grid level lead to reversing power flow directions between transmission and distribution grid. To control the vertical power flow in critical grid situations, processes such as the Redispatch 2.0 are applied. In this process DER with a capacity of more than 100 kW from the distribution grid level can be used to avoid congestions in the transmission grid [1].

Due to the shutdown of thermal power plants, the transmission system operator (TSO) also has less reactive power potential in its grid. In [2], a reactive power requirement of 25-40 Gvar is calculated for the transmission grid in 2050. In [2] it is shown that this demand can be covered by the reactive power potential of the distribution grid levels. According to the NOVA principle (grid optimisation before reinforcement before grid expansion), costs for the construction of compensation systems could therefore be saved.

Various concepts for DSO-TSO active and reactive power exchange are therefore being analysed in the literature. A key word in this context is flexibility. Due to the different use of this term [3], the ability to change the feed-in of DER is defined as flexibility in this paper. The DERs are referred to as flexibility providing units (FPUs). In [4], a promising way for the distribution system operator (DSO) to offer its flexibilities to the TSO is investigated. In the selected approach, the flexibilities are specified in the form of a PQ-Plane, which is called the Feasible Operation Region (FOR). It represents the maximum and minimum active and reactive power that can be exchanged between DSO and TSO.

Advantage of the approach is the consideration of constraints without providing the TSO with sensitive data about the distribution grid. As a consequence, a power exchange does not lead to violations of the voltage band or to a congestion in the distribution grid [4]. A current field of research in the area of the Feasible Operation Region, is the flexibility exchange between grid levels with more than one vertical interconnection [5–7], as it can typically occur between distribution and transmission system operators. Fig. 1 shows a TSO-DSO interface with two vertical interconnections (IC 1 and 2). The FOR of each interconnection is marked blue. The current operating point (OP) is marked with a black cross.

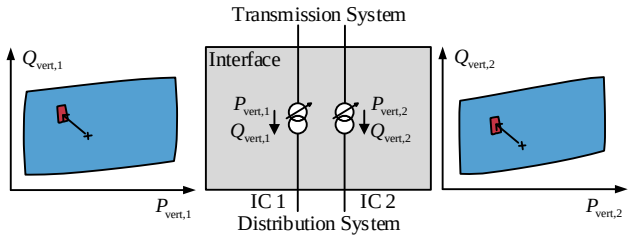

Fig. 1. TSO-DSO interface with two vertical interconnections [7]

With multiple interconnections, the FOR and thus the minimum and maximum power exchange can be determined individually for each interconnection. However, the selection of operating points within the FORs is subjected to coupling between each other. If for example the DERs in the distribution grid level reduce the power exchange at interconnection 1 (red area), the power exchange at interconnection 2 will also be reduced (red area). It is therefore not possible to control both OPs independently of each other. In addition to the FORs, the TSO therefore needs information on the coupling between the FORs so that only permissible operating point combinations between the interconnections are selected.

In [7], a literature review on multiple FORs and their mutual dependencies is given. A research paper [8] is highlighted in [7] that provides a promising approach for dealing with this challenge. The approach is a safest region concept, in which a probability distribution is specified within one of the FOR to describe the mutual dependencies. The probability distribution can be used to specify operating points that can be set with a high safety guarantee. This paper therefore examines the safest region approach in more detail and suggests an enhancement. The description of the safest region concept and the enhancement is shown in section II. In

This work was funded by the Deutsche Forschungsgemeinschaft (DFG, German Research Foundation) project number - 497762376

Section III both concepts are tested at a TSO-DSO interface with two vertical interconnections. This is followed by the conclusion.

II. Safest Region Concept

The FORs and their mutual dependencies must be determined to calculate the probability distribution for the safest region approach. For this purpose, a method from [7] is adopted first, which is called the static method.

A. The static method

In Fig. 2, the static method is applied to a system with two vertical interconnections. In this method, the FOR at interconnection 1 is divided into several subareas called grid cells using a static meshed grid. For interconnection 2, a permissible FOR is determined for each of these grid cells. The results are grid cell-FOR combinations, which describe the coupling between both interconnections. An exemplary grid cell-FOR combination is marked red [7].

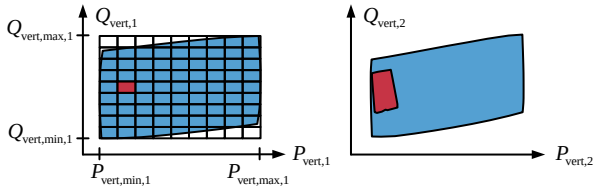

Fig. 2. Static method at a system with two vertical interconnections [7]

The blue FOR is named maximum FOR in the following. The length and width of the static meshed grid is defined by the maximum $(P_{vert,max,1}, Q_{vert,max,1})$ and minimum $(P_{vert,min,1}, Q_{vert,min,1})$ vertical power flows.

With the static method, it is important to keep the size of the grid cells small. This is also due to the mutual coupling of the interconnections. If the grid cell is too large, the mutual coupling occurs again. The TSO may therefore only select a grid cell instead of an OP at the interconnection with the static-meshed grid. A compromise must therefore be found between accuracy of the grid cell and the computational effort for the DSO. The grid cell size can be defined by the active power accuracy w_P and reactive power accuracy w_Q. The number of grid cells in the direction of active power $R_{P,1}$ and reactive power $R_{Q,1}$ is given by [7]:

$$R_{P,1} \approx \frac{\left|P_{vert,max,1} - P_{vert,min,1}\right|}{w_P}$$
$$R_{Q,1} \approx \frac{\left|Q_{vert,max,1} - Q_{vert,min,1}\right|}{w_Q} \quad (1)$$

The static method can be used to determine the mutual coupling of the FORs. If more than two interconnections are considered, each additional interconnection must also be overlaid with a meshed grid. The associated FOR must then be determined for each grid cell combination. This increases the computational effort exponentially [7]. In the next section, the static method serves as the basis for calculating a probability distribution. The safest regions within the FOR can then be determined from the probability distribution. The method in the next section thus equals the approach from [8].

B. Probability distribution

To determine the probability distribution, the permissible FORs resulting from the static method are superimposed at interconnection 2. Fig. 3 shows this process graphically for three grid cells which are marked yellow, red and green.

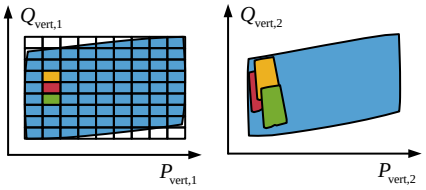

Fig. 3 Three marked grid cells and permissible FORs

The overlap is counted at each point within the FOR at interconnection 2 and divided by the total number of grid cells. This results in a probability distribution. Grid cells that lie outside the FOR and therefore do not allow any permissible operating points need to be deducted from the total number of grid cells. The TSO can now select any operating point at interconnection 1. At interconnection 2 he is given areas that can be set with a certain probability by the DSO.

Fig. 3 shows that permissible FORs on the left side of the maximum FOR do not reach the right side of the maximum FOR. Therefore, there will be no areas that can be set with a 100% probability. In order to be able to specify areas of high probability in the sense of a safety region, an enhancement called the operating area dependent probability distribution is presented below.

C. Operating area dependent probability distribution

With the operating area dependent probability distribution, the probability distribution is only given for a part of the FOR at interconnection 1, which reduces the total number of grid cells. The enhancement is shown in Fig. 4 for two different areas of the FOR.

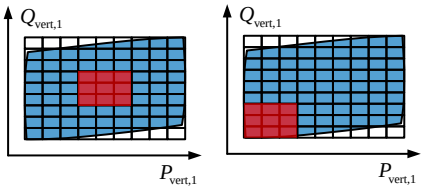

Fig. 4 Meshed grid with two different operating areas

This procedure ensures that the majority of the FORs belonging to the grid cells overlap at least in one point. The selection of the area can depend, for example, on the current operating point. Assuming that the TSO only wants to make a small change of the operating point, a high probability and therefore a high reliability could be given. The operating area dependent probability distribution therefore involves a compromise between the size of the flexibility area at interconnection 1 and the probability values for interconnection 2.

III. Simulation

In this section the operational functionality and accuracy of the probability distribution and operating area probability distribution method are tested and compared to each other. For this purpose, an exemplary distribution system with two vertical interconnections to a transmission system is used.

A. Distribution System

The distribution system is taken from [7] and the grid topology is shown in Fig. 5. The mathematical description of the FOR determination can also be found in [7]. The PQ-

planes of the flexibility providing units that determine the shape of the FORs are given in the Appendix. The voltage level of the distribution grid is 110 kV and thus resembles a high-voltage (HV) grid. The transmission system is not available to the DSO in reality and is represented by a slack node for FOR determination. The voltage is 220 kV, corresponding to an extra high-voltage (EHV) grid.

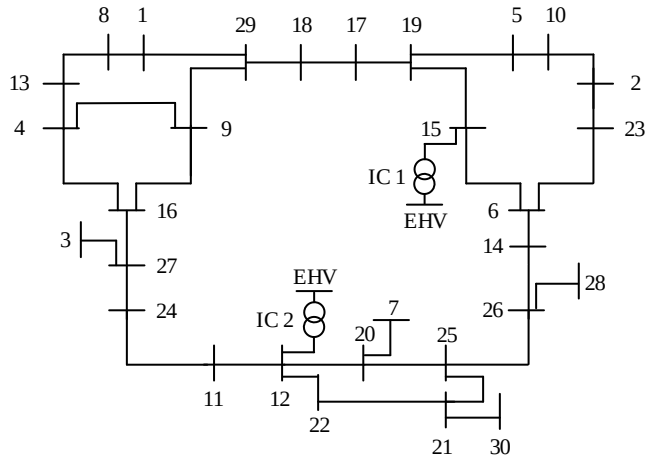

Fig. 5. 30 bus meshed HV grid with two vertical interconnections [7]

To calculate the probability distribution, the dependencies between the two interconnections are first determined using the static method. For the static method, the active and reactive power accuracy must first be defined. For this purpose, the influence of the grid cell size on the FOR is analysed in the next section.

B. *Influence of the grid cell size on the FOR*

Fig. 6 shows the corresponding FORs for three different grid cell sizes. The yellow grid cell has a size of 24.58 MW and 11.16 Mvar. The red grid cell is smaller by a factor of 9 in both width and length. The third grid cell is green and is smaller than the red one by a factor of 9 in width and length. Due to the resulting size, the green grid cell cannot be recognised in the graphic.

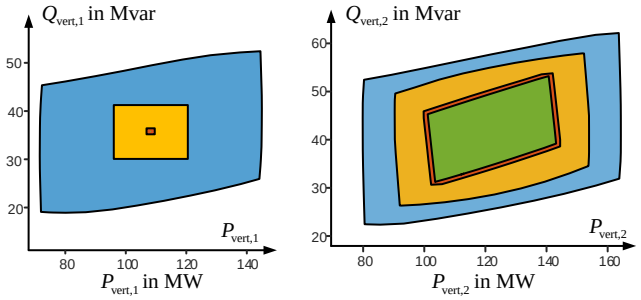

Fig. 6 Reduction of the grid cell size and permissible FORs

It can now be seen that the associated FORs also become smaller, but less than by a factor of 9. If the red FOR is compared with the green FOR, the area remains almost constant. It can be concluded that from a certain size of the grid cell, the coupling within the grid cell and the permissible FOR disappears. As a compromise between the removal of the coupling and the computational effort for the static method, the red grid cell size (2.73 MW and 1.24 Mvar) is selected for further investigations.

C. *Probability distribution*

Fig. 7 shows the FOR at interconnection 1 with the associated static meshed grid. The meshed grid consists of 27x27 grid cells. The total grid cell number is therefore 729. The second graph in Fig. 7 shows the corresponding probability distribution for interconnection 2. Because 95 grid cells lie outside of the FOR at interconnection 1, 634 permissible FORs were calculated and superimposed according to the static method in order to determine the probability distribution.

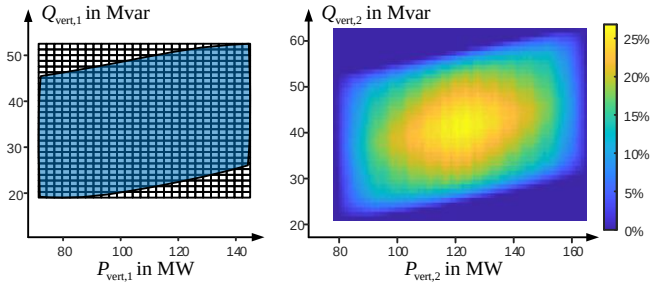

Fig. 7 Meshed grid and resulting probability distribution

With the probability distribution, the shape of the original FOR at interconnection 2 can be recognised, as outside the FOR is a probability of 0%. Inside the FOR the probability is always greater than 0%. Furthermore, the highest probability can be seen in the centre with values slightly above 25%, which decreases towards the edges. A probability of 25% means that 25% of all permissible FORs overlap in the centre. Therefore, an operating point in the centre of the FOR at interconnection 2 can be set with a probability to 25% for any operating point at interconnection 1.

The reason for the shape and values of the probability distribution lies in the coupling of the interconnections, which will now be analysed in more detail. Fig. 8 shows the FORs for various grid cells positions.

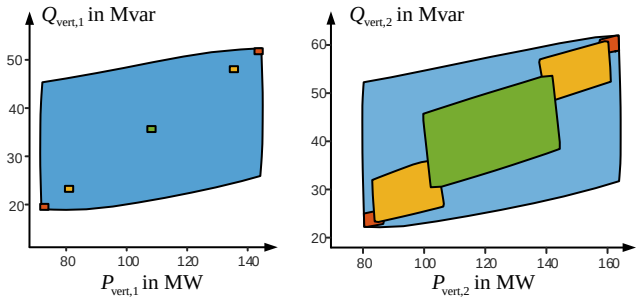

Fig. 8 Various grid cell positions and permissible FORs

The coupling can be seen by the position of the grid cells and the permissible FORs. A grid cell located in the bottom left corner, lead to a permissible FOR, which is also located in the bottom left corner. As a consequence, no high probabilities can be achieved, as the permissible FORs do not overlap the further away the grid cells are from each other. There are also clear differences in the size of the FORs. The more central a grid cell is, the larger is the area of the permissible FOR. As a result, the probability distribution in Fig. 7 is greatest in the centre and decreases towards the edge. To increase the probability, the operating area dependent distribution method is investigated in the next section.

D. *Operating area dependent probability distribution*

The aim of the operating area dependent distribution method is to achieve higher probabilities of up to 90%. The following section therefore analyses how large an operating area is allowed to be to achieve these values. As it was shown

in the last section the permissible FORs differ significantly in size. As a consequence, this investigation is carried out for an operating area in a corner (case a)) and in the centre (case b)) of the FOR. Both cases are shown in Fig. 9.

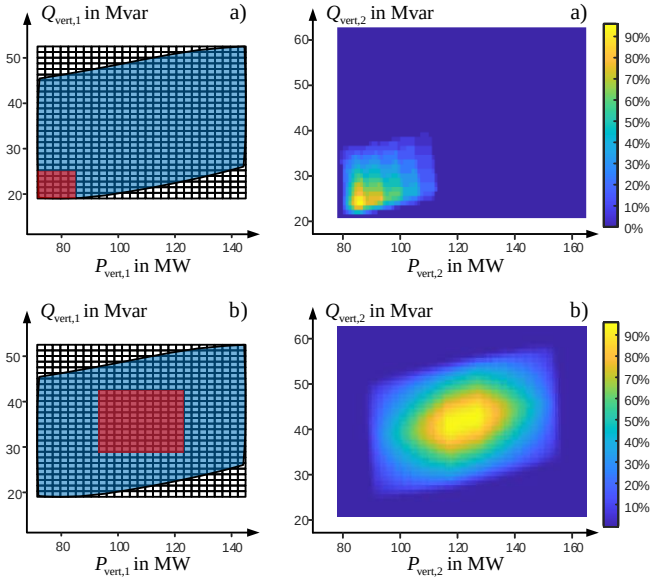

Fig. 9 Operating area dependent distribution for case a) (top) and case b) (bottom)

For probability values of over 90%, the operating area for test case a) may not exceed 5x5 grid cells. For test case b), the maximum operating area is 11x11 grid cells. The differences between the test cases result from the correlations shown in the section before. The more central a grid cell is, the greater is the FOR. Grid cells that are in the centre can therefore be further apart than grid cells that are at the edge of the FOR. The correlation between the size of the FOR and the position of the grid cell also means that the flexibility at interconnection 2, which can be specified with a probability over 90%, also differ significantly in size. By reducing the flexibilities at interconnection 2 to a safest region, this method leads to an underestimation of the flexibilities, this relation is evident in case a).

IV. Conclusion

In this paper, as a first step a safest region method was analysed, which describes dependencies between multiple interconnections in the context of flexibility exchange. The aim of the method is to calculate a probability distribution that can be used to determine flexibilities, which can be safely provided by the DSO to the TSO. The simulation results in this paper shows, that the safest region method leads to probability values, which are not sufficient to give the TSO high safety guarantees. In a second step the method was extended in order to ensure higher probability values and thus also higher safety guarantees. The extension was based on determining an operating area dependent probability distribution. By restricting the flexibility exchange to a subarea of the FOR, an increase in the probability values could be shown on the basis of simulations.

A general disadvantage of both methods is the underestimation of the flexibilities, which is particularly evident in the case of operating points at the edge of the FOR. In order to utilise the entire flexibility potential of the distribution grid level, other methods should therefore be investigated.

References

[1] Bundesnetzagentur, "Redispatch," [Online]. Available: https://www.bundesnetzagentur.de/DE/Fachthemen/ElektrizitaetundGas/Versorgungssicherheit/Netzengpassmanagement/Engpassmanagement/Redispatch/start.html

[2] Deutsche Energie-Agentur, " dena-Studie Systemsicherheit 2050," 2020. [Online]. Available: https://www.dena.de/fileadmin/dena/Publikationen/PDFs/2020/dena_Systemsicherheit_2050_LANG_WEB.pdf

[3] Taulant Kerci, "On the Definition and Classification of Power System Flexibility," in *Innovative Smart Grid Technologies (ISGT) Europe (accepted)*, Grenoble, France, 2023.

[4] R. Schwerdfeger, "Vertikaler Netzbetrieb: Ein Ansatz zur Koordination von Netzbetriebsinstanzen verschiedener Netzebenen," Ph.D. dissertation, Tech. Univ. Ilmenau, Germany, 2017. [Online]. Available: https://d-nb.info/113079220X/34

[5] J. Silva *et al.*, "A Data-Driven Approach to Estimate the Flexibility Maps in Multiple TSO-DSO Connections," in *IEEE Transactions on Power Systems*, vol. 38, no. 2, pp. 1908-1919 , 2023.

[6] N. Majumdar, M. Sarstedt, and L. Hofmann, "Distribution grid power flexibility aggregation at mutiple interconnections between the high and extra high voltage grid levels," in *IEEE PES GTD International Conference and Exposition (GTD)*, Istanbul, Turkiye, 2023, pp. 303–309.

[7] L. Stark, M. Sarstedt, and L. Hofmann, "Determination of Interdependent Feasible Operation Regions at Multiple TSO-DSO Interconnections," in *Innovative Smart Grid Technologies (ISGT) Europe (accepted)*, Grenoble, France, 2023.

[8] A. Kubis, A. Singh, G. Torres-Villarreal, and S. Leksawat, "Determination of Real-Time Interdependent Flexibility on Multiple Grid Connection Points in an Active Distribution Network," in *Cigre Session*, Paris, France, 2022.

Appendix

The PQ-planes of FPUs are assumed to be rectangular. The active power flexibility results from the reduction of the load and the reduction of the feed-in of the DER:

$$-0,3P_{\text{load},i} \le \Delta P_{\text{FPU},i} \le P_{\text{DER},i} \tag{2}$$

The reactive power flexibility results from the active power of the DER:

$$P_{\text{DER},i}\tan(\varphi) \le \Delta Q_{\text{FPU},i} \le -P_{\text{DER},i}\tan(\varphi) \quad \text{with } \varphi = \arccos(0,95) \tag{3}$$

The loads and DER are listed in TABLE I.

TABLE I. Node Data of FPUs

Node	*Load*	*DER*	*Node*	*Load*	*DER*
1	8.65 MW	3.04 MW	16	13.00 MW	4.41 MW
2	5.66 MW	1.93 MW	17	11.30 MW	4.00 MW
3	5.53 MW	-	18	13.61 MW	4.69 MW
4	8.56 MW	3.04 MW	19	4.32 MW	1.52 MW
5	4.94 MW	1.66 MW	20	11.90 MW	3.45 MW
6	10.36 MW	4.00 MW	21	4.83 MW	1.65 MW
7	7.73 MW	2.62 MW	22	11.90 MW	4.69 MW
8	12.72 MW	4.42 MW	23	6.28 MW	2.21 MW
9	12.24 MW	4.28 MW	24	10.68 MW	3.73 MW
10	5.55 MW	1.93 MW	25	11.71 MW	4.00 MW
11	11.27 MW	3.86 MW	26	5.26 MW	1.79 MW
12	-	-	27	8.61 MW	2.90 MW
13	9.82 MW	3.45 MW	28	9.26 MW	3.31 MW
14	7.68 MW	2.76 MW	29	-	-
15	-	-	30	8.94 MW	3.04 MW

Harmonic stability assessment of commercially available single-phase photovoltaic inverters in public low voltage networks

Elias Kaufhold
Institute of Electrical Power Systems
and High Voltage Engineering
Technische Universitaet Dresden
Dresden, Germany
elias.kaufhold@tu-dresden.de

Jan Meyer
Institute of Electrical Power Systems
and High Voltage Engineering
Technische Universitaet Dresden
Dresden, Germany

Peter Schegner
Institute of Electrical Power Systems
and High Voltage Engineering
Technische Universitaet Dresden
Dresden, Germany

***Abstract*—The growth of renewables in public low voltage (LV) networks leads to an increasing number of installed photovoltaic (PV) systems and respective inverters. For low power applications, single-phase inverters connect the PV system to the LV network and interact via the injected current and the voltage at the Point of Connection. Critical network conditions can lead to an instability of the inverter. In practice, a challenge of the stability assessment is the undisclosed design, i.e. the inverter topology and the parameters. This paper presents the measurement-based harmonic stability assessment for commercially available inverters based on simple network equivalents and on field measurements of public LV networks.**

Keywords—harmonic stability, inverters, low voltage networks, measurements, photovoltaics.

I. INTRODUCTION

To fulfill the climate goals, an increase of installed renewable energy generators in public low voltage (LV) networks has become a trend over the last years [1]. These renewable energy generators are typically connected to the LV network via power electronic (PE) devices. For photovoltaic (PV) systems, the grid-connected PE device is an inverter.

It is a general aim of network operators, e.g. distribution system operators (DSO) to ensure a reliable operation of the power grid. With the increasing power supply by PV systems, the stability of these inverters is consequently an important topic.

The increasing number of installed PE devices, e.g. modern loads but also network equipment, comes along with a reduction of the network damping, e.g. damping loads. In addition, the high penetration of inverters and converters that interact with other PE devices and the LV network, cause distorted voltages at individual Points of Connections (PoC's) due to their nonideal voltage current characteristics. In the past, shut downs of PE devices due to the interaction at frequencies above power frequency, e.g. 50 Hz, have been reported. Related to the bandwidth of the control, the phenomenon has been called a harmonic instability and is studied in the harmonic frequency range up to 2 kHz [2].

While elaborate white-box studies have been developed in detail, the required knowledge for these studies is typically not available for the DSO's. On the other hand, the manufacturers have no information about the network topology and the installed network equipment.

This work was funded by the Deutsche Forschungsgemeinschaft (DFG, German Research Foundation) – 360497354.

The aim of the presented work is therefore the harmonic stability analysis of commercially available single-phase inverters for photovoltaic applications in public LV networks.

Section II introduces briefly the state of the art with respect to the knowledge-based classification of inverter studies, the black-box modeling of the entire system and the harmonic stability analysis. Section III presents the harmonic stability and respective measurements. Furthermore, the operating power is identified as a non-linear model parameter and a holistic assessment of six commercially available inverters is performed based on probabilistic network considerations. Limitations of the assessment are also disclosed. In section IV, the conclusion summarizes the presented results and addresses future work.

II. STATE OF THE ART

A. Inverter studies

Inverter studies can be classified according to the available knowledge into white-box, grey-box and black-box studies.

1) White-box studies

White-box studies require detailed knowledge about the inverter design in terms of its topology and the respective parameter values. The most detailed white-box model is the switched model in time domain. A drawback of this model is the high computational effort next to the high implementation effort. The authors have proposed a modular modeling approach in [3] to ease the implementation of different designs by using similar individual component designs in different combinations to create different inverter designs. The designed inverters can be used for linearity studies analytically and for simulations.

2) Grey-box studies

Grey-box models are interesting for future studies when partial knowledge about the device is available but not all required model parameters are known. While identification methods of generic components, e.g. the grid-side filter circuit and the DC-link capacitance have been proposed ([4], [5]), also the identification of parameters for known topologies accounts into grey-box studies [6]. Grey-box study approaches are very promising but currently, missing identification methods for more device components and the development of grey-box equivalent models have to be developed.

3) Black-box studies

Black-box studies are the most generic and require no detailed model. All model parameters are identified by measurements. Currently, linearized models form the state of

the art, e.g. see the later section II.B, while also nonlinear model structures, such as the Hammerstein-Wiener model [7]–[9] and Neural networks [10] have been studied. However, the nonlinear models have to be studied in more detail to be used in large-scale system studies or elaborate simulations in the harmonic frequency range. To identify these models, e.g. see section II.B.2.a, measurement-based methods have been developed and later optimized. The parametrized black-box models can be used for further studies, e.g. for Harmonic Power Flow (HPF) analysis or with regard to this work for the harmonic stability analysis.

B. Small signal black-box system model

The small signal black-box system model can be separated into two parts: the inverter and the LV network as depicted in Fig. 1.

1) Low voltage network

The LV network is typically represented by a Thevenin equivalent model that consists of a frequency-dependent network impedance $\underline{Z}_\mathrm{g}(f)$ and a voltage source with the background voltage $\underline{U}_\mathrm{g}(f)$ that can also apply components at higher frequencies, i.e. a distortion, next to the power frequency.

2) Inverter

Grid-following single-phase commercially available inverters can be represented by the Coupled Norton model. The condition of a linear dependency on the voltage at the PoC is required to make use of this model for any represented device. The model consists of an uncontrolled current source that injects the current into the LV network that has been identified at a specifically chosen voltage, i.e. the reference voltage with a sinusoidal waveform for which Fig. 1 accounts. Voltage distortion deviations from the reference voltage are represented by the admittance and the controlled current source. The admittance reflects the currents at the same voltage frequencies at which the inverter is excited at the PoC. Furthermore, due to internal signal convolutions, currents result at frequencies other than the exciting voltage frequencies and are called frequency coupling components. These current components are considered by the controlled current source.

a) Measurement-based identification

The voltage-current response in the harmonic frequency range including the frequency coupling components can be represented by frequency coupling matrices (FCM). To identify such a matrix, first the reference voltage is applied. Afterwards, a frequency sweep is applied over an additional single-frequent voltage distortion according to [11] while for each measurement point *i*, the multi-frequent current response is recorded. If the current response at reference voltage is subtracted from the specific measurement point, the lines and rows of the matrix can be calculated elementwise by

$$\underline{Y}_\mathrm{Inv}(f_I, f_U) = \frac{\underline{I}_{\mathrm{PoC}\,i}(f_I) - \underline{I}_{\mathrm{PoC\,ref}}(f_I)}{\underline{U}_{\mathrm{PoC}\,i}(f_U) - \underline{U}_{\mathrm{PoC\,ref}}(f_U)}. \qquad (1)$$

The Coupled Norton model and the respective FCM are related to linear time-periodic (LTP) system theory [12]. If the LTP model is averaged or the frequency coupling components are neglected, both leads to the LTI model, e.g. the classical admittance, i.e. the uncoupled Norton model.

3) Harmonic stability analysis

The harmonic stability analysis studies the interaction of the inverter and the power system, e.g. LV networks, above power frequency. In practice, most studies are performed up to 2 kHz. The bandwidth of the control, specifically of the Phase locked loop (PLL) has a major impact, affects the overall active frequency region of the inverter impedance and consequently the stability of the inverter. In general, harmonic stability studies assume that the harmonic power is much smaller than the power at power frequency.

a) White-box analysis

White-box harmonic stability analysis is typically performed based on Eigenvalues, e.g. by zero-pole mapping. For commercially available devices, the poles and zeros of the transfer function are not known which is why the black-box analysis has to be applied.

b) Black-box analysis

The black-box harmonic stability analysis makes use of the (simplified) Nyquist criterion that states that the entire system is stable, if the open-loop transfer function does not encircle the point (-1, j0) in the complex plane. With regard to PE and power systems, the specific methodology is also called the impedance-based stability assessment [13]. Typically, the current at the PoC is of interest and can be calculated by

$$\underline{I}_\mathrm{PoC}(f) = \frac{\underline{I}_{\mathrm{PoC\,ref}}(f)\underline{Z}_\mathrm{Inv}(f)}{\underline{Z}_\mathrm{Inv}(f) + \underline{Z}_\mathrm{g}(f)} - \frac{\underline{U}_\mathrm{g}(f)}{\underline{Z}_\mathrm{Inv}(f) + \underline{Z}_\mathrm{g}(f)} \qquad (2)$$

or rather

$$\underline{I}_\mathrm{PoC}(f) = \left(\underline{I}_{\mathrm{PoC\,ref}}(f) - \frac{\underline{U}_\mathrm{g}(f)}{\underline{Z}_\mathrm{Inv}(f)}\right)\frac{1}{1 + \frac{\underline{Z}_\mathrm{g}(f)}{\underline{Z}_\mathrm{Inv}(f)}}. \qquad (3)$$

Though (3) is only a reformulation of (2), it becomes more visible, that if at least one of the two denominators becomes virtually zero, the current at the PoC will become extremely large. In practice, $|\underline{Z}_\mathrm{Inv}(f)|$ will be always greater zero and is uncritical. However, if the ration of $\underline{Z}_\mathrm{g}(f)$ to $\underline{Z}_\mathrm{Inv}(f)$ becomes -1, the denominator is zero. With regard to classical stability theory, the ration of -1 can be considered regarding

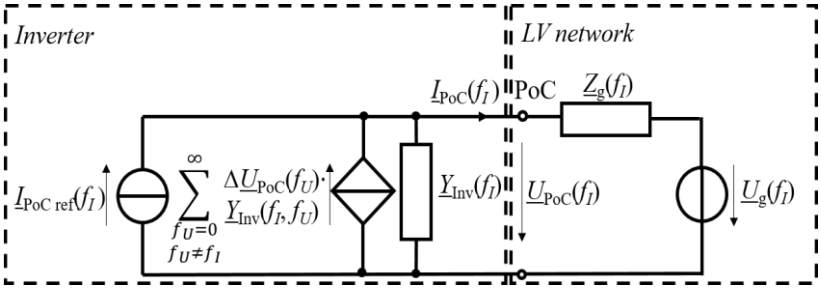

Fig. 1 Coupled Norton model of a PV inverter and the LV network.

its amplitude of one (amplitude criterion) that implies the intersection of the inverter impedance and the network impedance in the magnitude plot. And secondly, regarding its sign or rather the phase of being negative which can be formulated analytically by

$$\Phi_{\mathrm{PM}} = 180° - \Phi_{Z\,\mathrm{g}} + \Phi_{\mathrm{Z\,Inv}} \quad (4)$$

and thus the requirement according to passivity theory of

$$\Phi_{\mathrm{PM}} > 0 \quad (5)$$

for the entire system to ensure the stability of the inverter. As a consequence of (4), highly inductive network impedances are most critical.

III. HARMONIC STABILITY

Commercially available inverters have to be analyzed measurement-based if no white-box model is available.

1) Measurement setup

The measurement setup is depicted in Fig. 2. The DC power generator with a rated power of 7 kW enables to emulate the PV panels and respective strings. The overvoltage protectors SPD_1 and SPD_2 are installed to prevent overvoltages, specifically at the terminals of the grid simulator that is a controllable power source with a rated power of 45 kVA and a very low input impedance of below 1 Ω in the frequency range up to 2 kHz. To set different inductance values for the network impedance, air coils are implemented and form the test impedance $\underline{Z}_{\mathrm{test}}$ [14]. The magnetic coupling between the air coils can be adjusted by changing the air gap between the coils thus affecting the overall inductance of $\underline{Z}_{\mathrm{test}}$. The operating power of the inverter is varied related to its rated power of 4.6 kW in terms of 1 kW as low power, 2.5 kW as medium power and 4.5 kW as high power operating point.

2) Operating point dependency

Previous white-box studies and measurements have shown the linear dependency of the inverter impedance on the voltage distortion at the PoC. However, the power buffering in the DC-link capacity from the DC to AC power conversion causes a power-dependent ripple on the DC-link voltage. The convolution of this DC-link voltage ripple with the originally intended control output at the inverter bridge leads to a dependency on the operating power. The magnitudes and phase angles of a commercially available single-phase inverter are depicted in Fig. 3. The test impedance that emulates the network impedance is changed in its inductance values as plotted in Fig. 3 and the values of each measured test scenario are listed in table I together with the measured results in terms of its power-dependent stability. The measurements validate the assumption that high operating powers cause the inverter to become instable for lower inductance values (*RL*-equivalent network impedance model with low damping, i.e. a small resistance). For the measurements, no additional resistor has been implemented so that the resistive part of $\underline{Z}_{\mathrm{test}}$ consists only of the parasitic resistance of the air coils and the wiring.

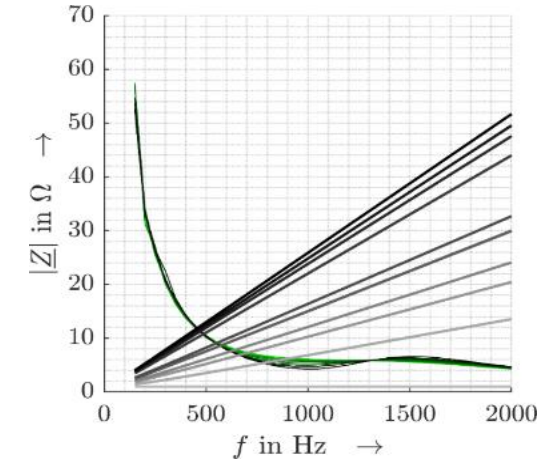

(a)

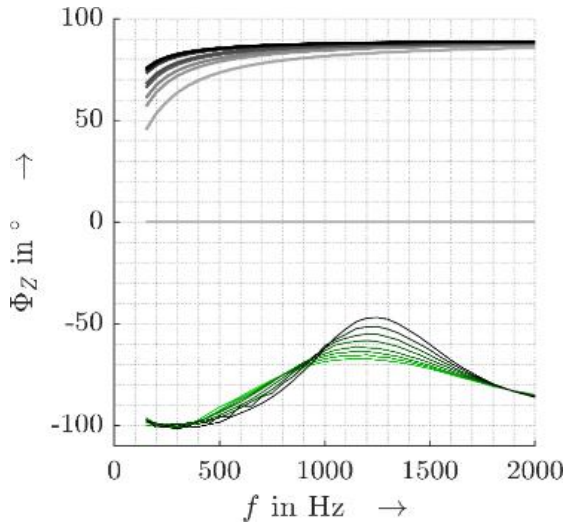

(b)

Fig. 3 Magnitude (a) and phase angle (b) characteristics of inverter impedance (green) and test impedance (grey).

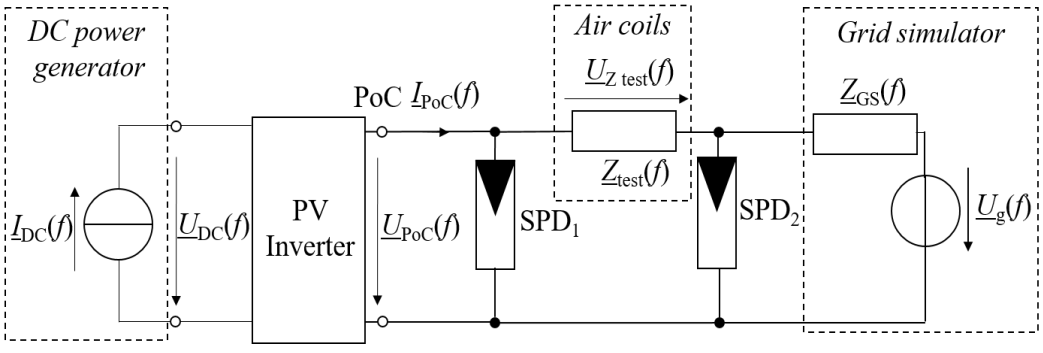

Fig. 2 Measurement setup.

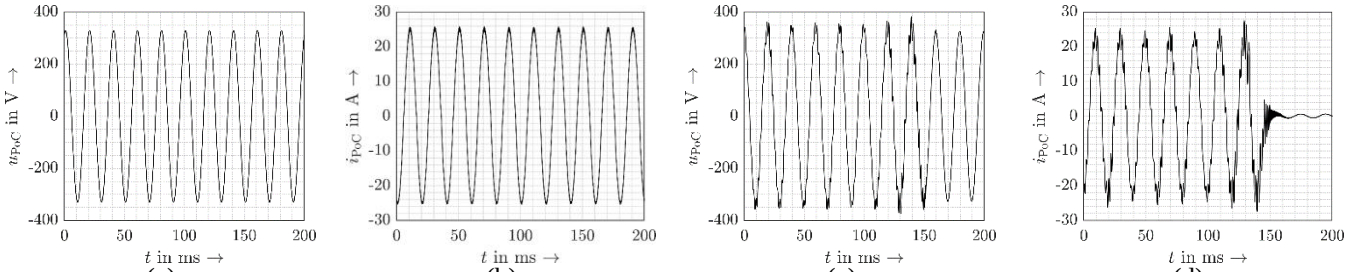

Fig. 4 Time domain measurements at 4.5 kW for voltage (a, c) and current (b, d) at the PoC for no intended applied test inductance (a, b - stable) and a test inductance of 2385 µH (c, d – instable with shut down).

TABLE I. MEASUREMENT SCENARIOS

Test scenario n°	*L* measurement @1 kHz	Operating power		
		1 kW	2.5 kW	4.5 kW
1	No intended *L*	stable	stable	stable
2	1074 µH	stable	stable	stable
3	1625 µH	stable	stable	stable
4	1915 µH	stable	stable	Stable
5	2380 µH	stable	stable	Stable (multiple attempts to start)
6	2385 µH	not tested	not tested	instable
7	2600 µH	stable	stable	not started
8	3500 µH	stable	stable	not started
9	3785 µH	stable	stable	not started
10	3943 µH	stable	instable	not started
11	4112 µH	instable	not started	not started

The time domain plots of the measurements for an instable and a stable scenario at 4.5 kW are shown in Fig. 4. The measurements present the shut down that is visible in Fig. 4 d of scenario 6.

The measurements have demonstrated the feasibility of the black-box stability analysis theory. To study the characteristics of the harmonic stability of commercially available inverters more general, two more commercially available single-phase inverters and four single-phase simulation models of possible inverter designs are analyzed by applying the validated theory.

To assess the operating point dependency, e.g. in this study in 500 W steps, and the critical inverter conditions in more detail, two values are identified, namely the critical inductance and the critical frequency.

The critical inductance is defined as the lowest inductance value that violates the Nyquist criterion. The critical frequency is defined as the frequency at which the inverter impedance and the network impedance intersect. The values for the seven studied inverter designs are depicted in Fig. 5.

The results demonstrate in many cases a lower critical inductance and a higher critical frequency for higher operating powers though resonances in the lower frequencies (some hundred Hz as for the inverters plotted in blue and purple in Fig. 5) can cause deviations from the monotonous relation. The study of one of the inverters (orange star in Fig. 5) indicates a very high critical inductance value for an operating point of 500 W and for higher operating powers an overall stable operation. This is a clearly good indicator for the stability characteristics of this inverter.

3) Probabilistic assessment

The previously studied network impedances have been limited to *RL*-equivalent models. In real LV networks, the impedance characteristics vary largely between different networks, e.g. by the resonance amplification, the resonance frequency, the q-factor (bandwidth of the resonance) and the phase angle characteristics around the resonance. To consider more realistic network impedances, the data of a large measurement campaign [15] in public LV networks in

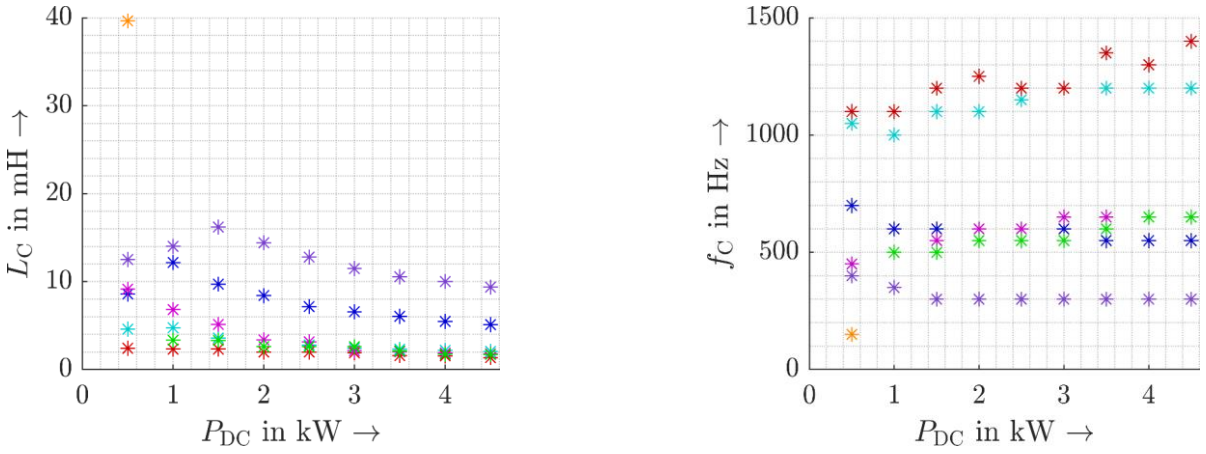

Fig. 5 Power-dependent critical inductances of three commercially available inverters and four simulation models.

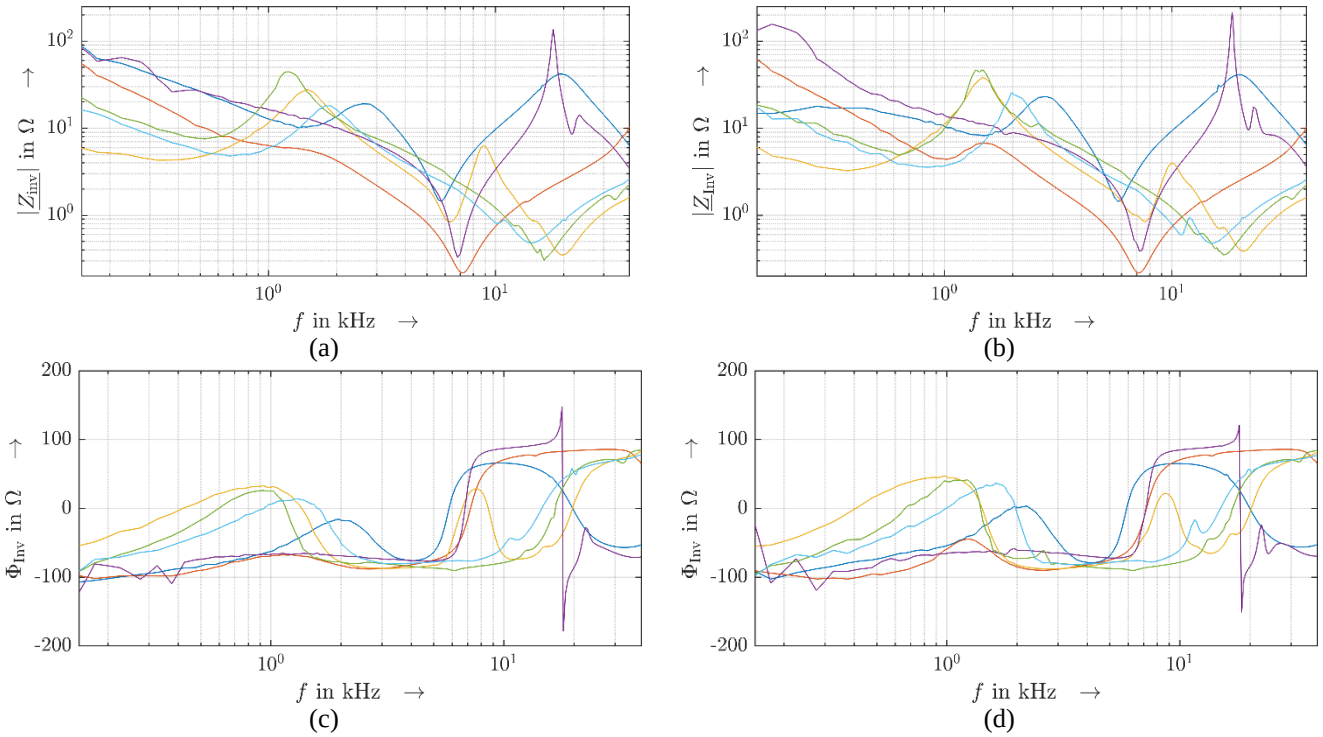

Fig. 6 Magnitude (a, b) and phase angle (c, d) characteristics of six commercially available inverters for 10 % of rated power (a, c) and 100 % of rated power (b, d).

Germany, Austria, Switzerland and the Czech Republic are used probabilistically to assess the inverter stability [16].

For this study, a different set of inverters has been used that consists of two single-phase inverters, one 3x-single-phase inverter (sometimes called artificial three-phase inverter) and three three-phase inverters (single-phase equivalent model is studied in the following). As this study has been performed before the study in the previous section II.2) the simulation model was not developed and the other single-phase inverter was not available yet. The respective impedance characteristics up to 39 kHz based on the frequency sweep are depicted in Fig. 6.

a) Network impedances

The data of the measurement campaign consists of 120 loop impedances. The measurements have been performed at junction boxes (75 % of the data) and at LV busbars in MV/LV substations (25 % of the data). About 80% of the impedances showed a first resonance peak between 600 Hz and 1.8 kHz. The measured network impedances are presented in Fig. 7.

The application of the Nyquist criterion on the measured network impedances and the inverter impedances indicated no critical combination.

b) Additional phase margin

However, the measurements of the LV networks have not been performed directly at the costumer terminals where the inverters are usually connected, e.g. the network impedance at a specific PoC can be different. In addition, other grid-connected devices at the PoC of the studied inverter might affect the network impedance characteristics, e.g. by causing a more capacitive or inductive phase angle. In general, the network impedance is typically dependent on daytime and season. Therefore, an additional phase margin reserve of 30° is considered so that (4) is reformulated to

$$\Phi_{\mathrm{PM}} = 180° - \Phi_{Z\,\mathrm{g}} + \Phi_{\mathrm{Z\,Inv}} - 30°. \qquad (6)$$

Finally, the assessment can be repeated for the adapted phase margin.

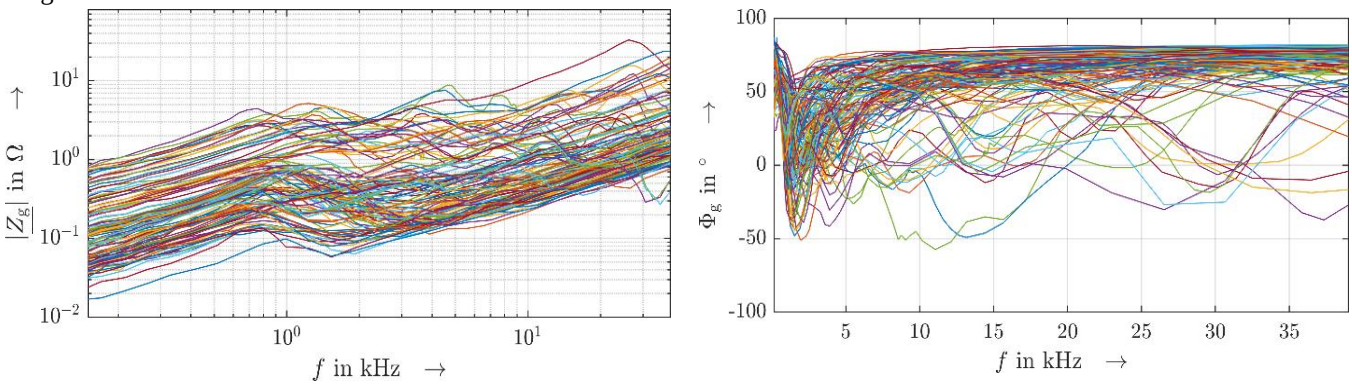

Fig. 7 Network impedances of public low voltage networks.

c) Grid compatibility index

To assess the stability with regard to the large number of different LV networks more comprehensively, the grid compatibility index (gci) is introduced. It can be calculated by

$$\text{gci} = 1 - \frac{n_c}{n_{tot}} \quad (7)$$

based on the number of critical measurement sites n_c related to the total number of considered measurement sites n_{tot}. A gci of one implies no critical measurement sites while the lower the gci, the worse the grid-compatibility of the inverter. The gci's of the six studied inverters considering the inverter impedances at 10 % and 100 % of the rated power are listed in table II.

TABLE II. GRID-COMPATIBILITY INDEX GCI

Inverter	**1**	**2**	**3**	**4**	**5**	**6**
gci	1	0.967	0.959	0.067	0.926	0.984

4) Assessment limitations

The previous sections have indicated that the Nyquist criterion is feasible to identify a harmonic instability. Measurements by the authors have however shown recently, that in reverse, this cannot be used as a general indicator that the inverter consequently operates stable. In practice, overvoltage and overcurrent protectors can cause the inverter to shut down though the system is theoretically considered by classical means of stability. To analyze the overall stable operation, also the background distortion and consequently the immunity of the inverter is of importance. To demonstrate the impact of a stable but present background distortion, scenario 10 (1 kW operating power, 3943µH test inductance) is studied for a setup with a sinusoidal background voltage waveform and a flat-top background voltage waveform. The flat-top voltage waveform is often found in public LV networks in central and western Europe.

The time domain measurements are presented in Fig. 8. Though the voltage distortion in the background voltage is not exceeding typical distortion limits, e.g. as in *IEC 50160*, the inverter shuts down when being exposed to the distortion and not the sinusoidal voltage. This clearly demonstrates the need for a more comprehensive and holistic study of the overall stable operation, even when limited to harmonic stability studies, instead of simply analyzing the stability by classical means though the Nyquist criterion is a good indicator to identify instable scenarios in a first preliminary stage.

IV. CONCLUSION

The presented can be summarized by the following: The stability of the inverters is power-dependent as the operating power affects the linear time periodic and the linear time invariant characteristics of the inverter. The Nyquist criterion can indicate an instable inverter operation, e.g. a harmonic instability by its classical definition. Resonances in the network characteristics of LV networks can have a significant impact on the inverter stability, e.g. the impedance magnitude amplification. However, the Nyquist criterion is not sufficient to conclude on the stable inverter operation.

Future work will have to expand the database of measured commercially available inverters. For simulations, grey-box time domain models need to be studied further and a measurement-based framework to assess the overall stable operation has to be developed and included in regulations and standards.

Studies of further devices, e.g. rectifiers, need to analyze the device-specific linearity and the feasibility of the coupled Norton model and other small signal models for their representation.

REFERENCES

[1] REN21, *Renewables 2022 Global status report*. Paris, 2022.

[2] X. Wang and F. Blaabjerg, "Harmonic Stability in Power Electronic Based Power Systems: Concept, Modeling, and Analysis," *IEEE Transactions on Smart Grid*. Institute of Electrical and Electronics Engineers (IEEE), p. 1, 2018.

[3] E. Kaufhold, J. Meyer, and P. Schegner, "Modular White-Box Model of single-phase Photovoltaic Systems for Harmonic Studies," in *2019 IEEE Milan PowerTech*, Jun. 2019, pp. 1–6.

[4] E. Kaufhold, J. Meyer, and P. Schegner, "Measurement-based identification of DC-link capacitance of single-phase power electronic devices for grey-box modelling," *IEEE Transactions on Power Electronics*. pp. 1–1, 2021.

[5] E. Kaufhold, J. Meyer, and P. Schegner, "Black-box identification of grid-side filter circuit for improved modelling of single-phase power electronic devices for harmonic studies," *Electric Power Systems Research*, vol. 199. p. 107421, Oct. 2021.

[6] B. H. Lin, J. T. Tsai, and K. L. Lian, "A Non-Invasive Method for Estimating Circuit and Control Parameters of Voltage Source Converters," *IEEE Transactions on Circuits and Systems I: Regular Papers*, vol. 66, no. 12. IEEE, pp. 4911–4921, Dec. 2019.

[7] N. Patcharaprakiti *et al.*, "Modeling of single phase inverter of

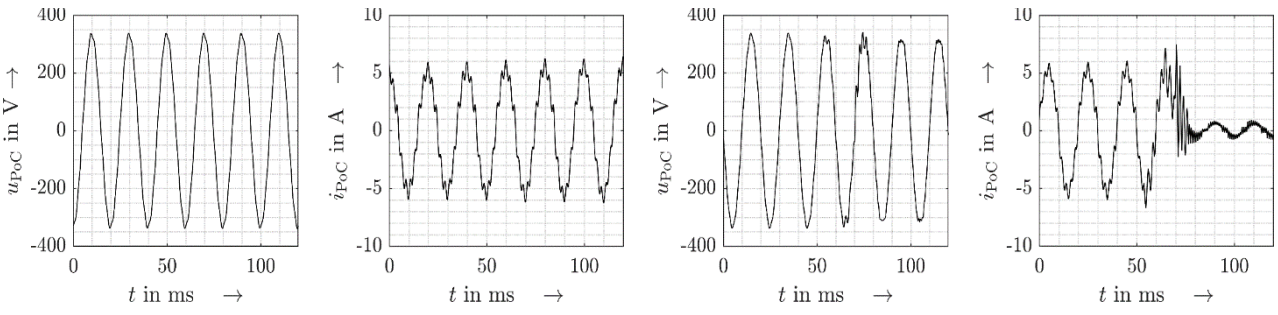

Fig. 8 Voltage (a, c) and current (b, d) measurements at PoC for a test inductance of 3943 µH for a sinusoidal background voltage (a, b - stable) and a flat-top background voltage waveform (c, d – instable).

photovoltaic system using Hammerstein–Wiener nonlinear system identification," *Current Applied Physics*, vol. 10, no. 3. Elsevier B.V., pp. S532–S536, May 2010.

[8] A. S. Abdelsamad, J. M. A. Myrzik, E. Kaufhold, J. Meyer, and P. Schegner, "Voltage-Source Converter Harmonic Characteristic Modeling Using Hammerstein-Wiener ApproachModélisation des caractéristiques harmoniques d'un convertisseur tension-source à l'aide de l'approche Hammerstein-Wiener," *IEEE Canadian Journal of Electrical and Computer Engineering*. pp. 1–9, 2021.

[9] L. M. Wiesermann, "Developing a transient photovoltaic inverter model in opendss using the Hammerstein-Wiener mathematical Structure," University of Pittsburgh, 2017.

[10] E. Kaufhold, S. Grandl, J. Meyer, and P. Schegner, "Feasibility of Black-Box Time Domain Modeling of Single-Phase Photovoltaic Inverters Using Artificial Neural Networks," *Energies*, vol. 14, no. 8. p. 2118, Apr. 2021.

[11] S. Cobben, W. Kling, and J. Myrzik, "The Making and Purpose of Harmonic Fingerprints," *19th International Conference on Electricity Distribution*, no. 0764. pp. 21–24, 2007.

[12] N. M. Wereley and S. R. Hall, "Frequency response of linear time periodic systems," in *29th IEEE Conference on Decision and Control*, 1990, pp. 3650–3655 vol.6.

[13] J. Sun, "Impedance-based stability criterion for grid-connected inverters," *IEEE Transactions on Power Electronics*, vol. 26, no. 11. Institute of Electrical and Electronics Engineers (IEEE), pp. 3075–3078, Nov. 2011.

[14] E. Kaufhold, C. A. Duque, J. Meyer, and P. Schegner, "Measurement-Based Black-Box Harmonic Stability Assessment of Single-Phase Power Electronic Devices Based on Air Coils," *IEEE Transactions on Instrumentation and Measurement*, vol. 71. pp. 1–9, 2022.

[15] R. Stiegler, J. Meyer, S. Schori, M. Höckel, J. Drápela, and T. Hanzlík, "Survey of network impedance in the frequency range 2-9 kHZ in public low voltage networks in AT / CH / CZ / GE," in *25th International Conference on Electricity Distribution*, 2019, no. June, pp. 3–6.

[16] E. Kaufhold, J. Meyer, S. Muller, and P. Schegner, "Probabilistic Stability Analysis for Commercial Low Power Inverters Based on Measured Grid Impedances," in *2019 9th International Conference on Power and Energy Systems (ICPES)*, Dec. 2019, pp. 1–6.

Computation of inrush-current in a phase-shifting transformer connected in series with network coupling transformer

Jiachen Bai
Department of Electrical Energy Systems
University Duisburg-Essen
Duisburg, Germayn
jianchen.bai@uni-die.de

Hendrik Vennegeerts
Department of Electrical Energy Systems
University Duisburg-Essen
Duisburg, Germayn
hendrik.vennegeerts@uni-due.de

Fekadu Shewarega
lDepartment of Electrical Energy Systems
University Duisburg-Essen
Duisburg, Germayn
fekadu.shewarega@uni-due.de

***Abstract*—The investigation of inrush-currents of transformers is a classical task in the design of power systems. For their determination in simulations, usually models based on the duality transformation from a magnetic circuit into an equivalent electric circuit as well as for modelling the magnetic feature of core material, the Jiles-Atherton model is applied. However, the series combination of in-phase-transformer and phase-shifting-transformer (PST) at the interface between transmission and distribution level is a quite new application, emerging from the need of power flow control for the distribution system operator and for the property lines at the low-voltage-side of the in-phase transformer. To confirm the model structure derived in this paper, simulation results based on the new derived transformer model are compared to on-site measurements of inrush-current from an already-operated transformer combination (with unsymmetrical PST) operated by Netz NÖ GmbH. Furthermore, for a pre-evaluation of a new-planning transformer combination (PST is of symmetrical type), comprehensive simulations based on the derived model are carried out. Since not all parameters can be derived from the data sheets provided by transformer manufacturers, sensitivity analysis of some estimated or approximated parameters is also conducted in this paper**

Keywords—inrush current, phase-shifting transformer, transformer EMT model

I. INTRODUCTION

Due to high loading and volatile power flows in both transmission and distribution networks, at their interface power flow control becomes more important. For this task, especially at the interface between the extra-high-voltage (EHV) transmission and high-voltage (HV) distribution networks, the in-phase regulation may be combined with phase-shifting transformer (PST) at the same location. Due to design and construction issues, as well as the often-applied property line at the secondary terminal of the EHV/HV transformer, the combination may result in a series combination.

Inrush-current at the switching-on process of transformer is a well-known phenomenon, which has been considered in design and parametrization work of transformer protection, as well as in the selection of the connection point with neighbouring substations. However, for the configuration of the aforementioned series-combined transformers, both on-site measurements and operational experience are rarely available. Even during factory test, only inrush-current of a single transformer is measured.

Triggered by the aforementioned new-planning configuration of transformers at an EHV/HV-substation, the distribution network operator Netz Niederösterreich (Netz NÖ) who plans to operate a PST at that interface, and the transmission system operator Austrian Power Grid (APG), both agree on a simulative ex-ante investigation to evaluate the possible inrush-current phenomenon, which is carried out by the University of Duisburg-Essen.

II. MODELLING WORK OF TRANSFORMER

In this chapter, the modelling work of in-phase transformer and PST transformer is discussed. First, a general structure of transformer is introduced. Then, the in-phase- and PST-transformer will be specifically introduced.

In Fig. 1, a general physical structure of a 5-limbs-4-windings transformer is given. This structure is applied for the in-phase transformers in this project. The capacitances between different windings, and between windings and ground are partly sketched in Fig. 1. The 4 windings corresponding to different voltage levels are: 1) for EHV, the main winding and the one with adjustable tap-position ports, which are used for star connection; 2) the winding on HV level to be connected with PST, which is also used for star connection; 3) the balancing winding on MV level, which is in delta connection.

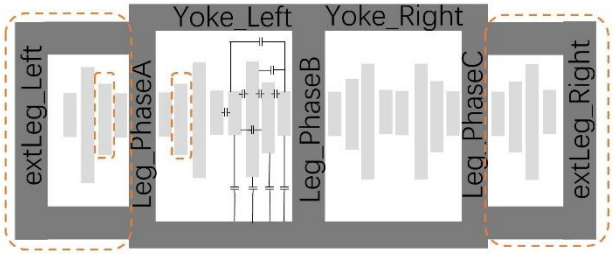

Fig. 1 Physical structure of a general 5-limbs-4-windings transformer

To understand the structure of PST being applied in this project, the parts in the orange dashed lines in the figure can be simply removed to construct a 3-limbs-3-windings transformer, since the symmetrical PST does not have any external legs (limbs) and only 3 windings according to its topology: 1) source-side winding with adjustable tap-position ports in star connection; 2) load-side winding with adjustable

tap-position ports in star connection; 3) excitation winding in delta-connection.

After duality transformation, the physical structure in Fig. 1 can be equivalently transformed through its magnetic-circuit into an electric-circuit as shown in Figure 2. The symbols of nonlinear inductor represent the hysteresis feature of the iron core of transformer. Referring to Figure 1, the whole iron core is equivalently divided into 3 limbs, 2 external limbs and 2 yokes for 3 phases. The symbol of linear inductor represents the leakage inductance between two neighboring windings. The block of ideal transformer defines the winding turns ratio and it establishes the inter-face between the inner part of the dual electric circuit and the external electric network [1] [2]. For the unbalanced operations, a linear inductor is used to enable the existence of zero-sequence fluxes [1]. The resistor symbol represents the winding resistance for each phase and winding. Similarly, by removing the figure parts in the dashed orange lines, an equivalent circuit of PST can be achieved.

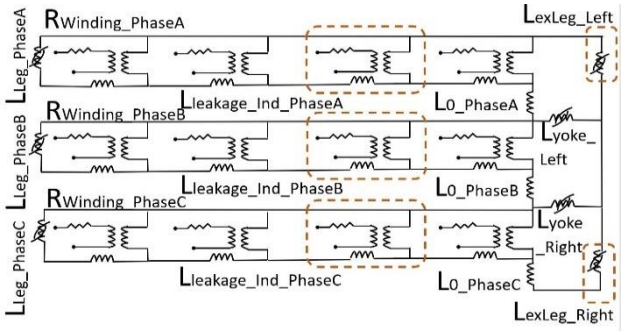

Fig. 2 Equivalent electric circuit of a general 5-limbs-4-windings transformer model after duality transformation from magnetic circuit.

In Fig. 2, a nonlinear-inductor block is used to model the hysteresis feature of iron core. For this, hysteresis-loop (HL) has to be included in this block, where Jiles-Atherton model (JA-model) [3] is applied to formulate HL. The determination of the key parameters of JA-model is done iteratively until the curve matching between the computed HL and the one read from the data sheet of manufacturer is acceptable. In Figure 3, such a comparison between two HLs is given. Except for the upper-left side, the two HLs are matching well, especially in the saturation range, which is decisive for the magnitude of possible highest inrush-currents. With this JA based nonlinear-inductor blocks, the residual fluxes in the transformer core and the saturation phenomenon can be represented appropriately.

As briefly shown in Fig. 1, the existing capacitances in the transformers are also required to be modelled so that the residual fluxes can be predicted by a natural LC response when a transformer is deenergized [1]. The modelling of shunt capacitance for a 5-limbs-4-windings in-phase transformer is given in Fig. 4. The capacitances between windings and between winding and ground, are respectively shown for each phase. Similarly, by removing the parts in the dashed orange lines, the capacitance model for a 3-limbs-3-windings PST can be achieved.

After the brief introduction of the models of the in-phase and PST transformer, their series combination is depicted in Fig. 5 (the whole model on SIMULINK platform)

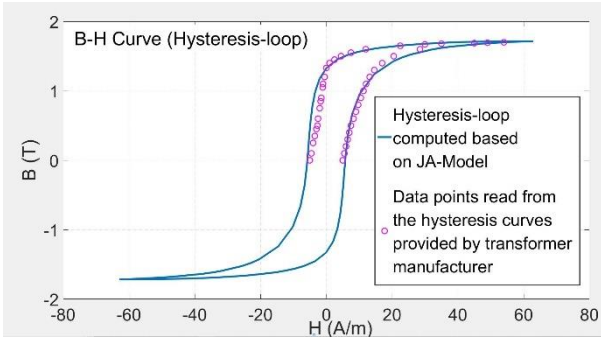

Fig. 3 Comparison between the hysteresis-loop based on the data from manufacturer and the one based on the calculation from Jiles-Atherton Model.

Here only the basic components are shown: a voltage source on EHV level, a switch-signal builder, and packaged blocks of the in-phase transformer and PST models. According to the task, the model is implemented for electromagnetic transient studies (EMT).

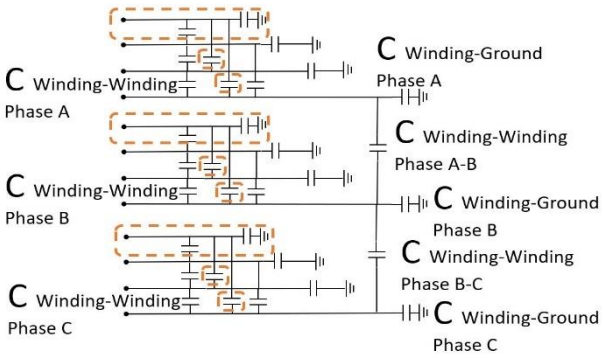

Fig. 4 Shunt capacitance model of a general 5-limbs-4-windings transformer

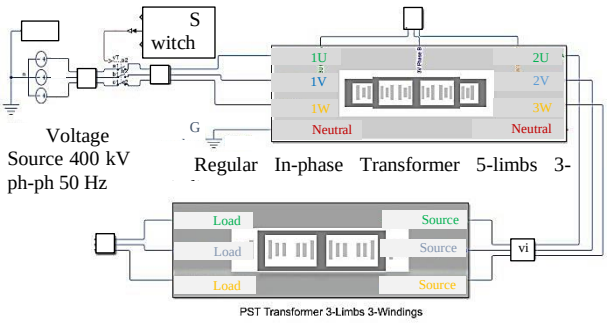

Fig. 5 Series-combined in-phase-transformer and PST transformer modelled in Simulink

III. CONFIRMATION OF MODEL STRUCTURE WITH ON-SITE MEASUREMENT

To confirm the effectiveness of the new-model structure, the simulation results in Fig. 6(b) are compared to the on-site measurement data in the Fig. 6(a). The on-site tests are carried out with the pre-defined switch-on and switch-off

time instants (de-energization and energization instants) corresponding to the specific points on the voltage profile of 3-phases system. For a correct comparison, the instants for the simulations are selected to match the exact same points on voltage profile.

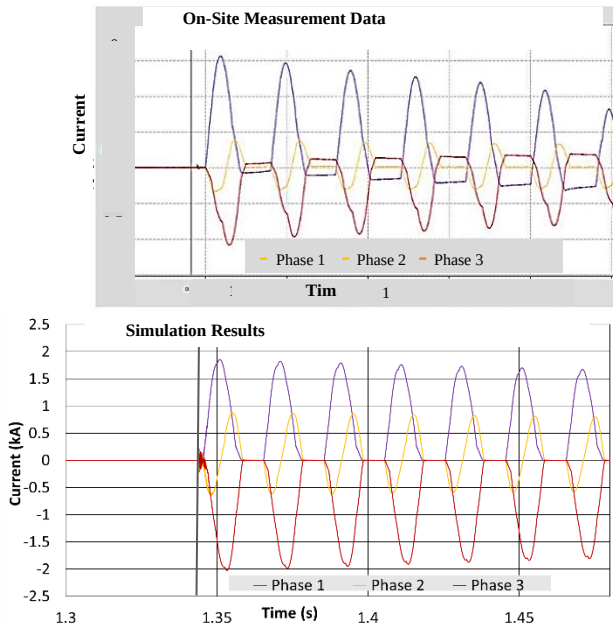

Fig. 6 Three-phase inrush-current profiles

It can be observed from the Fig. 6, the basic curve form of the simulation and of the measurement result is similar. The main difference is the different peak values of inrush-current. The possible reasons of this deviation can be listed as follows: 1) in the simulation model, the switch-actions are ideal actions without considering the condition of real switch-action; 2) in the on-site tests, between voltage source and the in-phase transformer, and between the two transformers, there exist naturally additional capacitances which however cannot be accurately modelled due to limitation of information. These capacitances can affect the residual flux density and as a result, affect the final inrush-current. This assumption has been demonstrated by additional simulations by the authors. As the final conclusion from this comparison, the modelling work of the series-combined transformers is proven to be effective.

IV. SIMULATION BASED PRE-EVALUATION OF INRUCH-CURRENT OF A NEW-PLANNING TRANSFORMER COMBINATION

One of the main tasks of this project is to model the series-combined transformers in the new-planning operation, and with its simulation results to evaluate the levels of inrush-current, e.g. extreme high inrush-currents may give too much stress on neighboring switchgears and lead to additional actions like controlled switching, before the combination is fully operational. To have a comprehensive pre-evaluation, different critical operating conditions have to be investigated by simulation tests.

A. Inrush-current levels of the test cases based on different switch-off instants (Deenergization)

Since different switch-off (transformer de-energization) instants of transformer can affect the final residual flux density, which result in different inrush-current profiles, simulations corresponding to different switch-off instants are carried out. A full period (0º to 360º) of switch-off instants with their corresponding points on voltage curve (phase 1) is given in Fig. 7(a). The 1st peak of inrush-current for each test case are presented in Fig. 7(b). It can be first concluded that the levels of the inrush-current for all the tests remain at an acceptable range for a practical operation. Next, it can be observed that the curve in the Fig. 7(b) is a periodic curve, however without sinusoidal form. One explanation is that residual flux density is an integral of transient voltage after switch-off action, based on the applied model, the transient voltage from different tests does not lead to a sinusoidal envelop curve linking different residual flux density after switch-off action.

B. Inrush-current levels of the test cases based on different switch-on instants (Energization)

Similar to the previous study, since different switch-on instants of transformer can determine the starting point of integral of the voltage curve after switch-on action, which results in different inrush-current profiles, the respective simulations are carried out. Again, a full period (0º to 360º) of switch-on instants with their corresponding points on voltage curve for one phase is given in Fig. 8(a). The corresponding 1st peak of inrush-current for each test case are presented in Fig. 8(b). At first, it can be concluded that the levels of inrush-current for all the tests remain at an acceptable range for practical operation. Next, it can be observed that the curve in the Fig. 8(b) is a periodic and sinusoidal curve. This observation can be mathematically derived by the sinusoidal line in the Fig. 8(a), since the value of each point in this line determines the integral result, i.e. the final inrush-current value.

To be noted from the previous two studies: 1) for the tests with different switch-off instants, the on-instant is fixed to match a zero-crossing point on positive slope on voltage profile. The reason to do it is to have the highest inrush-current contribution from the energization process; 2) for the tests with different switch-on instants, similarly the off instant is fixed to achieve the maximal contribution into inrush-current from the de-energization process. By doing these two things, the worse (highest) case of inrush-current has been included in the studies.

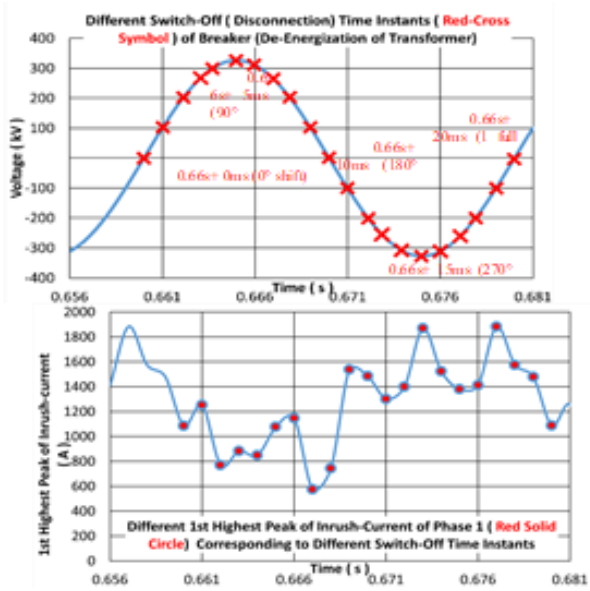

Fig. 7 (a) Different switch-off time instants of transformer; (b) different 1st highest peak of inrush-current corresponding to switch-off instants

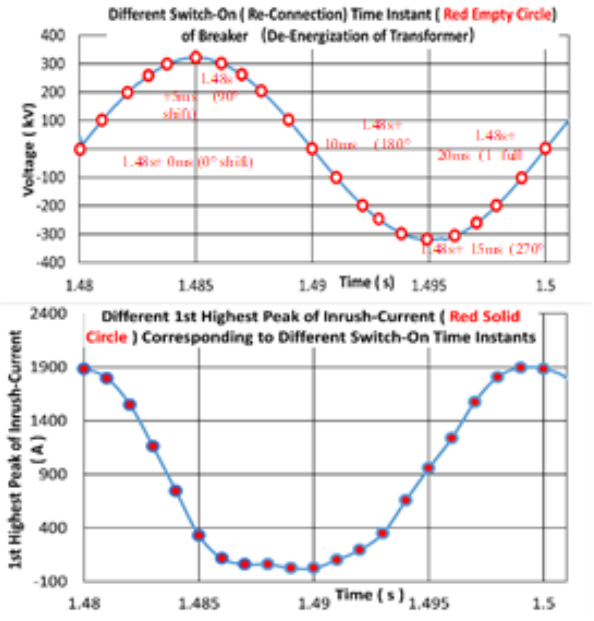

Fig. 8 (a) Different switch-on time instants of transformer; (b) different 1st highest peak of inrush-current corresponding to switch-on instants

C. *Inrush-current levels of the test cases based on different settings of tap-positions*

Similar to the previous studies, since different settings of tap-position for both in-phase transformer and PST can change the voltage conditions of different nodes in the whole model, results in different inrush-current profile, the respective simulations are carried out. There are 4 different settings of tap-positions being listed on Table 1 to cover the most critical conditions. The comparison is given in Figure 9. It can be firstly observed that the tap-position of in-phase transformer (cases 1&2 or 3&4) has a dominant influence on the inrush-current profile, since it determines the voltage level for the switching-on of PST. Secondly, when the tap-position of the in-phase transformer is set at a middle-stage (cases 1&2), a high-level of inrush-current will appear. As a conclusion of this study, the inrush-current values of different cases are still in an acceptable range for practical operation.

Table 1 Study cases of 4 different combination of tap-positions of in-phase transformer and PST

Study Case	Tap-position of the In-phase Transformer	Tap-position of the PST
1	Middle-Stage	Middle-Stage
2	Middle-Stage	Margin-Stage
3	Margin-Stage	Middle-Stage
4	Margin-Stage	Margin-Stage

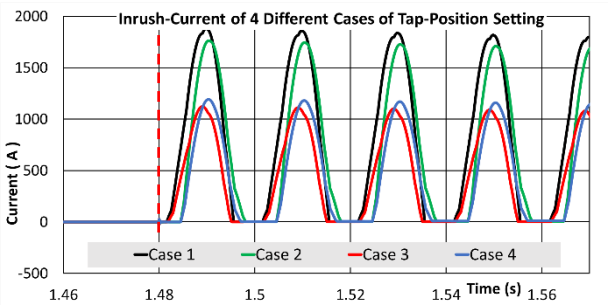

Fig. 9 Inrush-current of 4 cases of different tap-position

D. *Comparison of the inrush-current levels between the series-combined transformers and a single in-phase transformer*

The comparison is given in Fig. 9. It can be directly seen, that after the combination of transformers, the inrush-current is almost double higher than the single application of one in-phase transformer. However, the inrush-current levels are still in an acceptable range.

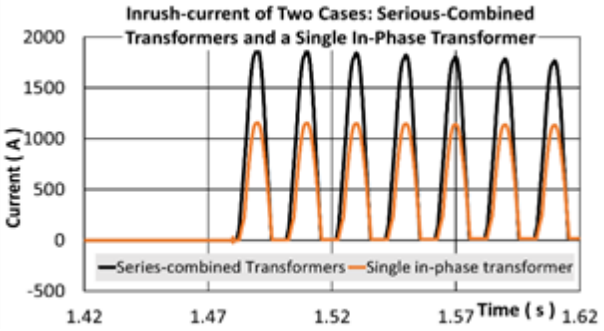

Fig. 10 The comparison of inrush-current profile between two series-combined transformers and a single in-phase transformer.

V. SENSITIVITY ANALYSIS OF ESTIMATED AND APPROXIMATED PARAMETERS

For the parameterization of the model, not all necessary parameters can be found in typical data sheets provided by the manufacturer. Some estimations or approximations are necessary. To check their influence on inrush-current, it is necessary to conduct sensitivity analysis of these estimated parameters. In this paper, only the parameter sensitivity with visible influence on inrush-current are discussed.

A. Capacitive model parameters

The capacitance $C_{ph\text{-}ph}$ between the outmost windings of two different phases is not given by any manufacturer's data sheet. (Also, it is not part of obligatory data according to IEC 60076). An empirical estimation has to be carried out and the sensitivity analysis is given in Fig. 11. With a 30% change to the reference value, the difference of the 1st inrush-current peak is between -16% and +7%. As a conclusion, the estimation of the $C_{ph\text{-}ph}$ has a certain impact on the final inrush-current results.

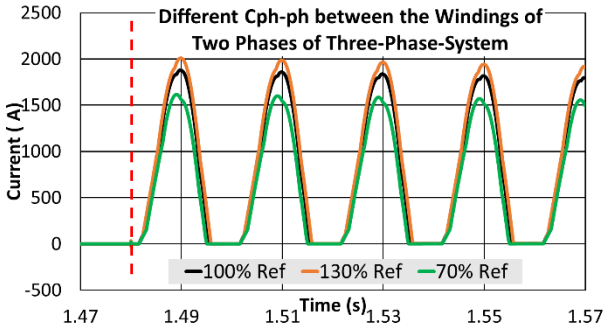

Fig. 11 Inrush-current of 3 cases with different phase-phase capacitance

B. Inductive model parameters

Zero-sequence inductances L_0 of each phase are usually provided by the manufacturer. However, in this case there was some uncertainty about these exact values. Therefore, sensitivity analysis is conducted and given in Figure 12. With a change range from 70% to 200%, the difference of the 1st peak only stays in a small range from -6% to +6%. As a conclusion, the L_0 of the in-phase transformer has only slight impact on the final inrush-current results.

C. Resistive model parameters

The parasitic conductance $G_{Parasitic}$ is used to model the eddy current losses of transformers. In the modelling work, a default value has been adopted. However, it is necessary to understand how much sensitivity the simulation results have to the $G_{Parasitic}$. The conclusion of this analysis is given directly here: the $G_{Parasitic}$ also has a slight impact on the final simulated inrush-currents.

VI. DISCUSSION AND CONCLUSIONS

In this paper, to investigate the inrush-current phenomena of a complex transformer configuration: two transformers in series-combination, the new model is conceived and the relevant modelling work is introduced. By the comparison with the on-site measurement from the application of an already-operated series-combined transformers, the new model's effectiveness is confirmed. Subsequently, with the same model structure, the inrush-current situation of a new-planning application of series-combined transformers is pre-evaluated. Concerning different critical operating conditions, the simulations results show that the dimension of inrush-current is always in an acceptable range which makes the further practical application reliable. Lastly, due to some parameter estimation and approximation involved in the modelling work, the sensitivity analysis of those parameters is carried out and presented.

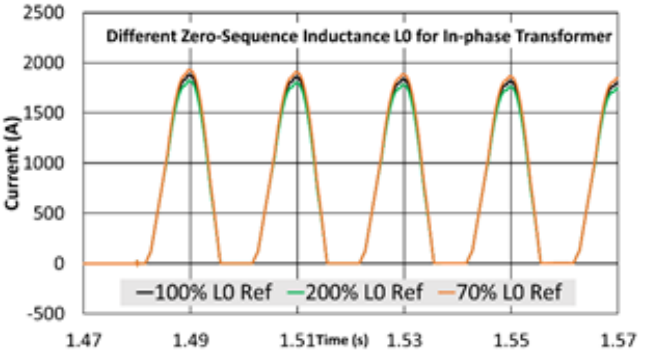

Fig. 12 Inrush-current of 3 cases with different zero-impedance L0 of in-phase transformer.

As a conclusion, the influence of the estimation and approximation on the final simulation results can be negligible. As a result of this study, the new transformer combination has been put into operation. In accordance with the pre-evaluation results, no critical inrush-currents have been experienced.

REFERENCES

[1] N.Chiesa, Bruce A, H.K. Høidalen, 2010, "Transformer Model for Inrush Current Calculations: Simulations, Measurements and Sensitivity Analysis", IEEE Transactions on Power Delivery, vol.25, NO.4, 2599-2608.

[2] M.Shafieipour, W.Ziomek, R.P.Jayasinghe, J.C.G.Alonso, A.M.Gole, 2020, "Application of Duality-Based Equivalent Circuits for Modeling Multilimb Transformers Using Alternative input Parameters", IEEE Access, ISSN: 2169-3536

[3] David C.Jiles, J.B.Thoelke, M.K.Devine, 1992, "Numerical Determination of Hysteresis Parameters for the Modeling of Magnetic Properties Using the Theory of Ferromagnetic Hysteresis", IEEE Transaction on Magnetics, vol.28, No.1

Dynamic Security Enhancement in Power Networks with High Share of Wind and Solar-PV Power Generations

Tahaguas Woldu
Institute of Electric Power Systems
Otto von Guericke University
Magdeburg, Germany
tahaguas.woldu@ovgu.de

Martin Wolter
Institute of Electric Power Systems
Otto von Guericke University
Magdeburg, Germany
martin.wolter@ovgu.de

Abstract— **The issue of environmental concerns and efforts to reduce dependency on fossil fuel are bringing renewable energy resources to the mainstream of electric power generation. Wind power has undergone fast expansions worldwide in recent decades, but it also results in challenging the system operation related to frequency and voltage stabilities. This work is intended to investigate the impacts of wind power and propose mitigation measures to enhance the network dynamic security with higher penetration level of wind power. Doubly-fed induction generator (DFIG) is one of the most common wind turbines that challenges the grid integration during low voltage conditions. In this work, a control strategy is proposed to enhance the low voltage ride-through (LVRT) capability so as not only to remain connected but also to support the system stability during grid fault events. The control strategy comprises a joint application of STATCOM and rotor over-speeding schemes. The STATCOM is mainly employed to improve the stator voltage dip while the rotor over-speeding strategy is engaged to reduce the rotor over-currents during voltage dip that results in reduced output power. To enhance the grid frequency challenges, a frequency control module is proposed to dispatch the wind power generations so as to give support in frequency restoration process. The proposed frequency control module is at plant level and monitors the contribution of various operating units in a wind farm, based on their respective wind speed and the instantaneous frequency deviation. Various types of network topologies and scenarios are employed to study the dynamic responses. The time-domain simulation results indicate that the proposed voltage and frequency control strategies are efficient with higher penetration level of renewable energy sources.**

Index Terms—Dynamic security, Frequency control, LVRT, Rotor over-speeding, STATCOM, Voltage stability, Wind turbine power

I. INTRODUCTION

The increasing demand to reduce fossil fuel products together with environmental concerns have caused an increase in the share of renewable energy. The most common types of wind turbine are variable-speed turbines with partial or full load converter systems [1]. Doubly-fed induction generator (DFIG) is widely used in the wind industry due to its higher conversion efficiency, less mechanical stress, and relatively low cost due to its partial-load converter requirement [1].

High-share of wind power generation stresses transient stability of the power system and affects its operation [2], [3]. As long as the wind power penetration level is low, the behavior of the power system is governed by conventional generators [4]. Compared to synchronous generators, DFIG-based wind generators are more sensitive and respond differently to transient disturbances, such as changes in terminal voltage and frequency [2]-[4]. Therefore, with increasing wind power share, the most challenging issue is to make the wind generators stay connected to the grid system during voltage dips while a grid fault happens [4]. As the power electronics in the DFIG-based wind turbines (DFIG-WTs) are partially loaded, the rotor currents are restricted to the converter ratings for protection purpose so that the fault ride-through capability is of special interest in such cases. This special requirement of DFIG is termed as low voltage ride-through (LVRT) capability [1].

There are quite a few studies in the literature to improve the LVRT capability of DFIG-WTs [5]-[10]. The crowbar protection is among the most common control strategies [5], [6]. During a grid fault, the crowbar circuit is triggered to damp the rotor over-current so that it prevents the rotor current from passing to the rotor side converter. In this regard, the DFIG operates as conventional induction machine, which demands more reactive power from the grid [6], [7]. Although the crowbar is effective to protect the DFIG, the active and reactive controllability using the rotor side converter is momentarily lost. Due to such drawbacks with the crowbar, some researchers have recommended other control schemes [8], [9]. In [8], an advanced control strategy of converters by increasing the generator rotor speed during grid voltage dip is proposed to enhance the LVRT capability by setting the reference torque equal to zero. However, this approach will contribute to vary the grid frequency and it is not also applicable for wind turbines which have reached their maximum limit as the proposed pitch

control method is slow to respond. A DC-link switchable resistive type fault current controller has also been recommended to enhance the LVRT of wind turbine generator (WTG) in [9]. This has also limitations as the DC-voltage itself is triggered during fault time. The studies in [10]-[12] have also recommended the employment of STATCOM to enhance the fault ride-through (FRT) capability of DFIG during grid disturbances. In [10], STATCOM and the crowbar have jointly implemented to improve the FRT capability during 50 % grid voltage sag. STATCOM is also introduced as strategy to enhance the FRT capability during three-phase fault in [11], [12]. However, so far, the STATCOM was mainly used to improve the voltage stability along with the crowbar control for FRT.

Conventional generators have spinning reserve for regulating the frequency oscillations but wind turbines are converting directly the instantaneous wind kinetic energy and it is unlikely to control the variable wind speed. Thus, wind power plants must employ with frequency control strategies so that frequency depression problem can be shared to all operating generators in a system. Energy reserve for wind generators can be applied by either from de-loading operation or through separated storage system [3-eem]. Recently, there are quite many studies on virtual inertial response and de-loading operations based on uniform de-loading rate and governor droop constant [3-eem]-[5-eem]. Such control strategies are limited to vary the droop frequency and de-loading rate with varying wind speeds. The dynamic de-loading operations in [6]-[8-eem] estimate further the de-loading reference power with variable governor droop parameters. However, the de-loading factor is constant and so the governor droop parameter has to depend with the minimum power margin among the wind turbines. Hence, there are no comprehensive studies on dispatching wind power and detail frequency response provisions.

This work assesses the impact of DFIG-based wind power generation and proposes control strategies to enhance the low voltage ride-through capability of the wind generators and grid frequency controllability. The control strategy comprises a joint application of STATCOM and rotor over-speeding schemes to improve the LVRT capability. The STATCOM is mainly employed to improve the stator voltage dip while the rotor over-speeding strategy is engaged to reduce the rotor over-currents during voltage dip that results in reduced output power. The over-speeding scheme is initiated to adjust the active power reference to be proportional to the voltage dip at the stator. Thus, the turbine is made to increase the rotor speed till the maximum allowable limit so that the output power remains reduced until the stator voltage dip is recovered by a fast-acting STATCOM. On the other hand, a new approach is introduced to enhance the grid frequency challenges with higher penetration level of wind power by which wind power plant operators can dispatch their wind power generations so as to give support in frequency restoration process. The proposed frequency control module at plant level monitors the contribution of various operating units in a large wind farm, based on their respective wind speed and frequency deviation.

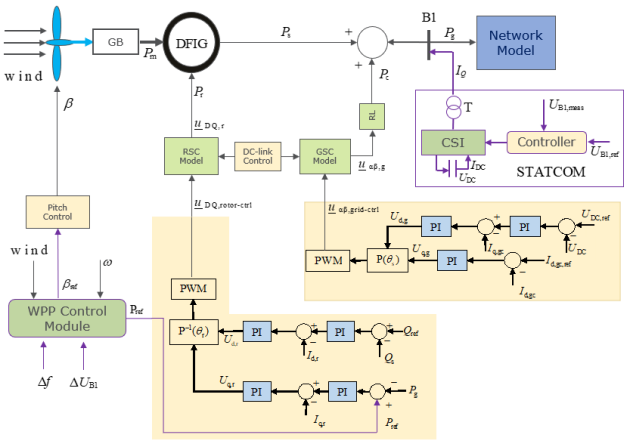

Figure 1. Schematic diagram of DFIG-control strategy

II. SYSTEM MODELING

The dynamic behaviors of the synchronous generator (SG) are represented by 4-th order model as in [10]. Each SG is equipped with IEEE-type DC1A voltage regulator with feedback control to maintain its terminal voltage at a set value [11]. The dynamic parameters of the 4-th order model of SG and the IEEE-type DC1A are specified in [12]. The SG has also included the speed governor and turbine system dynamics to regulate the input power as per the load so that the rotor speed remains at synchronous speed.

The DFIG-based wind turbine model comprises the wind turbine, gearbox system, induction generator, back-to-back converters, and the control system. The active and reactive stator power are controlled by voltage source from the rotor side converter (RSC). The grid side converter (GSC) regulates the converter DC-link voltage. The conventional DFIG control strategy includes the rotor and grid side controllers as depicted in **Fig. 1**, where the active and reactive power of the DFIG is independently controlled using the vector control technique through the rotor side converter as in [15]. With the vector control technique, the stator active and reactive power are controlled by the q-axis and d-axis rotor current components, respectively. The q- and d-axes rotor currents are in turn regulated by the active and reactive power deviations, respectively. While, the grid side converter controller regulates the DC-link voltage [15].

III. LOW VOLTAGE RIDE-THROUGH CONTROL STRATEGY

Low voltage phenomena are generally occurred when a power grid is subjected to transient disturbance such as short-circuit fault or sudden large load change. As a result of this, the grid voltage-dip at the DFIG point of connection (POC) introduces undesirable transients in the stator and rotor circuits. The low voltage condition also limits the active power transmission from wind generators to the grid which results in power imbalance between the turbine maximum power point (MPP) operation and the grid side, leading to significant increase of fluctuations in currents, voltages and rotational speed in the DFIG system.

A voltage dip in the stator of DFIG results in rotor over-current which is essential element for protecting the power

electronic devices. Thus, in order to ride-through the wind generator and protect its partial power converter the DFIG system shall employ either a mechanism to reduce momentarily the rotor circuit over-current or damp the excessive power through temporary circuit like the crowbar application. In this paper, the over-current is reduced by enhancing the voltage dip using a modified STATCOM at the POC and by provisionally over-speeding the rotational speed so that the MPP operation is de-loaded.

The STATCOM is modeled by a cascaded voltage and current PI controllers to regulate the voltage deviation U_g at the POC as in Fig. 1. This simplified model considers only the q-axis component as it refers to reactive power provision as shown in **Fig. 2**. The parameters K_{pu}, K_{iu} and K_{pi}, K_{ii} represent the gains of the PI controllers of the voltage and current controller, respectively. The upper and lower current limits are set according to the nominal power of the STATCOM. The inductance L represents the equivalent inductance of the grid and coupling transformer. The DFIG power electronics are highly sensitive to rotor over-currents so that an immediate protection scheme must be applied as the STATCOM is not fast enough to protect the voltage dip consequences. For this reason, the rotational speed of the rotor is made to over-speed so that the MPP operation of the turbine is regulated to operate at lower mechanical torque, T_m. With such turbine de-loading operation, the torque imbalance between T_m and T_{em}, in (2), is momentarily stored as kinetic energy instead of dissipating. By over-speeding, the turbine accumulates the kinetic energy which can be released when the voltage dip is recovered. The momentary increase of rotor speed is achieved by proper control of rotor side converter through supplementary power to adjust the voltage dip as shown in **Fig. 3.** The control scheme is made to respond to the voltage dip derivative with higher gain, K_d. The supplementary active power, controlled by the voltage dip magnitude, is subtracted from the optimal turbine power so that the reference active power is momentarily reduced.

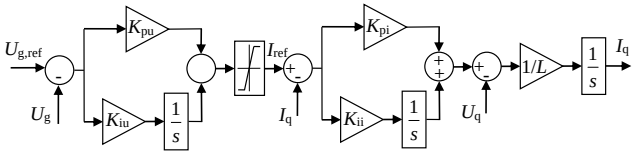

Figure 2. Schematic diagram of the modified STATCOM

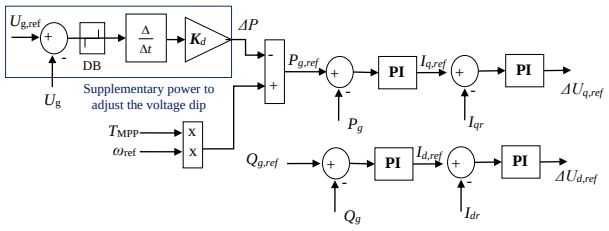

Figure 3. Rotor side converter active and reactive power control with rotor over-speeding strategy in response to voltage dips

When the reference power to the rotor side converter is set at lower value than the optimal power, P_{MPP}, the rotational speed is gradually increasing till the maximum limit. In this regard, the active power control method is modified in such a way that the reference power is dramatically reduced to lower value so that the speed increases and the rotor side converter current decrease. The impact of reducing rotor current resulted in higher fluctuation of DC link voltage. The grid side converter is made to compensate such fluctuation and keep the DC-link transients within the protection limit. With these arrangements, the DFIG-based wind turbine improves its LVRT capability and ultimately contribute support to the grid transient stabilities.

IV. WIND POWER PLANT FREQUENCY CONTROL SCHEME

De-loading operation helps the DFIG-based WTG to take part in primary frequency regulation by which it can have sufficient generation margin during fault events. WTG can operate under stable de-loading operation by limiting the output so that the electrical output reference power, P_{ref} in Fig. 1, is operating at lower value than the optimal power. Such load limitations can be achieved by either rotor over-speeding or by regulating the pitch angle. **Fig. 4** (a) shows a typical WTG that is operating at de-loading rate of d =10%. **Fig. 4** (b) shows that the output power can be reduced by varying its rotor speed and/or pitch angle.

Wind turbines in a WPP might operate at different rotational speeds depending on the stochastic wind speeds. In this work, the wind turbines are generally grouped into four operation regions based on the available wind speeds, as in **Fig. 3** that reduce the computation time. The group of turbines that are receiving low wind speeds (AB), Type-0, do not participate in the de-loading operation. Thus, three groups of WTGs, namely, Type-1, Type-2 and Type-3, are participating in the primary frequency response. The three types of WTGs are operating in wind speed intervals BC, CD and DE based on the wind speed and matching control strategy. Such type of classification allows to take full advantage of distinct regulation range for over-speeding and pitch control that help to use variable de-loading control strategies.

Type-1 WTGs receive wind speed between v_{d1} and v_d, where the first is minimum wind speed that allow turbine to enter de-loading and the later represents the upper wind speed limit in the BC range. In this slot, only rotor over-speeding is applied. The optimal and de-loading reference powers are determined in (1).

$$P_{opt} = 0.5\rho\pi R^5 \frac{C_{p\text{-}max}}{\lambda_{opt}} \omega_{opt}{}^3$$
$$P_{del} = (1-d)P_{opt} = 0.5\rho\pi R^5 \frac{C_{p\text{-}del}}{\lambda_{ref}} \omega_{del}{}^3 \quad (1)$$

Where P_{opt} and P_{del} are the references for power at MPPT and power under de-loading operations, respectively. $C_{p\text{-}max}$ and $C_{p\text{-}del}$ are the wind energy utilization coefficients at MPP and de-loading conditions, respectively. For constant wind speed, $C_{p\text{-}del}$ at optimal pitch angle (β = 0) is determined in (2).

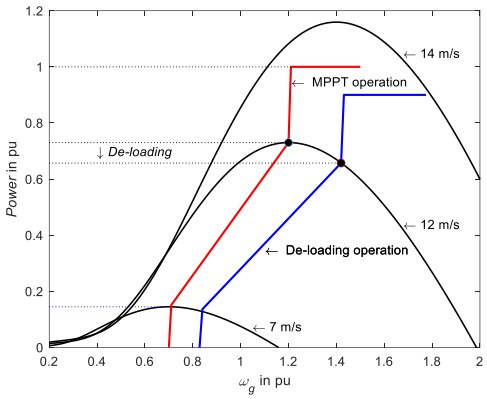

(a) MPPT and de-loading operations

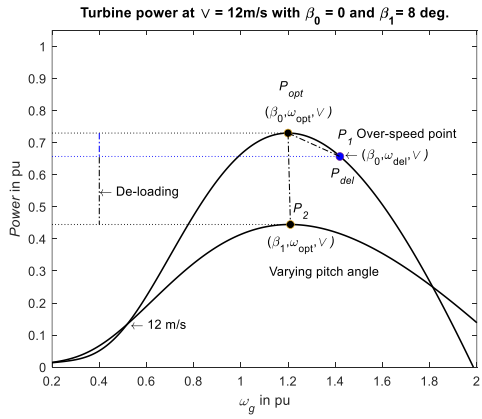

(b) De-loading using over-speed and pitching system

Figure 4. De-loading operation of wind turbines (a) through rotor over-speeding and pitch angle regulation techniques (b)

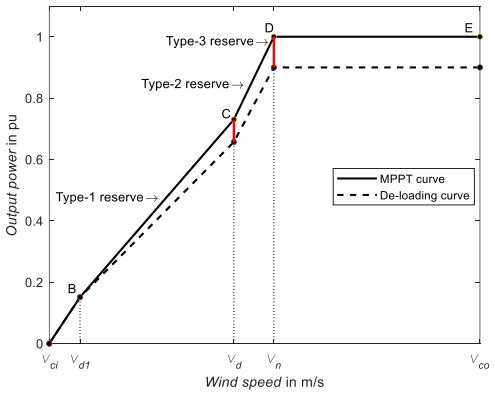

Figure 5. WPP reserve power for frequency control strategies

$$C_{\text{p-del}}(\lambda_{\text{ref}},0) = (1-d)C_{\text{p-max}}(\lambda_{\text{opt}},0) \tag{2}$$

Where λ_{opt} and λ_{ref} are the tip speed ratios during optimal and de-loading operations of wind turbines in Type-1. The rotor over-speeding at the initial de-loading rate, between points B and C, is determined by substituting the reference tip speed ratio and its optimal values in (1) as derived in (3).

$$\begin{aligned} &d_0 P_{\text{opt}} = P_{\text{opt}} - P_{\text{del}} \rightarrow d_0 \omega_{\text{opt}}{}^3 = \omega_{\text{opt}}{}^3 - \omega_{\text{del}}{}^3 \left(\frac{\lambda_{\text{opt}}}{\lambda_{\text{ref}}}\right)^3 \\ &\frac{\lambda_{\text{opt}}{}^3}{\lambda_{\text{ref}}{}^3} = (1-d_0)\frac{\omega_{\text{opt}}{}^3}{\omega_{\text{del}}{}^3} \rightarrow \omega_{\text{del}} = \sqrt[3]{1-d_0}\,\frac{\lambda_{\text{ref}}}{\lambda_{\text{opt}}}\omega_{\text{opt}} \end{aligned} \tag{3}$$

The de-loading reference tip speed ratio, λ_{ref} can be first determined from lookup tables from $C_{\text{p,del}}$ - λ_{ref} - 0 curve. Moreover, upper wind speed limit, v_{d} for Type-1 is obtained from (1) using λ_{ref} and the maximum rotor speed, ω_{max}.

Type-2 wind turbines operate at middle wind speeds, in the range between v_{d} and the nominal speed, v_{n}, where the over-speeding control reaches its upper limit at v_{n}. Thus, over-speeding alone cannot satisfy the required de-loading operation. Therefore, both over-speeding and pitch angle control are jointly applied to accomplish the required maximum reserve power for stable de-loading operation. As the turbine power is generating below its rated value, the reference power calculation for the optimal and de-loading operations are similar to that of Type-1 in (1). However, in this case, the pitch angle is varying so the reference tip speed ratio is first determined from $\lambda_{\text{ref}} = \omega_{\text{ref}} R/v$ at $\omega_{\text{ref}} = \omega_{\text{max}}$, then the reference pitch angle is obtained from lookup table from $C_{\text{p,del}}$ - λ_{ref} - β_{ref}. The $C_{\text{p,del}}$ is determined as in (4).

$$C_{\text{p-del}}(\lambda_{\text{ref}},\beta_{\text{ref}}) = (1-d)C_{\text{p-max}}(\lambda_{\text{opt}},0) \tag{4}$$

Type-3 wind turbines are operating at wind speeds greater than the nominal wind, v_{n} but less than the cut-out wind speed, v_{co}. Over-speeding control has already reached to its upper limit at the end of CD control strategy. Therefore, the only technique to get more reserve at such high wind speeds can be realized by varying more the pitch angle as can be seen in Fig. 4 (b). The reference pitch angle is obtained from lookup table of $C_{\text{p,del}}$ - λ_{ref} - β_{ref} curve where $\lambda_{\text{ref}} = \omega_{\text{ref}} R/v$ and $\omega_{\text{ref}} = \omega_{\text{max}}$. However, the $C_{\text{p,del}}$ for such high wind speed is determined from the ratio factor of the rated power to the ideal power at a wind speed as in (5).

$$\begin{aligned} &C_{\text{p-rated}}(\lambda_{\text{ref}},\beta_{\text{ref}}) = \frac{\text{P}_{\text{rated}}}{P_{\text{opt,3}}} C_{\text{p-max}}(\lambda_{\text{opt}},0) = k_{\text{r}} C_{\text{p-max}} \\ &\rightarrow C_{\text{p-del}}(\lambda_{\text{ref}},\beta_{\text{ref}}) = (1-d)k_{\text{r}} C_{\text{p-max}}(\lambda_{\text{ref}},0) \end{aligned} \tag{5}$$

The de-loading operation reference power for the three types are determined by substituting (2), (4) and (5) into (1). The reserve power P_{res} of the three types is determined as:

$$P_{\text{res}} = P_{\text{opt}} - P_{\text{del}} \tag{6}$$

The plant level frequency control module is modeled to dispatch the imposed power constraint by grid operators over the operating units. The WPP is initially operating at steady state condition with constant de-loading rate, d_0. The decision module algorithm gives dispatching priority to the high wind speed turbines that guarantee the frequency regulation based on the initial reserves. With this algorithm, Type-3 are given first priority and if sum of initial de-loading of this group is not

enough to compensate the limit, Type-2 and then Type-1 in order are dispensed to the frequency change. Then, the algorithm establishes new power margins for the three turbine types that satisfy the pre-defined constraint. Hence, the new power margins will help to set the reference power, P_{ref} and then new de-loading operation point is determined. A new de-loading rating, d_n is determined in (7):

$$d_n = \begin{cases} 1 - \dfrac{P_{ref}}{P_{opt}}; \text{ for Type-1 and Type-2} \\ 1 - \dfrac{P_{ref}}{P_{rated}}; \text{ for Type-3} \end{cases} \quad (7)$$

The WPP will then be ready to respond to any grid frequency change with the help of primary governor. The actual droop parameter, R_w is set to be variable and satisfy the power margins using the linear correlation with droop values as in **Fig. 6**. In this work, the wind turbine droop parameter is set to vary in the range between 2 % – 5 %. The reserve power ranges from the generation margins of Type-3 as $P_{mar,\ max}$ and Type-1 as $P_{mar,min}$. The turbine droop parameter R_w of the three turbine types are calculated from the linear function in (8).

$$R_w = R_{min} + \frac{R_{max} - R_{min}}{P_{mar,max} - P_{mar,min}} (P_{mar,max} - P_{mar,ref}) \quad (8)$$

The *P-f* droop characteristic of primary frequency governor allows multiple generating units to share common load changes [7-eem].

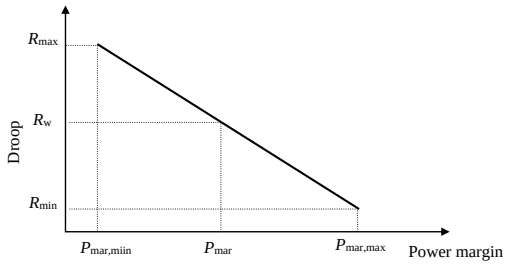

Figure 6. Speed droop values based on the generation margin

In this work, supplementary control loops have been integrated with the rotor side converter control unit that act in response to the grid frequency change, Δf. The primary frequency contribution, ΔP of the wind generator depend on the droop parameter, R_w of the speed governor.

$$\Delta P = \frac{\Delta f}{R_w} \quad (9)$$

The new de-loading rate and droop parameters become variable which allow the turbines with less wind speeds to have higher droop while turbine with high wind speed to have lower droop settings. This allows Type-3 turbines to be mainly responsible for the frequency control. With such arrangements, the stability of de-loading operation is optimized and improved which ultimately results in higher plant capacity rate.

V. SIMULATION RESULTS AND DISCUSSIONS

The proposed LVRT control strategy is implemented with various penetration levels of wind power in the IEEE 39-bus test network. Initially, the network consists of 10 synchronous generators. The synchronous generators at buses 30, 32 and 35 are replaced step by step by aggregated DFIG-based wind generators in three scenarios. The synchronous generators at the three buses have ratings of 1000 MVA, 800 MVA and 800 MVA, respectively. The detail parameters of the DFIG system used in the simulation are presented in the Appendix.

- **Scenario 1:** the test grid consists of all synchronous generators (hydropower plants)
- **Scenario 2:** aggregated DFIG-based wind power at bus 30 and bus 35 which accounts 27 % penetration level of wind power
- **Scenario 3:** aggregated DFIG-based wind generator power at buses 30, 32 and 35 which accounts 40 % penetration level of wind power

The impacts of increasing wind power penetration on the grid frequency are assessed by applying a short-circuit fault at bus 20 with duration of 120 milliseconds for all scenarios.

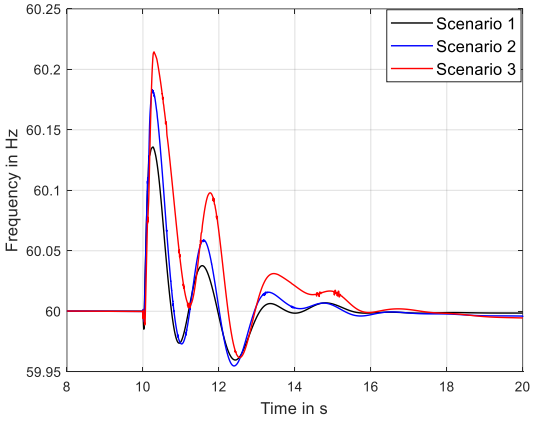

Figure 7. Grid frequency responses for the three scenarios.

The grid frequency response of the three scenarios is depicted in **Fig. 7**. The results show that a higher share of wind generation results in higher fluctuations of grid frequency as indicated by scenario 3.

The proposed LVRT control strategy is implemented on the IEEE 39-bus test system using the third scenario, which has the highest penetration level of wind power. To evaluate the proposed LVRT scheme, three strategies have been adopted and compared in response to the same type of short-circuit fault at bus 20 with clearing time of 120 ms.

- **Strategy 1:** Conventional DFIG-control scheme with maximum power point tracking and without STATCOM as in [18]
- **Strategy 2:** DFIG-control with maximum power point tracking and with STATCOM to compensate voltage dip at stator
- **Strategy 3:** DFIG-control with over-speed control capability and with STATCOM to compensate voltage dip at the stator

Bus 32 is physically close to the fault point which results in a higher stator voltage dip comparing to the others. The voltage dip at this bus is higher for the conventional DFIG-control strategy (strategy 1) as in Fig. 8. Meanwhile, in strategy 2 and strategy 3, the voltage dip is improved compared to strategy 1. In Fig. 9, the rotor current response of each strategy is displayed. The rotor over-speeding strategy is limited within the allowable safety speed. It can be noted that in strategy 1, there is high over-current whereas the rotor over-currents are decreased in strategy 2 and even much better in strategy 3 which makes strategy 3 the best option compared to the other two strategies. However, decreasing the rotor over-current results in high fluctuation of the DC-link voltage as shown in Fig. 10. Thus, it is noted that strategy 3 has higher DC-voltage fluctuation compared to strategy 2 though it remains within the converter protection limits. The results in Fig. 9 reveal that the proposed scheme with a joint application of the modified STATCOM and over-speeding capability (strategy 3) have improved the LVRT capability by reducing the rotor over-currents.

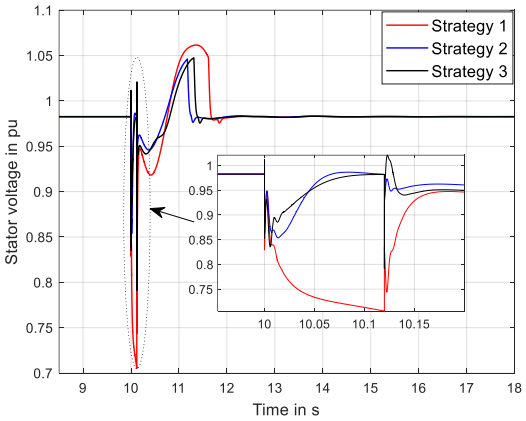

Figure 8. WTG voltage dip response at bus 32 for short-circuit at bus 20.

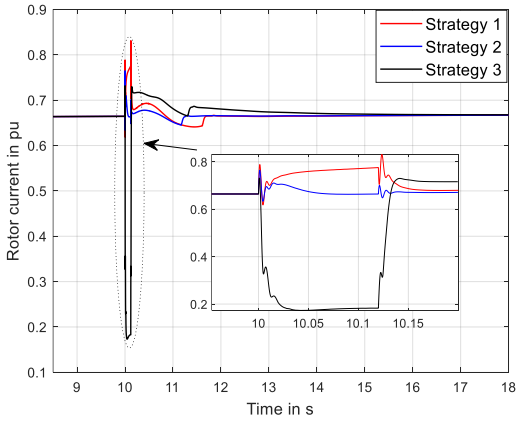

Figure 9. WTG rotor current responses at bus 32 for short-circuit at bus 20.

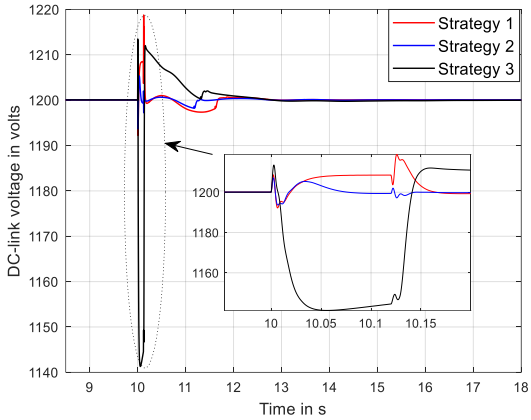

Figure 10. DC-link voltage responses at bus 32 for short-circuit at bus 20.

Moreover, the proposed scheme has enhanced the fluctuations in grid frequency as presented in Fig. 8. The proposed control strategy (specifically strategy 3) helps to improve the grid frequency fluctuations with higher penetration level of wind capacity. In Fig. 8 and Fig. 4, it can be seen that the grid fluctuation has been comparatively improved in strategy 3 compared to the scenario with all conventional generators (scenario 1).

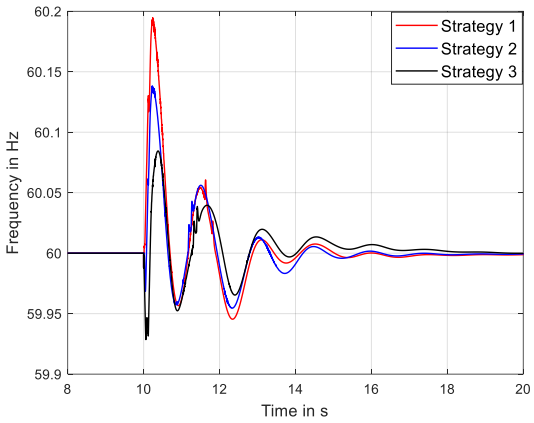

Figure 11. Grid frequency responses for the three strategies.

To verify the effectiveness of the inverter-based converter control strategies, the proposed WPP frequency module has been integrated with a solar PV power plant that have modeled as a virtual synchronous machine (VSM). Figure 12 shows that inverter-based power generation with grid-supporting capabilities of the wind turbines and grid-forming (GFM) control schemes for the PV power plants have significantly improved the grid frequency responses. The results prove that an increase in penetration level of renewable energy sources (such as wind and solar) has increased the grid frequency challenges and they must be employed with grid-forming ancillary facilities to enhance the system dynamics.

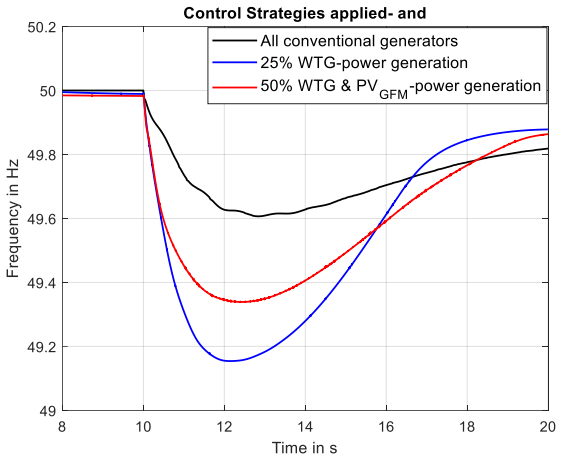

Figure 12. Grid frequency response to a large load change for three different network scenarios

VI. CONCLUSIONS

Power systems with high penetration level of inverter-based power generations, such as wind and solar power, are subjected to higher risks of dynamic instabilities such as LVRT capability, grid frequency and dynamic voltage of critical bus. WTGs must ride-through during grid faults and must support and contribute a role in monitoring the grid operation during fault conditions. On the other hand, solar PV power plants shall support the inertial response of the grid during low availabilities of conventional generators in the system.

In this paper, DFIG-based wind turbines are modeled with enhanced LVRT capability during grid voltage dips. The proposed new control scheme is implemented using a modified STATCOM application jointly with over-speeding capability of rotor side converter control during voltage dip conditions. The proposed control strategy enables the DFIG-based wind generators to improve their ride-through capability during grid voltage dip. The simulation results of the test grid show the proposed control strategies are efficient to suppress the rotor over-current and voltage fluctuations in DC-link which are vital elements for LVRT capabilities. The proposed LVRT enhancement scheme has compared with the conventional DFIG control strategy and the results show employment of both STATCOM and over-speeding control strategy respond better transient behaviors. The PV power plants are employed with grid-forming converter control strategies. Thus, the proposed control strategies of the wind and solar power plants help to suppress the grid frequency transients and support the dynamic voltage stability of the critical bus.

VII. REFERENCES

[1] S. Heier, “Grid integration of wind energy onshore and offshore conversion systems”, John Wiley & Sons, Ltd, United Kingdom, 2014

[2] Z. Chen, Y. Hu and F. Blaabjerg. “Stability Improvement of Induction Generator-Based Wind Turbine System”, IET Renewable Power Generation, Vol. 1, pp. 81-93, 1, March 2007.

[3] I. S. Naser, A. Garba, O. Anay-Lara and K. L. Lo,“Voltage Stability of Transmission Network with Different Penetration Levels of Wind Generation”, 45th International Universities Power Engineering Conference (UPEC), Cardiff, Wales , pp. 1-5, 2010.

[4] P. N. Boonchiam, A. Sode-Yome, K. Aodsup,“Voltage Stability in Power Network when Connected Wind Farm Generators”, PEDS conference, Taipei, pp. 655 - 660, 2-5 Nov. 2009

[5] A. H. Kasem, E. F. EI-Saadany, H. H. EI-Tamaly, "An improved fault ride-through strategy for doubly fed induction generator-based wind turbines", IET Renew. Power Gen., vol. 2, no. 4, pp. 201-214, 2008.

[6] L. Peng, B. Francois and Y. Li, "Improved crowbar control strategy of DFIG based wind turbines for grid fault ride-through", *Proc. IEEE 24th Annu. Applied Power Electronics Conf. Expo.*, pp. 1932-1938, 2009.

[7] V. Akhmatov, Induction Generators for Wind Power, CA, Brentwood, Multi-Science, 2005.

[8] L. Yang, Z. Xu, J. Ostergaard, Z. Y. Dong and K. P. Wong, "Advanced Control Strategy of DFIG Wind Turbines for Power System Fault Ride Through," in *IEEE Transactions on Power Systems*, vol. 27, no. 2, pp. 713-722, May 2012

[9] S. Naderi, Michael N., Amin J., Mehrdad H., Kashem M., Low voltage ride-through enhancement of DFIG-based wind turbine using DC link switchable resistive type fault current limiter, IJEPES,Volume 86, P. 104-119, 2017

[10] P.W. Sauer and M.A. Pai, “Power System Dynamics and Stability”, Prentice Hall, New Jersy, 1998.

[11] IEEE Std 421.5-2005, “IEEE Recommended Practice for Excitation System Models for Power System Stability Studies”, New York, NY 10016-5997, 2006

[12] Woldu, Ziegler, Wolter, Modeling of synchronous generator with fast-response excitation system for studying power network transients, VDE VERLAG GMBH, 2019, S. 37-43

[13] IEEE WG on Prime Mover, “Dynamic Models for Steam and Hydro Turbines in Power System Studies”, IEEE Trans. on PAS, Vol PAS-92, Nov-Dec 1973, pp. 1904-1915.

[14] Olimpo A., Nick J., Janaka E., “Wind Energy Generation-Modelling and Control”, John Wiley & Sons Ltd, United Kingdom, 2009

[15] Vijay V., Raja A., Grid Integration and Dynamic Impact of Wind Energy, Springer-Verlag New York, 2013

APPENDIX: DFIG PARAMETERS EMPLOYED IN THE STUDY:

Nominal power =1.5 MW; U_n (rms) = 0.575 kV; R_s = 0.00706 p.u.; L_{ls} = 0.171 p.u.; L_m = 2.9 p.u.; R_r = 0.171 p.u.; L_{lr} = 0.156 p.u.; H = 0.84 s; number of poles = 6; DC-link voltage = 1200 V; DC-link capacitor = 10 mF; rated wind speed = 12 m/s; Radius =37.5 m; Cut-in speed = 4 m/s; Cut-off speed = 22 m/s; Active power regulator gains [K_p K_i] = [1 100]; Reactive power regulator gains [K_p K_i] = [0.05 5]; DC-link regulator gains [K_p K_i] = [0.002 0.05]; Rotor side current regulator gains [K_p K_i] = [1 100]; Grid side current regulator gains [K_p K_i] = [0.3 8]; Pitch angle regulator gains [K_p K_i] = [500 0]; STATCOM regulator gain K_r = 4 and T_r = 0.2 s; rotor over-speeding derivative gain K_d=50

Simulation Studies of a Model Predictive Control-Based Operation of Island Power Systems

Lucas Reus
Power Engineering Section
Insitute of Electric Power Systems
Leibniz University Hannover
Hannover, Germany
reus@ifes.uni-hannover.de

Marco Alferink
Insititute of Automation
University of Bremen
Bremen, Germany
alferink@iat.uni-bremen.de

Kai Michels
Institute of Automation
University of Bremen
Bremen, Germany

Lutz Hofmann
Power Engineering Section
Insitute of Electric Power Systems
Leibniz University Hannover
Hannover, Germany

***Abstract*—Island power systems still rely to a great extent on the supply by fossil fuel-based generators, although most islands have a sufficient availability of renewable energy sources (RES). Energy management systems (EMS) are proposed as a solution to ensure a stable, secure and economic operation of island power systems with high shares of volatile RES. In this paper an EMS with a model predictive control approach is utilised for the power system of Suðuroy, Faroe Islands. To investigate the stable operation of the power system with the setpoints calculated by the EMS, closed-loop quasi-stationary simulations are performed. The results show that the power system stays stable even for fluctuating wind power and load. Even the loss of a generating unit does not jeopardise the stability of the system. The event-triggered call-up of the EMS after the loss of generation results in the decision to ramp-up another generating unit.**

Keywords—island power systems, energy management system, model predictive control, quasi-stationary simulation

I. INTRODUCTION

Most geographic islands have a sufficient availability of renewable energy sources (RES) for the supply with electric energy [1]. Nevertheless, there is still a vast usage of fossil fuel-based generators in island power systems [2], [3]. Energy management systems (EMS) are proposed in order to deal with the fluctuating generation from RES. With the help of an advanced EMS a stable and economic optimal operation can be ensured while enabling a high share of RES [4]. Due to their sizes, small islands power systems can also be regarded as microgrids (MGs) in isolated operation [5].

Model predictive control (MPC) is used as an approach to deal with the uncertainties and disturbances of load demand and renewable generation. This is allowed by introducing a feedback mechanism. Several works dealing with MPC for MGs only examine single node problems [6], [7]. No optimal power flow (OPF) needs to be calculated in this case, as no spatial distribution of generating units and loads is considered. References [8], [9] incorporate the spatial distribution of generating units and loads. Both sources propose to separately solve a mixed-integer linear programming (MILP) problem for the unit commitment (UC) as well as a non-linear programming (NLP) or quadratic programming problem for the economic dispatch (ED) respectively OPF on different time scales. This approach is also pursued by the authors, proposing a centralised hierarchical EMS based on an MPC approach [10]. The EMS is the key aspect of the proposed MG operation (see Fig. 1).

The UC acts on a long-term planning control level solving the economical scheduling of flexible generating units. The reference values are provided to the next lower level, where at a faster time domain the OPF-based ED is processed, taking all operational and security constraints into account. Setpoints for the local controllers of the distributed energy resources (DER) are calculated and transferred periodically. For this reason, the concept relies on communication infrastructure. The local controllers represent the lowest level of the proposed structure for the isolated operation of MGs.

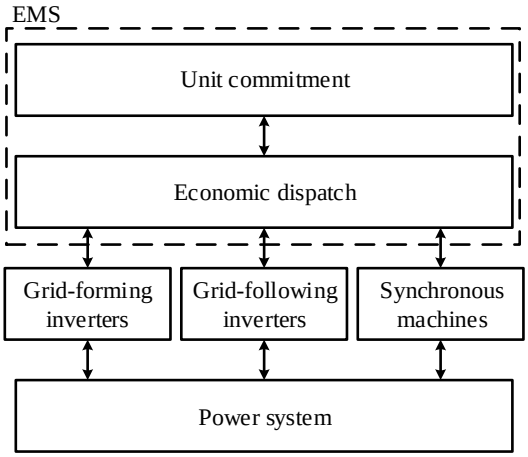

Fig. 1: Hierarchical structure of the control system

In [11] the integration of accurate MG (equipment) models into the investigation of the EMS performance is stated as an open research topic. Few literature was found that included simulated or experimental results of the dynamic interactions of the DER and the EMS. The dynamic responses from the local controllers of the DER in case of forecast uncertainties are shown in simulations in [12] for a rule-based EMS and a grid-connected MG. No results are shown for the response to new setpoints though. Experimental results are shown in [13], but only a single node setup is tested. The authors showed first results of closed-loop simulations in [10]. In this work further closed-loop dynamic simulations of an actual island hybrid power system (Suðuroy, Faroe Islands) are conducted, to verify, if the power system stays stable with the local controls of the DER reacting to the EMS setpoints on the one hand and the dynamic behaviour of fluctuating loads and RES on the other hand. Also the tripping of a DER and an event-triggered call-up EMS are investigated.

The rest of the paper is organised as follows. In section II the power system of Suðuroy and its modelling are described. The EMS and the closed-loop simulation framework are explained in section III. Afterwards, the case study and the simulation results are presented in section IV. In section V the paper is concluded and an outlook on future work is given.

This work was supported by Federal Ministry for Economic Affairs and Climate Action on the basis of a decision by the German Bundestag. Project Inselnetz_optimal funding numbers: 03EI4033A and 03EI4033B.

II. SUÐUROY POWER SYSTEM

The power system of Suðuroy consists of diesel generators (DGs), a hydro power plant (HP), a synchronous condenser (SC), a battery energy storage system (BESS) as well as a wind farm (WF) feeding two ohmic-inductive loads (L1, L2) and one ohmic-capacitive load (L3). The peak load is about 8 MW and the voltage level of the transmission lines is 20 kV [14]. A simplified single line diagram is depicted in Fig. 2.

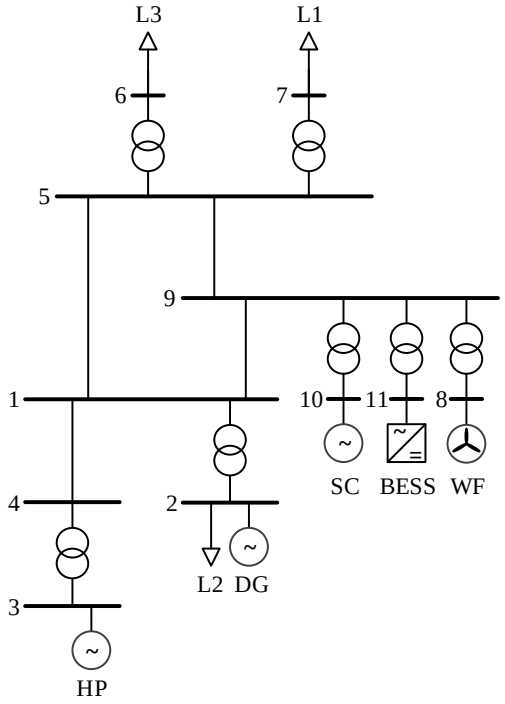

Fig. 2: Single line diagram of the Suðuroy power system

The power system is modelled according to assumptions usually made for quasi-stationary simulations. Therefore, the models of all passive components (lines, transformers and loads) are derived from their stationary equivalent circuits. The lines are modelled by Π-equivalent circuits with lumped parameters, whereas the transformers are modelled by T-equivalent circuits. All lines are cables, resulting in a high amount of reactive power provision by the cables. The loads are described as constant impedances. Balanced operation of the power system is assumed, in agreement with SEV, the grid operator of Suðuroy. For that reason, only positive sequence models are considered. The DERs are described with differential-algebraic equations, as depicted in the following subsections. The described dynamic models are derived from models provided in PowerFactory, including black-box models from the vendors of the WF, SC and BESS.

A. Synchronous Generators

For the quasi-stationary simulation of the synchronous generators (DG, HP) a fifth-order model with one equivalent damper circuit is chosen (a.k.a. model 2.1 from IEEE Std 1110 [15]). It is described by the equations of the flux linkages of the rotor for the excitation winding Ψ_{fd} and the damper windings in the d-axis Ψ_{D} and in the q-axis Ψ_{Q}:

$$\dot{\Psi}_{\mathrm{fd}} = \frac{1}{T_{\mathrm{ff}}}\Psi_{\mathrm{fd}} + \frac{1}{T_{\mathrm{fD}}}\Psi_{\mathrm{D}} + k_{\mathrm{fd}}R_{\mathrm{fd}}I_{\mathrm{Gd}} + V_{\mathrm{fd}} \tag{1}$$

$$\dot{\Psi}_{\mathrm{D}} = \frac{1}{T_{\mathrm{Df}}}\Psi_{\mathrm{fd}} + \frac{1}{T_{\mathrm{DD}}}\Psi_{\mathrm{D}} + k_{\mathrm{D}}R_{\mathrm{D}}I_{\mathrm{Gd}} \tag{2}$$

$$\dot{\Psi}_{\mathrm{Q}} = \frac{1}{T_{\mathrm{Q}}}\Psi_{\mathrm{Q}} + k_{\mathrm{Q}}R_{\mathrm{Q}}I_{\mathrm{Gq}} \tag{3}$$

where T_{ff}, T_{fD}, T_{Df}, T_{DD} and T_{Q} are machine time constants, k_{fd}, k_{D} and k_{Q} are machine parameters, R_{fd}, R_{D} and R_{Q} are the equivalent winding resistances, V_{fd} is the exciter field voltage and I_{Gd} and I_{Gq} are the d- and q-components of the generator's terminal current. The fifth-order model is completed by the equations of motion:

$$\Delta\dot{\omega}_{\mathrm{r}} = k_{\mathrm{m}}t_{\mathrm{e}} + k_{\mathrm{m}}\frac{p}{\omega_0}P_{\mathrm{m}} \tag{4}$$

$$\dot{\delta}_{\mathrm{r}} = \omega_{\mathrm{r}} - \omega_0 = \Delta\omega_{\mathrm{r}} \tag{5}$$

where k_{m} is a machine constant, t_{e} is the electrical torque that acts on the rotor, p is the number of pole pairs, ω_0 is the nominal angular frequency, P_{m} is the mechanical power of the prime mover, δ_{r} is the load angle of the generator and ω_{r} is the angular frequency of the rotor.

This model is extended by an automatic voltage regulator actuating V_{fd}, determined by a PID controller (orientated at type AC8C from IEEE Std 421.5 [16]). The input to the PID controller V_{C} is calculated from the generator's terminal voltage reference $V_{\mathrm{G}}^{\mathrm{ref}}$, the measured terminal voltage $V_{\mathrm{G}}^{\mathrm{meas}}$ and a voltage droop $V_{\mathrm{G}}^{\mathrm{droop}}$:

$$V_{\mathrm{C}} = V_{\mathrm{G}}^{\mathrm{ref}} - V_{\mathrm{G}}^{\mathrm{meas}} - V_{\mathrm{G}}^{\mathrm{droop}} \tag{6}$$

The voltage droop is based on the reactive power reference $Q_{\mathrm{G}}^{\mathrm{ref}}$, the measured terminal reactive power $Q_{\mathrm{G}}^{\mathrm{meas}}$ and the reactive power droop coefficient $K_{\mathrm{G,Q}}$, which is set to zero for all generators in this publication:

$$V_{\mathrm{G,droop}} = K_{\mathrm{G,Q}}\left(Q_{\mathrm{G}}^{\mathrm{ref}} - Q_{\mathrm{G}}^{\mathrm{meas}}\right) \tag{7}$$

Furthermore, a model of the governor is implemented, actuating P_{m}. The generator provides frequency containment reserve P_{FCR}. The governor model consists of a first order lag element and a PI controller. The input to the governor P_{C} is calculated from the generator's terminal active power reference $P_{\mathrm{G}}^{\mathrm{ref}}$, the measured terminal active power $P_{\mathrm{G}}^{\mathrm{meas}}$ and P_{FCR} adjusted by the governor in response to $\Delta\omega_{\mathrm{r}}$:

$$P_{\mathrm{C}} = P_{\mathrm{G}}^{\mathrm{ref}} - P_{\mathrm{G}}^{\mathrm{meas}} - P_{\mathrm{FCR}} \tag{8}$$

A droop is used to determine P_{FCR}:

$$P_{\mathrm{FCR}} = -K_{\mathrm{G,P}}\Delta\omega_{\mathrm{r}} \tag{9}$$

where $K_{\mathrm{G,P}}$ is the generator's active power droop coefficient. The negative sign before $K_{\mathrm{G,P}}$ results from the passive sign convention. The setpoints for $P_{\mathrm{G}}^{\mathrm{ref}}$ and $V_{\mathrm{G}}^{\mathrm{ref}}$ are given by the EMS. The overall structure of the synchronous generator model is depicted in Fig. 3.

B. Synchronous Condenser

An SC is a synchronous machine operated without a prime mover. The model of the SC is therefore equivalent to that of a synchronous generator without the model of the automatic generation control ($P_{\mathrm{m}} = 0$). The setpoint for the SC's terminal voltage $V_{\mathrm{SC}}^{\mathrm{ref}}$ is given by the EMS.

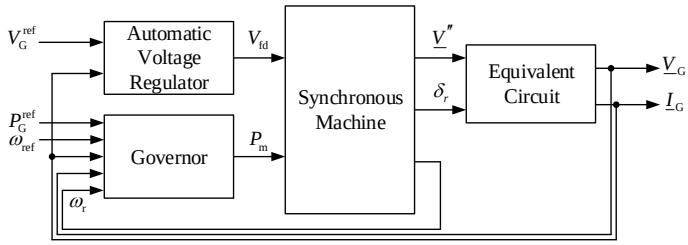

Fig. 3. Structure of the synchronous generator model

C. Battery Energy Storage System

The BESS is modelled only through the grid-side converter (GSC), because the dynamics of the GSC control are the most relevant to depict in quasi-stationary simulations, as performed below. The GSC of the BESS is operating in a grid-forming mode, meaning that the magnitude V_{GSC} and the phase angle θ_{GSC} of the AC voltage are controlled. The phase angle θ_{GSC} is indirectly controlled through the frequency of the voltage. The reference value for the voltage frequency difference $\Delta f_{\mathrm{GSC}}^{\mathrm{ref}}$ from the system frequency f_0 is calculated based on a droop characteristic regarding the active power of the GSC P_{GSC}:

$$\Delta f_{\mathrm{GSC}}^{\mathrm{ref}} = -K_{\mathrm{GSC,P}} \Delta P_{\mathrm{GSC}}^{\mathrm{LPF}} \tag{10}$$

where $K_{\mathrm{GSC,P}}$ is the BESS's active power droop coefficient. The deviation of P_{GSC} compared to a reference value P_{GSC0} is low-pass filtered to gain $\Delta P_{\mathrm{GSC}}^{\mathrm{LPF}}$:

$$\Delta \dot{P}_{\mathrm{GSC}}^{\mathrm{LPF}} = -\frac{1}{T_{\mathrm{P,LPF}}} \Delta P_{\mathrm{GSC}}^{\mathrm{LPF}} + \frac{1}{T_{\mathrm{P,LPF}}} \left(P_{\mathrm{GSC}} - P_{\mathrm{GSC0}} \right) \tag{11}$$

The cut-off frequency of the low-pass filter is described by $1/T_{\mathrm{P,LPF}}$. The relation between $\Delta f_{\mathrm{GSC}}^{\mathrm{ref}}$ and θ_{GSC} is given as:

$$\dot{\theta}_{\mathrm{GSC}} = 2\pi \Delta f_{\mathrm{GSC}}^{\mathrm{ref}} \tag{12}$$

The voltage magnitude reference value $V_{\mathrm{GSC}}^{\mathrm{ref}}$ is calculated similarly through a droop characteristic regarding the reactive power of the GSC Q_{GSC}:

$$V_{\mathrm{GSC}}^{\mathrm{ref}} = V_{\mathrm{GSC0}} - K_{\mathrm{GSC,Q}} \Delta Q_{\mathrm{GSC}}^{\mathrm{LPF}} \tag{13}$$

where $K_{\mathrm{GSC,Q}}$ is the BESS's reactive power droop coefficient. The deviation of Q_{GSC} compared to a reference value Q_{GSC0} is low-pass filtered to gain $\Delta Q_{\mathrm{GSC}}^{\mathrm{LPF}}$:

$$\Delta \dot{Q}_{\mathrm{GSC}}^{\mathrm{LPF}} = -\frac{1}{T_{\mathrm{Q,LPF}}} \Delta Q_{\mathrm{GSC}}^{\mathrm{LPF}} + \frac{1}{T_{\mathrm{Q,LPF}}} \left(Q_{\mathrm{GSC}} - Q_{\mathrm{GSC0}} \right) \tag{14}$$

The cut-off frequency of the low-pass filter is described by $1/T_{\mathrm{Q,LPF}}$.

The cascaded inner voltage and current control loops of the GSC are neglected. The inner control is usually implemented in a rotating reference frame (dq-coordinates), using θ_{GSC} as the transformation angle. Therefore, $V_{\mathrm{GSC}}^{\mathrm{ref}}$ is the reference value for the d-axes part of $\underline{V}_{\mathrm{GSC}}$:

$$V_{\mathrm{GSCd}} = V_{\mathrm{GSC}}^{\mathrm{ref}} \tag{15}$$

$$V_{\mathrm{GSCq}} = 0 \tag{16}$$

Fig. 4 displays the overall structure of the used BESS model.

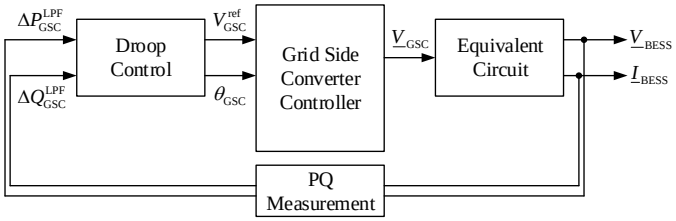

Fig. 4: Structure of the battery energy storage model

D. Wind Farm

The WF consists of seven wind turbines (WTs). All WTs in the WF are assumed to be equal and see the same rotor effective wind speed, thus the WTs of the WF are aggregated in this study. Therefore, no higher level WF controller is modelled. They are modelled by a GSC and an ideal DC link capacitor. An aerodynamic model, the generator and the machine-side converter are neglected. The GSC is operating in a grid-following mode. This means, that the current is controlled in a way (with respect to the WTs' terminal voltage), that the active and reactive power fed into the grid follows given setpoints. In this model the active power setpoints $P_{\mathrm{WF}}^{\mathrm{ref}}$ are obtained from the WTs' power curve, corresponding to a control that is designed to extract the maximum power point possible from the available wind speed until the rated power of the WT is reached. A Phase-Locked-Loop is used to extract the angle of the GSC's terminal voltage. The active power setpoints can be curtailed by the EMS ($\delta_{\mathrm{WF,Curt}}^{\mathrm{sch}} \in \{0,1\}$). In this case, the WT feeds in less power to the grid than potentially possible. The provision of reactive power by the WF is not considered in this paper ($Q_{\mathrm{WT}}^{\mathrm{ref}} = 0$). A detailed description of the implemented GSC control can be found in [17]. The overall structure of the implemented wind turbine model is shown in Fig. 5.

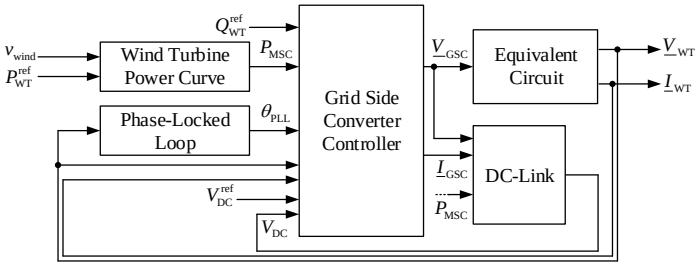

Fig. 5: Structure of the wind turbine model

III. Energy Management System

The EMS within the utilised MPC framework consists of two optimization layers (s. Fig. 1), the UC formulated as an MILP problem and the ED formulated as an NLP problem. Both are solved repeatedly with different frequencies and for different time horizons. The inputs to the UC are the state of charge of the BESS ($SOC_{\mathrm{BESS}}^{\mathrm{meas}}$) and the previous DG's and HP's active power injections ($P_{\mathrm{DG}}^{\mathrm{meas}}$, $P_{\mathrm{HP}}^{\mathrm{meas}}$). The outputs of the UC are the decision, whether the DG or the HP are to be dis-/connected ($\delta_{\mathrm{DG}}^{\mathrm{sch}}$, $\delta_{\mathrm{HP}}^{\mathrm{sch}} \in \{0,1\}$), whether the BESS should be dis-/charged ($SOC_{\mathrm{BESS}}^{\mathrm{sch}}$) or if the WF should be curtailed. The inputs to the ED are the first time step of the optimal solution from the UC, $SOC_{\mathrm{BESS}}^{\mathrm{meas}}$, $P_{\mathrm{DG}}^{\mathrm{meas}}$ and $P_{\mathrm{HP}}^{\mathrm{meas}}$. For both, the UC and ED, forecasts are calculated for the respective time horizon corresponding to the optimization problem. The resulting optimal active and reactive power setpoints and voltage magnitude setpoints from the ED are forwarded to the local controllers of the DERs. A detailed description of the

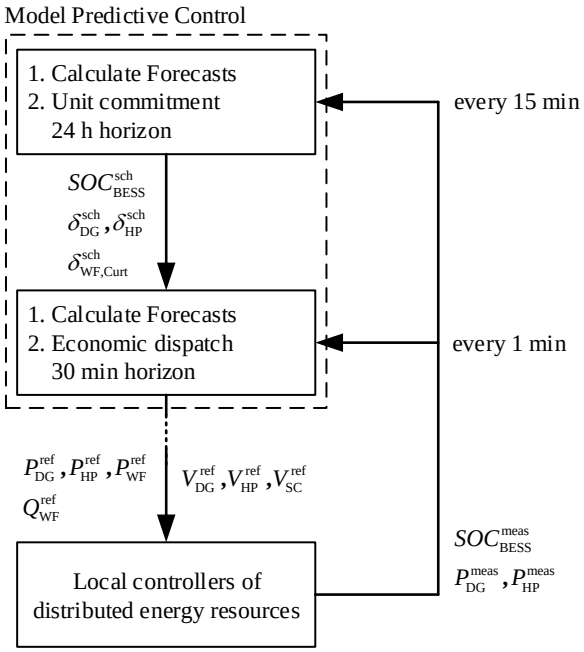

Fig. 6: Flowchart of the utilised EMS

EMS and its layers can be found in [10]. Fig. 6 shows the simplified flowchart of the EMS.

A normal and an event-triggered call-up of the EMS are differentiated. For the normal operation the UC is run every 15 min and the ED every 60 s. In case of a larger disturbance, the EMS is also called outside of the normal operation. In this case both, UC and ED, are calculated. The dotted arrow in Fig. 6 implies that it is possible to evaluate the setpoints with security assessments before they are forwarded to the local controllers. The implementation of security assessments is planned as a future extension of the EMS.

IV. Case Study

For the case study all DER except the DG are active and connected to the grid initially. The state of charge (SOC) of the BESS is chosen to be close to its minimal admissible value. Ideal forecasts are used for the optimization problems based on historic data instead of an actual forecast framework. During the quasi-stationary simulation historic data is used to determine the actually applied load demand and the wind speed. Three different disturbances are given onto the system. For the loads a normally distributed error is added to the respective value of the active and reactive power for every second. Similarly, for the wind a normally distributed error is added to the value of the wind speed for every second. Both of these disturbances can be regarded as small-signal errors, which are not considered when determining the optimal setpoints by the EMS. Additionally at $t = 30$ s the loss of the HP is simulated, which can be regarded as a large disturbance. The tripping starts an event-triggered call-up of the EMS.

The results of the active and reactive powers of the DERs and the loads from the closed-loop quasi-stationary simulation are displayed in Fig. 7 and Fig. 8, respectively. For $t < 30$ s the BESS compensates the fluctuations of the active powers of the WF and the loads. The HP follows its setpoint given by the EMS. A change in the BESS's active power is always combined with a change of the BESS's voltage frequency, due

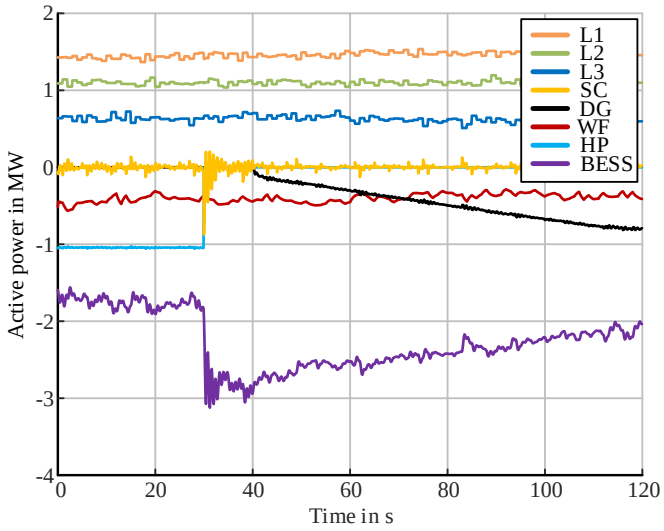

Fig. 7: Simulation results of the active powers of the DERs and loads

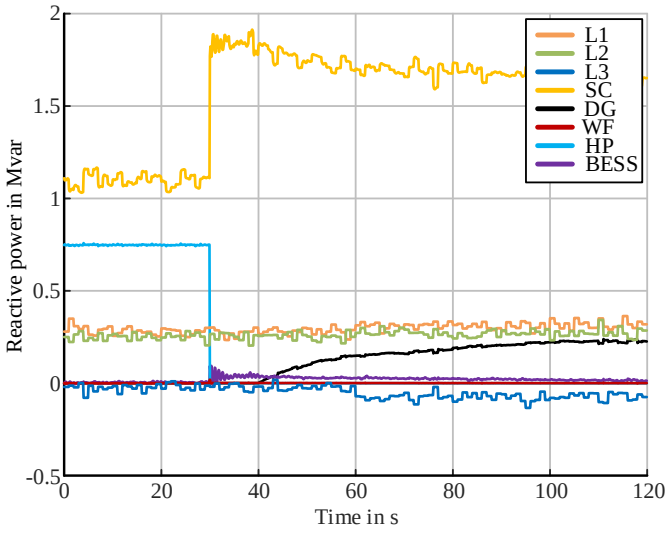

Fig. 8: Simulation results of the reactive powers of the DERs and loads

to the droop characteristic. Therefore, the SC also reacts to the fluctuating active powers although it has no prime mover. With a change in frequency, the SC releases or absorbs active power based on its inertia. Regarding the reactive powers for $t < 30$ s, the fluctuations of the loads are mainly compensated by the SC and to a smaller degree also by the HP. The $Q-V-\text{Droop}$ of the BESS is tuned in a way, that it hardly exchanges reactive power with the grid.

At $t = 30$ s the HP trips. In the first moment, the frequency goes down (not displayed) and therefore the SC releases active power. The BESS reacts shortly after and feeds more active power into the grid. There are damped oscillations between the SC and the BESS following the tripping of the HP. The loss of reactive power is almost entirely compensated by the SC. The HP tripping provokes an event-triggered call-up of the EMS. In the EMS calculations is decided to turn on the DG, because the SOC of the BESS is close to its minimal admissible value. The DG is therefore ramped up from $t = 40$ s on. That the DG is directly available after a short dead time of 10 s is a simplifying assumption. The synchronous connection of the DG to the power system is smooth and doesn't provoke further oscillations. While the

DG is ramping up, the active power from the BESS is reduced accordingly.

The simulation results for the voltage magnitudes of all nodes are shown in Fig. 9. The voltage magnitudes stay within a tolerated band of $\pm 10\,\%$ from the nominal value during the simulation. Due to the provision of reactive power from the cables, the HP was absorbing reactive power before the tripping. Thus, with the loss of the HP the voltages rise. After it's connection, the DG absorbs a high amount of reactive power for a short time, which results in a voltage dip. The voltage magnitude at node 2 is controlled to 1 pu by the DG.

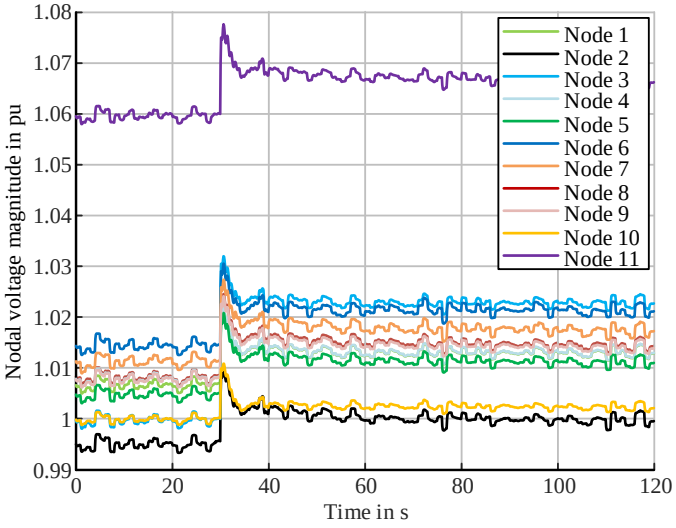

Fig. 9: Simulation results of the node voltage magnitudes

V. Conclusion

This paper presented simulation studies of an advanced energy management system (EMS) for island power systems with fluctuating wind power and loads. As the EMS is implemented in a model predictive control approach closed-loop quasi-stationary simulations are performed. The power system of Suðuroy, Faroe Islands, is used as a test case. Fluctuating loads and wind power, based on historic data, are used for the simulation. Random errors are added to the historic data to create deviations from the optimal setpoints determined by the EMS. A battery energy storage system with a grid-forming controlled inverter and a synchronous condenser hold the system stable during the normal operation with small fluctuations and even after the tripping of a hydro power generator. An event-triggered call of the EMS is provoked through the tripping to adapt the dispatch to changed conditions. The EMS decides to activate and ramp-up a diesel generator, which is successfully done without jeopardising the system stability during the ramp-up time.

Future work includes the integration of forecasts and uncertainties in the closed-loop simulation of the EMS. The EMS is ought to be extended by assessments of the found setpoint regarding the system security, especially the (n-1)-security and the provision of sufficiently high short-circuit currents. The simulation of different types of disturbances and larger island power systems is another step towards verifying the EMS. After profound validation of the EMS in simulation studies a field campaign on Suðuroy is planned.

Acknowledgement

The authors would like to thank Helma Maria Tróndheim and Terji Nielsen from SEV for the provision of data regarding the Suðuroy power system.

References

[1] Y. Kuang *et al.*, "A review of renewable energy utilization in islands," *Renewable and Sustainable Energy Reviews*, vol. 59, pp. 504–513, Jun. 2016, doi: 10.1016/j.rser.2016.01.014.

[2] "Hybrid Systems for Off-Grid Power Supply," CIGRÉ C6.28, Technical Brochure 826, 2021.

[3] F. Rana and A. A. Ali, "Renewable energy targets in small island developing states," International Renewable Energy Agency, Abu Dhabi, 2022.

[4] IRENA, "Transforming small-island power systems: Technical planning studies for the integration of variable renewables," International Renewable Energy Agency, Abu Dhabi, 2018.

[5] N. Hatziargyriou, H. Asano, R. Iravani, and C. Marnay, "Microgrids," *IEEE Power and Energy Magazine*, vol. 5, no. 4, pp. 78–94, Jul. 2007, doi: 10.1109/MPAE.2007.376583.

[6] R. Palma-Behnke *et al.*, "A Microgrid Energy Management System Based on the Rolling Horizon Strategy," *IEEE Transactions on Smart Grid*, vol. 4, no. 2, pp. 996–1006, Jun. 2013, doi: 10.1109/TSG.2012.2231440.

[7] J. Sachs and O. Sawodny, "A Two-Stage Model Predictive Control Strategy for Economic Diesel-PV-Battery Island Microgrid Operation in Rural Areas," *IEEE Transactions on Sustainable Energy*, vol. 7, no. 3, pp. 903–913, Jul. 2016, doi: 10.1109/TSTE.2015.2509031.

[8] D. E. Olivares, C. A. Cañizares, and M. Kazerani, "A Centralized Energy Management System for Isolated Microgrids," *IEEE Transactions on Smart Grid*, vol. 5, no. 4, pp. 1864–1875, Jul. 2014, doi: 10.1109/TSG.2013.2294187.

[9] F. Yang, X. Feng, and Z. Li, "Advanced Microgrid Energy Management System for Future Sustainable and Resilient Power Grid," *IEEE Transactions on Industry Applications*, vol. 55, no. 6, pp. 7251–7260, Nov. 2019, doi: 10.1109/TIA.2019.2912133.

[10] M. Alferink, L. Reus, F. Goudarzi, L. Hofmann, and K. Michels, "Optimization-based operation of island hybrid power systems: a case study in Suðuroy, Faroe Islands," in *7th International Hybrid Power Plants & Systems Workshop*, 2023, pp. 1–8. doi: 10.1049/icp.2023.1427.

[11] J. M. Raya-Armenta, N. Bazmohammadi, J. G. Avina-Cervantes, D. Sáez, J. C. Vasquez, and J. M. Guerrero, "Energy management system optimization in islanded microgrids: An overview and future trends," *Renewable and Sustainable Energy Reviews*, vol. 149, p. 111327, Oct. 2021, doi: 10.1016/j.rser.2021.111327.

[12] K. Mahmud, A. K. Sahoo, J. Ravishankar, and Z. Y. Dong, "Coordinated Multilayer Control for Energy Management of Grid-Connected AC Microgrids," *IEEE Transactions on Industry Applications*, vol. 55, no. 6, pp. 7071–7081, Nov. 2019, doi: 10.1109/TIA.2019.2931490.

[13] W. C. Clarke, M. J. Brear, and C. Manzie, "Control of an isolated microgrid using hierarchical economic model predictive control," *Applied Energy*, vol. 280, p. 115960, Dec. 2020, doi: 10.1016/j.apenergy.2020.115960.

[14] H. M. Tróndheim, L. Hofmann, P. Gartmann, and E. Quitmann, "Frequency and Voltage Analysis of the Hybrid Power System in Suðuroy, Faroe Islands," presented at the Virtual 5th International Hybrid Power Systems Workshop, 2021, p. 6.

[15] "IEEE Guide for Synchronous Generator Modeling Practices and Parameter Verification with Applications in Power System Stability Analyses," *IEEE Std 1110-2019 (Revision of IEEE Std 1110-2002)*, pp. 1–92, Mar. 2020, doi: 10.1109/IEEESTD.2020.9020274.

[16] "IEEE Recommended Practice for Excitation System Models for Power System Stability Studies," *IEEE Std 421.5-2016 (Revision of IEEE Std 421.5-2005)*, pp. 1–207, Aug. 2016, doi: 10.1109/IEEESTD.2016.7553421.

[17] F. Goudarzi and L. Hofmann, "A Combined RMS Simulation Model for DFIG-Based and FSC-Based Wind Turbines and Its Initialization," *Energies*, vol. 14, no. 23, p. 8048, Dec. 2021, doi: 10.3390/en14238048.